

A Survey of Extended H₂ Emission from Massive YSOs.

F. Navarete^{1*}, A. Daminieli^{1*}, C. L. Barbosa² and R. D. Blum³

¹*IAG-USP, Rua do Matão, 1226, 05508-900, São Paulo, SP Brazil*

²*MCTI/Laboratório Nacional de Astrofísica, Rua Estados Unidos 154, CEP 37504-364, Itajubá, MG, Brazil*

³*NOAO, 950 N Cherry Ave., Tucson, AZ 85719 USA*

Accepted 2015 April 22. Received 2015 April 22; in original form 2014 October 28

ABSTRACT

We present the results from a survey, designed to investigate the accretion process of massive young stellar objects (MYSOs) through near infrared narrow band imaging using the H₂ $\nu=1-0$ S(1) transition filter. A sample of 353 Massive Young Stellar Object (MYSO) candidates was selected from the Red MSX Source survey using photometric criteria at longer wavelengths (infrared and submillimeter) and chosen with positions throughout the Galactic Plane. Our survey was carried out at the SOAR Telescope in Chile and CFHT in Hawaii covering both hemispheres. The data reveal that extended H₂ emission is a good tracer of outflow activity, which is a signpost of accretion process on young massive stars. Almost half of the sample exhibit extended H₂ emission and 74 sources (21%) have polar morphology, suggesting collimated outflows. The polar-like structures are more likely to appear on radio-quiet sources, indicating these structures occur during the pre-UCH II phase. We also found an important fraction of sources associated with fluorescent H₂ diffuse emission that could be due to a more evolved phase. The images also indicate only $\sim 23\%$ (80) of the sample is associated with extant (young) stellar clusters. These results support the scenario in which massive stars are formed by accretion disks, since the merging of low mass stars would not produce outflow structures.

Key words: infrared: stars – stars: formation – stars: early-type – stars: massive – stars: pre-main sequence – ISM: jets and outflows.

1 INTRODUCTION

The scenario of formation of low mass stars ($M < 8 M_{\odot}$), through disk accretion controlled by magnetic field is already well understood (Shu et al. 1987). For high masses ($M > 8 M_{\odot}$), however, there are theoretical problems for applying the same scenario. From the observational point of view, there are too few bona fide candidates to test the models. This is due to the fact that massive young stellar objects (MYSOs) are short lived and occur inside large molecular clouds, subject to huge reddening. The relevant phases of massive stars formation are not seen directly at wavelengths shorter than the mid-infrared (MIR) and also to wavelengths longer than radio-mm. Shocked molecular outflows are “smoking guns” of the accretion process and can be traced outside the central heavily obscured zone. The aim of this work is to use the H₂ $\nu=1-0$ S(1) emission to constrain the possible models.

Even after decades of progress both theoretical and observational fronts, formation of massive stars remains an open question. The short timescale for MYSO formation in-

dicates that high rates of mass accretion are required. Two scenarios currently dominate the discussions, *a*) in the first, high mass stars are formed by accretion through a disk (Jijina & Adams 1996; Krumholz et al. 2005); *b*) in the second, high mass stars are formed via coalescence of low mass stars (Bonnell et al. 1998, 2001; Bally & Zinnecker 2005). In the last decade, a number of observations have been presented favoring the first scenario, among them Bik & Thi (2004) and Blum et al. (2004).

Low and intermediate mass stars are formed by the gravitational collapse of the parental giant molecular cloud (GMC), followed by the accretion process (Palla 1996). During the accretion phase, material is ejected as well via collimated bipolar jets. However, when a YSO reaches $8 M_{\odot}$, the radiative flux becomes so intense (using $\phi = L/4\pi d^2$, the ratio between the radiative fluxes of an O5 and a B3 star – masses of ~ 40 and $\sim 8 M_{\odot}$, respectively – is ≈ 250) that it may interrupt the accretion flow. A process that constrains the outcoming radiation field to narrower angles may leave some room for the accretion process to continue in some directions. This seems to be the case for the outflows driven by young stars from a very broad mass range, as previous reported by several authors (Shepherd & Churchwell 1996;

* E-mail: navarete@usp.br (FN); daminieli@iag.usp.br (AD)

Bachiller 1996; Bontemps et al. 1996; Beuther et al. 2002; Wu et al. 2004). Outflows associated with high-mass objects are expected to be more energetic than the outflows observed in lower mass YSOs (Beuther et al. 2005; Zhang et al. 2005; López-Sepulcre et al. 2009), with velocities greater than $\sim 100 \text{ km s}^{-1}$ (Martí et al. 1998). Some authors have found evidences that outflows associated with massive stars are scaled up versions of their low mass counterparts (Vaidya et al. 2011; Codella et al. 2013) while other works have reported that no well-collimated outflows have been found toward MYSOs (Shepherd et al. 2003; Sollins et al. 2004). Massive YSO outflows mapped in high-velocity CO lines have collimation factors $R = \text{length/width} \sim 2.05 \pm 0.96$ as compared to $R \sim 2.81 \pm 2.16$ for low mass stars (Wu et al. 2004), indicating a weak tendency that outflows associated with massive stars are less collimated than those from low mass stars as previously thought (Richer et al. 2000). Besides the degree of collimation, these massive outflows would work removing mass from the plane of the accretion disk, lowering the density on the plane and, therefore, facilitating the accretion flow to reach the stellar core as shown in the recent 3-D simulations presented by Krumholz et al. (2009). Although these authors have not included the outflow activity on their simulations, they argue that the presence of outflows would decrease the star formation efficiency from 70% (considering purely radiation effects) to 50%.

In the second scenario, massive stars are formed by collision and coalescence of low mass stars in dense clusters (Bonnell et al. 1998; Stahler et al. 2000). The low mass stars are formed after the gravitational collapse of the GMC and through an accretion disk, interact with each other, colliding to form stars with greater masses. In this case, the massive stars would be formed in the highest density parts of clusters, and the low mass stars would be the dominant fraction of the entire cluster mass (Bonnell et al. 1998; Bally et al. 2002). Moreover, no massive stars would be expected in small stellar clusters.

While there is no observational evidence for stellar merges in clusters, a growing number of observations supports the accretion disk scenario by answering questions such as the duration of accretion period (Zhang et al. 2005; Beuther et al. 2002), the required accretion rates to overcome the radiation pressure (Kim & Kurtz 2006) and the confirmation of molecular jets ejected from these massive objects (Bally & Zinnecker 2005). The existence of outflows driven by stars from a large mass range is a potentially interesting aspect, since stellar mergers cannot produce stable outflows; therefore, the observation of such flows can be used to discern between the two scenarios of massive star formation.

Bipolar molecular jets associated with MYSO candidates indicate that massive stars are formed by accretion. However, previous samples were contaminated by low mass objects, mostly due to inaccurate photometry. Recently, MYSO candidates were observed in the $\text{H}_2 \nu=1-0 \text{ S}(1)$ transition and collimated jets were identified, suggesting accretion discs around these objects (Varricatt et al. 2010). Although this work presents observational evidence for the accretion scenario, few MYSOs were confirmed in that sample.

To identify bonafide MYSO candidates, accurate photometry and well developed selection criteria are necessary to avoid contamination by normal H II regions, proto-

planetary nebulae (PPNe) and cool stars. The Red MSX Source (RMS) survey (Lumsden et al. 2002; Mottram et al. 2011) contains a large list of objects measured in 2MASS, MSX, Spitzer, and reprocessed IRAS/IGAL images for objects along the Galactic plane, including ultra-compact (UC) H II regions and a large sample of MYSOs. Additional observations were used to separate the MYSOs from UCH IIs, such as water masers (Urquhart et al. 2009b, 2011) and centimetric emission (Urquhart et al. 2007, 2009a). Recently, the bolometric fluxes of those sources were derived by Mottram et al. (2011) using IR and submillimetric data and adopting the kinematic distances derived by CO observations from Urquhart et al. (2007, 2008) and a spectral energy distribution (SED) model. They found there are few MYSOs (~ 20) with $L \geq 10^5 L_\odot$, and many MYSOs (~ 150) with $10^4 L_\odot \leq L \leq 10^5 L_\odot$.

There are a few examples of well documented accretion disks around massive ($10\text{-}30 M_\odot$) forming stars (Davies et al. 2010; Murakawa et al. 2013) using keplerian motion in the CO lines. Disks have been identified in a few cases (Bik & Thi 2004; Blum et al. 2004) through profile fitting of emission features seen in high spectral resolution data, however, the accretion process might have already ceased and the disks are now passively evolving. Although the scenario of an accretion disk may apply for all massive stars, the details are lacking. Instead of doing a detailed study of a small number of potential candidates that might harbor a disk, we are moving toward a large statistical study which will point to accretion signatures (or not) of a well selected sample of MYSOs, selected by the RMS survey.

A smaller survey based on the present motivation was conducted by Varricatt et al. (2010). These authors found that 76% of the targets display H_2 emission, which is indicative of shocks, and in 50% of the sample the H_2 features have some symmetry, suggesting collimated outflows and so accretion disks. Such signatures are more frequent in pre-UCH II than in UCH II phase. The most luminous YSOs in that sample correspond to early B or late O star progenitors. The lack of more massive stars may be due to several causes such as: insufficient number of targets (50); underestimation of luminosities due to errors in the kinematic distances or in the method of magnitude extraction. Problems with the kinematic distances of star forming regions have been pointed out by authors who derive spectrophotometric and trigonometric distances (Hanson et al. 1997; Navarete et al. 2011; Moisés et al. 2011, and references therein). Most non-kinematic distances are half the magnitude of the kinematic ones. As discussed in Moisés et al. (2011), the kinematic distances are larger than their non-kinematic counterparts mostly due to two reasons: a) breaking the ambiguity in the far/near distance is not always a reliable procedure for the kinematic distance method, b) in directions close to the Galactic Center, where radial velocities are small, local perturbations in the gas produces velocity components of the same magnitude as the Galactic rotation. If this result is reliable, than the luminosity of those stars would be ≈ 4 times smaller than predicted by the original data. Unfortunately, MYSOs in pre-UCH II phases have not been reported for massive star clusters, where spectrophotometric distances are accurate.

In this paper, we present the results of our survey, which is organized as follows. In section 2, the observations and

data reduction are described. In section 3 we present overall results from the survey. In section 4 we discuss the results. Finally, our conclusions are summarized in section 5. The images of the sources presenting extended H₂ emission are shown in the Appendix. For those sources that do not display H₂ emission, the images are found in the Vizier Catalogue.

2 OBSERVATIONS AND DATA REDUCTION

The sample of 353 MYSO candidates comprises 135 sources located in the Northern hemisphere ($\delta > 0^\circ$) and 219 from the Southern hemisphere ($\delta < 0^\circ$). Most of the Northern subsample was observed with the Canada-France-Hawaii Telescope (CFHT) and the Southern subsample was observed using the Southern Astrophysical Research Telescope (SOAR). Details of the observing setup used on each telescope are described below.

2.1 Northern Sample

The data were obtained with the CFHT, Mauna Kea, Hawaii, using the Wide-field InfraRed Camera (WIRCam) between 2010 August and 2012 August. The WIRCam detector is a mosaic of four 2048 × 2048 Rockwell Scientific Hawaii-2RG HgCdTe arrays, with a 45'' gap between detectors. The scale is 0.3''/pixel so that a single exposure covers a field of view (FOV) of 21 × 21 arcmin². The median seeing was 0.7 ± 0.2'' and the airmass of each pointing was 1.3 ± 0.2. WIRCam is described by Puget et al. (2004).

The sample was observed through the H₂ ($\lambda = 2.122 \mu\text{m}$, $\Delta\lambda = 0.032 \mu\text{m}$) and *K*-band continuum ($\lambda = 2.218 \mu\text{m}$, $\Delta\lambda = 0.033 \mu\text{m}$) narrow band filters. Each target was observed using a four point dither pattern, defining a 60'' × 60'' square on the sky, with exposure time of $t_{exp} = 150$ seconds per frame, totalling 600 seconds per filter. The dither pattern was employed to cover the 45'' gap between the detectors and also to facilitate the identification and the suppression of bad pixels and cosmic rays. Using the observational setup described above, we reached an average 3σ sensitivity of 19.7 ± 0.5 mag and 19.1 ± 0.2 mag on point sources in the H₂ and continuum filters, respectively. The equivalent 3σ sensitivity per pixel is $3.1 \times 10^{-18} \text{ W m}^{-2} \text{ arcsec}^2$ and $5.9 \times 10^{-18} \text{ W m}^{-2} \text{ arcsec}^2$ for the H₂ and continuum filters, respectively.

2.2 Southern Sample

The Southern sample have been observed with the Southern Astrophysical Research Telescope (SOAR), Cerro Pachón, Chile, using the Ohio State Imager/Spectrometer (OSIRIS) camera between 2011 March and 2011 June and the Spartan camera between 2011 August and 2012 December. The OSIRIS camera has a 1024 × 1024 Rockwell Scientific Hawaii HgCdTe detector with a pixel scale of 0.139''. A single exposure covers a FOV of approximately 1.5 × 1.5 arcmin². OSIRIS is described by Depoy et al. (1993). The narrow-band H₂ ($\lambda_c = 2.116 \mu\text{m}$, $\Delta\lambda = 0.035 \mu\text{m}$) and continuum ($\lambda_c = 2.139 \mu\text{m}$, $\Delta\lambda = 0.050 \mu\text{m}$) filters were used for the OSIRIS observations. The data taken with OSIRIS were observed using a three point dither pattern,

separated by 20 arcseconds in the E-W direction, with exposure times of 180 s per frame, totaling 540 s per filter. Using the observational setup for OSIRIS, we reached an average 3σ sensitivity of 16.8 ± 0.6 mag and 16.5 ± 0.3 mag on point sources in the narrow H₂ and continuum filters, respectively. The equivalent 3σ sensitivity per pixel is $6.8 \times 10^{-17} \text{ W m}^{-2} \text{ arcsec}^2$ and $8.6 \times 10^{-17} \text{ W m}^{-2} \text{ arcsec}^2$ for the H₂ and continuum filters, respectively.

The Spartan Infrared Camera (Loh et al. 2012) has four Hawaii-II arrays deployed in a 2 × 2 mosaic. The pixel scale is 0.067'' such that a single exposure covers a FOV of approximately 5 × 5 arcmin². The narrow-band H₂ ($\lambda_c = 2.117 \mu\text{m}$, $\Delta\lambda = 0.031 \mu\text{m}$) and continuum filters from the Spartan's filter set ($\lambda_c = 2.140 \mu\text{m}$, $\Delta\lambda = 0.030 \mu\text{m}$) were used. The targets observed with Spartan used a four point dither pattern, defining a 60'' × 60'' square on the sky, with exposure time of 150 seconds per frame, totaling 600 seconds per filter. Using the observational setup described above, we reached an average 3σ sensitivity of 16.7 ± 0.5 mag and 17.0 ± 0.4 mag on point sources in the narrow H₂ and continuum filters, respectively. The equivalent 3σ sensitivity per pixel was $2.6 \times 10^{-17} \text{ W m}^{-2} \text{ arcsec}^2$ and $3.6 \times 10^{-17} \text{ W m}^{-2} \text{ arcsec}^2$ for the H₂ and continuum filters, respectively.

The central coordinates of the first 20 objects in the complete sample are listed in Table 1 (the full version of this table containing 353 entries is available online at the CDS).

Each H₂ processed image (see below) was continuum-subtracted by an associated *K*-band continuum image scaled to the same effective bandwidth. The usage of narrow filters avoided contamination by nebular features such as Brackett- γ that would be present in a broad-band filter and so might mask H₂ emission.

2.3 Data Reduction

The images were processed using THELI, an instrument-independent pipeline for automated reduction of astronomical images (Erben et al. 2005; Schirmer 2013). The processing is accomplished through a series of tasks, briefly described as follows. First, the images are dark-subtracted and flat-field corrected. Then a model of the sky background is subtracted from the images. To perform the sky subtraction, THELI masks the point-like sources, creates a first-step model for the sky contribution and subtracts it from the flat-corrected images. Then, the pipeline creates a second-step model to improve the sky subtraction. The astrometric solution for the observed field was determined by cross-matching the sources in each observed field with those from the 2MASS catalog (Skrutskie et al. 2006). For a good astrometric solution, each chip requires a minimum of 80-100 matches. THELI uses SExtractor (Bertin & Arnouts 1996) to extract the position of the point sources on the images and then runs Scamp (Bertin 2006) to derive the astrometric solution and the distortion of the instrument's field-of-view (that is, the pixel scale variation along the FOV). The images were resampled using the astrometric solution determined by THELI and were median combined, creating final H₂ and Continuum images. The astrometric solution was fit as a second order polynomial for each instrument. The residuals to the astrometric fit were ~ 0.3 pixel RMS for all the three instruments.

Post-processing routines were written using IDL to cre-

Table 1. Log of observations.

ID	MSX name	RA (J2000)	Dec (J2000)	d_{kin} (kpc)	$\log(L/L_{\odot})$	Telescope	Semester
001	G016.7981+00.1264	18:20:55.3	-14:15:30.8	14.6	5.14	SOAR	2011A
002	G017.0332+00.7476	18:19:07.3	-13:45:23.6	13.8	4.64	SOAR	2011A
003	G017.6380+00.1566	18:22:26.4	-13:30:12.0	2.3	4.77	SOAR	2011A
004	G018.6608+00.0372	18:24:50.2	-12:39:22.4	10.8	4.29	CFHT	2012A
005	G019.8817-00.5347	18:29:14.7	-11:50:23.6	3.5	3.94	CFHT	2012A
006	G019.9386-00.2079	18:28:09.9	-11:38:22.9	4.5	3.35	CFHT	2012A
007	G020.5143+00.4936	18:26:43.5	-10:48:18.5	13.6	4.10	CFHT	2012A
008	G020.7491-00.0898	18:29:16.4	-10:52:01.2	11.7	4.95	SOAR	2011A
009	G022.3554+00.0655	18:31:44.2	-9:22:17.0	5.2	4.23	CFHT	2012A
010	G023.2628+00.0713	18:33:24.8	-8:33:50.0	4.9	3.88	CFHT	2012A
011	G023.3891+00.1851	18:33:14.3	-8:23:57.4	4.8	4.67	SOAR	2011A
012	G023.4394-00.2394	18:34:51.3	-8:32:55.0	6.0	4.36	CFHT	2012A
013	G023.6566-00.1273	18:34:51.6	-8:18:21.6	5.0	4.17	CFHT	2012A
014	G023.8176+00.3841	18:33:19.5	-7:55:37.8	4.8	3.62	CFHT	2012A
015	G023.8983+00.0648	18:34:37.2	-8:00:12.4	3.0	3.86	CFHT	2012A
016	G024.0946+00.4565	18:33:34.9	-7:38:53.5	5.6	3.50	CFHT	2012A
017	G024.6343-00.3233	18:37:22.7	-7:31:41.5	12.3	4.90	CFHT	2012A
018	G024.7320+00.1530	18:35:50.9	-7:13:27.2	9.1	4.26	CFHT	2012A
019	G025.4118+00.1052	18:37:17.0	-6:38:25.4	5.7	3.97	CFHT	2012A
020	G025.6498+01.0491	18:34:20.9	-5:59:42.5	12.3	5.50	SOAR	2011A

Notes. The first 20 rows of the table is presented. The full version containing 354 entries is available online at the CDS. The columns are – 1: source’s ID; 2: MSX PSC name; 3: right ascension; 4: declination; 5: kinematic distance from Urquhart et al. (2007, 2008); 6: logarithm of the bolometric luminosity (using the bolometric flux from Mottram et al. 2011, and the kinematic distance from column 5); 7: telescope; and 8: semester.

ate the images presented in this paper. The first one crops the final images to smaller ones centered on the source. Next, the H_2 images were continuum-subtracted in order to produce pure H_2 emission maps.

Differences in the filter transmission curves and bandpasses and non-zero interstellar extinction mean a simple subtraction is expected to leave systematic residuals in the point sources and extended emission (where the continuum is strong, at least). In fact the Spartan filters have similar peak transmission and bandpass, so that no large affect is expected based on the filter profile. For WIRCam, the filters have similar peak transmission, but the continuum filter is wider (the ratio of bandpasses is 0.7).

For the strategy employed here of using only one continuum filter to the redward side of the H_2 line is that the interstellar extinction will be slightly higher in the line filter than for the continuum. All other things being equal, and making no extinction correction, there should be a net reduction in the emission signal in a typical source due to extinction. Considering the central wavelength of each filter used in this work (described in Section 2), and assuming the Stead & Hoare (2009) reddening law ($\alpha = 2.14^{+0.05}_{-0.04}$), we have $A_{H_2}/A_{Cont} \approx 1.099 \pm 0.002$ and $1.0234^{+0.0006}_{-0.0004}$ for WIRCam and Spartan, respectively. With no bandpass correction to the WIRCam data, this effect would be enhanced. In practice, residuals were identified on several images. We found a scale factor ranging from 0.63 to 1.75 was needed so that the H_2 and continuum fluxes of the point sources would be approximately equal, minimizing residuals in the final H_2 maps. In the end, we simply minimized the residuals to get a best H_2 map for each source. Since our main goal is to use the morphological information from the maps, this is sufficient for our purposes. The typical scale factor divided into the continuum image to match the line image was 1.14

± 0.10 . This is roughly consistent with expectations from the considerations of bandpass and reddening.

3 RESULTS

The continuum-subtracted H_2 map of each source is presented in the Appendix. An illustrative example of one of these maps is shown in Figure 1. The main frame corresponds to the continuum-subtracted H_2 map. The intensity of each pixel is shown as a multiple of the standard deviation of the continuum subtracted counts and a divergent color scale was used to highlight and increase the contrast of the extended emission: excess of H_2 emission (> 0) is shown in blue while excess of continuum (< 0) is shown in red. The colorbar at the right side of the main image indicates the scale adopted for the image, in units of σ of the continuum subtracted counts. Each H_2 structure is labelled with a dashed circle or a line. The position of the RMS source is indicated by the black circle and its diameter corresponds to the MSX resolution ($\sim 18''$). The coordinates of the MSX position are shown at the bottom of the main frame. We have adopted the green * and yellow Δ symbols in order to distinguish between radio quiet or radio loud RMS sources. Radio loud sources are UCH II regions which harbor nascent O-type stars. MYSOs that are radio quiet must be extremely young if they are massive so that the UCH II region has not yet formed (see Churchwell 2002). When available, the position of the 2MASS and IRAS counterparts of the RMS source are shown as black \times and \diamond symbols, respectively. The secondary image located at one of the corners is shown in red and corresponds to the continuum image of the region delimited by the dashed box. It exhibits the point sources and continuum extended emission

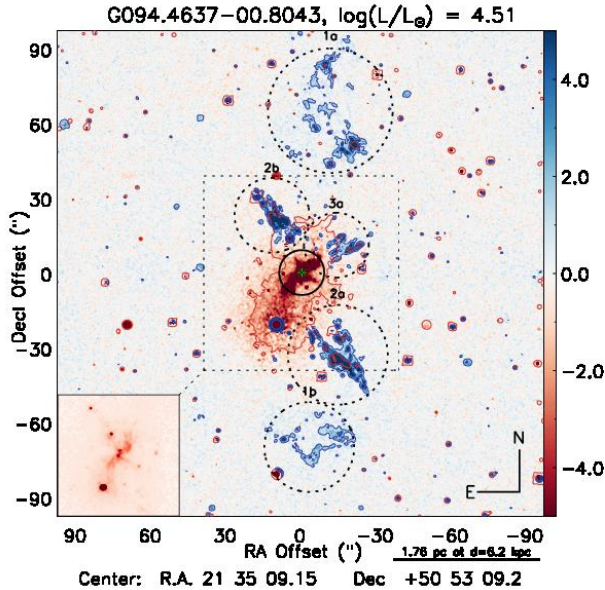


Figure 1. Continuum-subtracted H_2 map of G094.4637-00.8043 scaled by the standard deviation of the continuum-subtracted background counts. Excess H_2 emission (> 0) is shown in blue while excess in the continuum filter (< 0) is shown in red. Radio quiet/loud RMS sources are represented by a green $*$ or a yellow \diamond , respectively (see text). The inset frame displays the details in the continuum filter of the region delimited by the dashed box in the main H_2 map. The inset frame displays the details of the region delimited by the dashed box in the continuum filter. For a complete description, see details in Section 3.

close to the MYSO at the center of the field. Finally, we include a physical scale (in parsecs) based on the kinematic distance of the source (given in kpc). Both values are shown at the top of the horizontal ruler located at the bottom right side of the image.

3.1 Classification of Extended H_2 emission

The continuum-subtracted H_2 map of each source was analyzed and the emission morphology was classified according to the following classes (each type is illustrated in Figure 2):

(i) Polar emission (BPn): Extended H_2 emission likely to be polar and/or jet-like structures (the “n” corresponds to the number of polar structures associated: BP1 is monopolar emission, BP2 is bipolar emission and BP3 corresponds to a region with H_2 emission in three distinct areas/outflow lobes, etc);

(ii) Knot emission (K): K-type morphology corresponds to those sources which display non-aligned knots of H_2 emission;

(iii) Diffuse emission (D): D-type sources are associated with diffuse or filamentary H_2 emission, possibly originating through fluorescent excitation of the H_2 molecules;

(iv) No emission (N): corresponds to non-detections.

BP-type emission is expected to be more often associated with the central sources than K- or D-type ones. In addition, K-type emissions could *i*) correspond to the most brilliant region of a low surface brightness jet structure; *ii*)

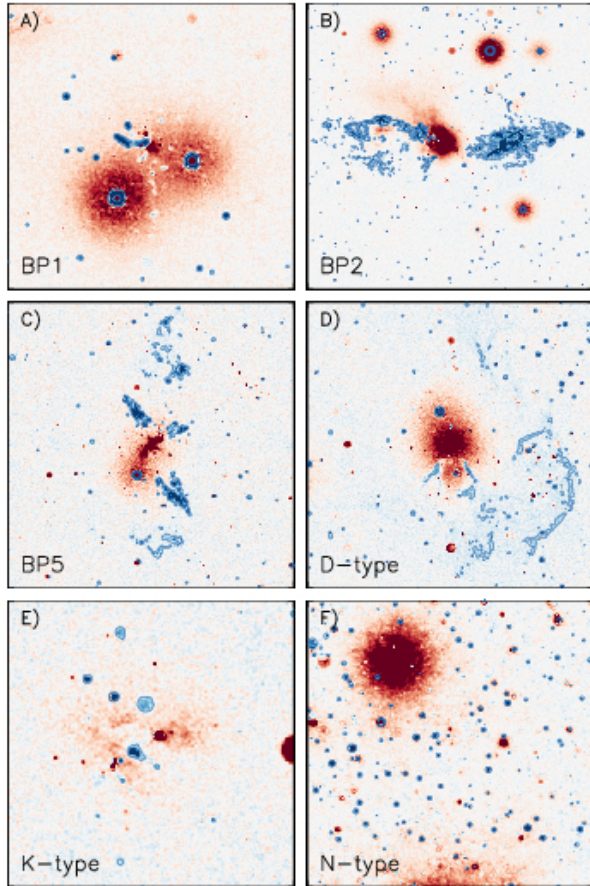


Figure 2. Examples of the morphological classes based on the classification of the H_2 emission. The color scale of each image follows the same definition as Figure 1. The blue contours are placed at $\sigma = 1.0$ and 3.0 . Panels A: BP1-type; B: BP2-type; C: BP5-type; D: D-type; E: K-type; F: N-type.

originate from the interaction of the radiation field with the interstellar medium surrounding the protostar or *iii*) be foreground structures on the line-of-sight of the MSX sources.

Each of the sources has received a primary classification regarding the four classes defined above, and in a few cases, a secondary classification was also provided.

3.2 NIR Classification of the environment

The environment surrounding each RMS source was classified according to the following items:

- (i) presence of extended continuum emission; and
- (ii) association with a stellar cluster.

Extended continuum emission could indicate free-free emission due to ionized gas or scattering by dust. The usage of a narrow band continuum filter could not resolve the origin of the positive detections, which requires additional observations in atomic transitions such as the Br γ ($\lambda \approx 2.16 \mu\text{m}$). The association with stellar cluster candidates was based upon the identification of stellar overdensity around the position of each source. This was performed by analyzing the continuum image of each source “by eye” and distinguishing those which appears to be located within

a group of stars (cases of sources #099, #104 and #112, shown in Appendix A) and those which seems to be isolated sources (such like #132, #189 and #287, also shown in Appendix A).

3.3 Global Analysis of the Sample

Each of the 353 sources were classified as described in the previous subsections and the results are summarized in Table 2. The full version of this table containing 353 entries is available online at the CDS.

The general statistics of the sample are shown in the Panel A from Figure 3. We found extended H₂ emission towards $\approx 50\%$ (178 sources) of the sample; $\approx 54\%$ are associated with extended continuum emission (191); and only $\approx 23\%$ of the sample (80) are apparently members of extant stellar clusters. This result needs some further discussion. Positive association occurs only for those stellar cluster candidates visible at near-infrared wavelengths. In some cases, the members of the cluster would not be visible or may not be formed yet. Therefore, is possible to say that, at least $\approx 23\%$ of the sample have formed within high-density environments. The large number of cases of apparently isolated MYSOs ($\sim 77\%$) suggests that massive stars require a formation mechanism that allows their formation even isolated from other stars.

Panel B from Figure 3 shows the morphological classification of the extended H₂ emission (defined in subsection 3.1) as fractions of the total number of observed sources. The figure shows that $\approx 49\%$ of the sample was classified as N-type objects (175 sources), about $\approx 12\%$ of the sample displays diffuse H₂ emission (43), $\approx 17\%$ of the sample was classified as K-type (61) and $\approx 21\%$ of the sources (74) are associated with polar structures (monopolar, bipolar or multipolar) and, thus, classified as BP-type. Sixty two (62) sources have received a secondary (or multiple secondary) H₂ classification (see Table 2).

The formation of jets does not predict the existence of monopolar structures (BP1) driven by the young stars. BP1 is simply an observational classification. In such cases, it is expected that a conjunction of factors (inclination angle, extinction, opacity of the interstellar medium [ISM] around the protostar) is obscuring the red counterpart of the observed structure. On the other hand, the existence of multipolar structures could be due to the presence of multiple stars and/or a precessing central source with irregular or non-uniform accretion rates. There are 10 BP1, 51 BP2 nine BP4, and one each of BP3, BP5, BP6 and BP8 sources among the total sample of BP-sources.

The magnitude limit of WIRCam observations is ~ 19.5 mag (see section 2.1) for both H₂ and continuum filters, and the magnitude limit for Spartan/OSIRIS is approximately equal to ~ 16.7 mag (see subsection 2.2). The sample can be divided into two subsamples: a northern subsample, containing 185 sources observed with WIRCam; and a Southern one, containing 169 targets observed with Spartan (125) and OSIRIS (43). Panels C and D from Figure 3 show the previous results but as a function of the number of targets from each subsample. Detection of H₂ emission corresponds to $\sim 59.5 \pm 5.7\%$ of the Northern subsample and $\sim 40.5 \pm 4.9\%$ of the Southern one (the uncertainties correspond to a random distribution error). Comparing each H₂ emission type

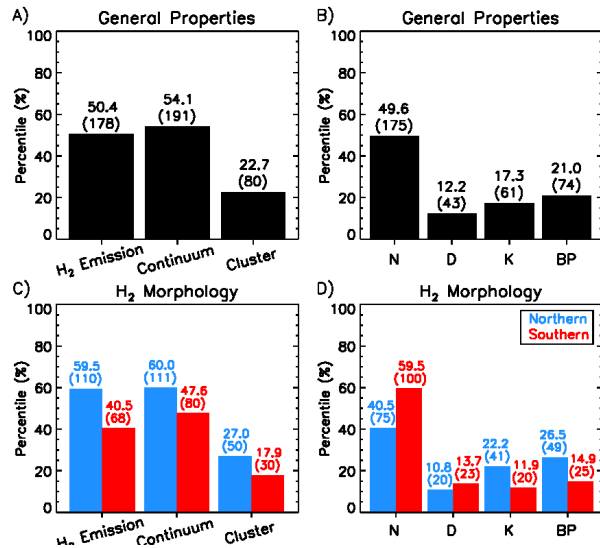


Figure 3. Global properties of the sample. Panel A: detection of extended H₂ and continuum emission and association with stellar clusters; Panel B: assigned morphology of the H₂ emission. Panels C and D: same as Panels A and B but shown for Northern (in blue) and Southern subsamples (in red) individually. The number of sources is shown in parenthesis at the top of each bar. Its corresponding percentile is shown right above it.

shown in Panel D, the Southern subsample has fewer K- and BP-type sources, but shows a similar fraction of D-type ones as compared to the Northern subsample.

These differences in subsamples do not appear significant, but several factors may explain them. The filter sets in WIRCam and Spartan/OSIRIS are fundamentally different. WIRCam uses wide, well separated filters, while the Spartan/OSIRIS filters are narrower but closer together (in fact they overlap to some extent). For WIRCam, the filter transmission curve for the H₂ filter shows there might be some non-zero transmission in the red wing at the wavelength of Br γ . This suggests some strong Br γ sources could produce false H₂ detections. For Spartan/OSIRIS the concern is a strong Br γ line in the wing of the continuum filter might cause a faint H₂ source to be undetected (due to over subtraction). The other possibility is due to the flux limitations of the southern observations. It is possible that we are unable to detect some faint H₂ emission in the south sample due to the flux limit of these images. While the differences in the number and type of H₂ detections may be significant (2.8σ), we do not believe the difference in frequency between the two samples changes our main conclusions about the character of the star formation process.

Figure 4 summarizes the morphological classification defined in subsection 3.2 (N, D, K and BP). Panel A displays a correlation between the sources associated with BP-, K- and D-type extended H₂ emission with those which display extended continuum emission (roughly $\sim 80\%$ compared to $\sim 26\%$ found for N-type sources).

This correlation with extended continuum emission could be due to two processes: *i*) nebular emission or *ii*) dust-scattered radiation. The present observations do not allow us to resolve the nature of the continuum emission. Additional observations of atomic transitions (such as Brackett- γ

Table 2. General classification of the sources.

ID	Ext. Continuum Emission	Stellar Cluster	Primary H ₂ Classification	Secondary H ₂ Classification	Components
001	Y	N	N	-	-
002	N	N	BP2	D	BP2(1a,b), D(2a,b)
003	Y	N	D	-	D(1)
004	N	N	N	-	-
005	N	N	N	-	-
006	Y	N	BP2	K	BP2(1a-f),K(2,3,4)
007	Y	N	K	-	K(1,2)
008	N	N	N	-	-
009	N	N	N	-	-
010	N	N	N	-	-
011	N	N	N	-	-
012	N	N	N	-	-
013	N	N	N	-	-
014	N	N	N	-	-
015	N	N	N	-	-
016	N	N	N	-	-
017	N	N	N	-	-
018	Y	N	K	-	K(1,2)
019	N	N	BP2	-	BP2(1a,b)
020	N	N	N	-	-

Notes. First 20 rows of the table is presented. A full version containing 353 entries is available online at the CDS. The columns are – 1: source’s ID; 2: extended continuum emission (yes or no); 3: association with a stellar cluster (yes or no); 4: primary classification of the H₂ emission; 5: secondary (when given) classification of the H₂ emission; 6: structures classified in main components labeled by numbers (i.e., 1, 2, 3) and, when applicable, related components are given by numbers and letters (i.e., 1a, 1b). For example, a BP2(1a,b) indicates one bipolar structure with two components while a BP1(1a,b,c,d) means four distinct components within a single polar structure.

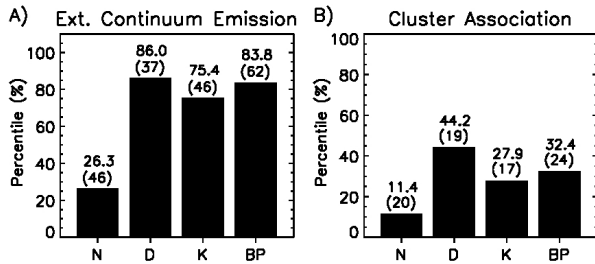


Figure 4. Global properties of the sample as a function of the H₂ morphology. Each source was classified by the presence (or absence) of extended continuum emission (Panel A) and association with stellar clusters (Panel B). The bars correspond to the percentile of the sources classified as N-, D-, K- and BP-type, respectively (see text). The number of sources is shown in parenthesis at the top of each bar. Its corresponding percentile is shown right above it.

in 2.16 μm) could trace the gaseous emission associated with such regions.

Panel B from Figure 4 shows that most stellar clusters with MYSOs exhibit H₂ emission. Comparing stellar clusters and associated extended continuum emission, most of the sources associated with clusters also exhibit extended continuum emission (61 of 80). While clusters appear to be more likely to exhibit continuum emission, there is no preference for isolated MYSOs: 47% of the sources that do not belong to stellar clusters exhibit extended continuum emission (139 of 274).

3.4 Radio quiet/loud phases and H₂ morphology

The RMS sources were observed at 6 cm by Urquhart et al. (2007, 2009a) and were classified by those authors as radio quiet (YSO) or radio loud (H II) sources. Our sample consists of 282 radio quiet sources and 72 radio loud ones. The fraction of the radio loud sources is smaller than the radio quiet one, which may introduce a bias against UCH IIs. Besides of that fact, the comparison between their NIR properties could provide useful information of the intrinsic properties of each phase.

Figure 5 displays the global results of the survey as a function of the radio emission. Panel A shows that the fraction of radio quiet sources (shown as black bars) associated with both extended H₂ and continuum emission is $\sim 10\%$ larger than the values found for radio loud ones (shown in blue). The fraction of radio quiet or radio loud sources associated with stellar clusters is almost the same ($\sim 20\%$). Panel B indicates that most of radio loud sources were classified as N-type sources (44 from 72). Comparing the other three classifications, the fraction of radio loud sources decreases from D-type ($\sim 21\%$) to K- ($\sim 13\%$) and BP-type sources ($\sim 4\%$). On the other hand, the fraction of radio quiet sources increases in the opposite direction: there is a minimum for D-type ($\sim 10\%$), and an increase for K- ($\sim 18\%$) and BP-type ones ($\sim 25\%$). This result suggests that polar H₂ emission is found preferentially towards radio quiet sources (MYSOs) while diffuse H₂ emission is more often associated with radio loud ones, corresponding to more evolved phases (pre-UCH II).

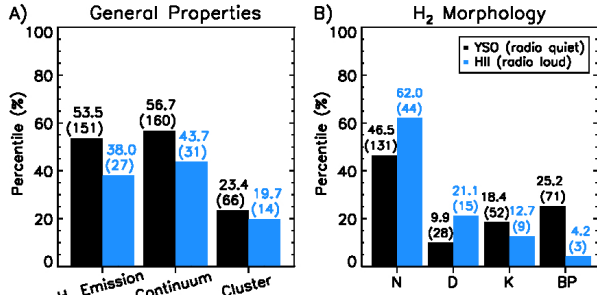


Figure 5. Same data from Figure 3 but separated into radio quiet (YSO, in black) and radio loud (HII, in blue) subsamples. The number of sources is shown in parenthesis at the top of each bar. Its corresponding percentile is shown right above it.

3.5 Luminosity vs. Distance diagrams

Figure 6 presents the distribution of MYSOs as a function of luminosity and distance. The diagrams were constructed using a luminosity and kinematic distance binning of $\Delta \log(L/L_{\odot}) = 0.5$ and $\Delta d = 2.0$ kpc, respectively. Since the RMS sources were selected by their infrared colors, fainter targets at larger distances may not be included in the final sample (our sample is flux limited). This is consistent with the lack of low luminosity sources beyond distances of ~ 10 kpc. The full sample distribution is shown in Panel A. Most of the sources are mid- to high-luminosity objects with $3.0 \lesssim \log(L/L_{\odot}) \lesssim 6.0$, located at $d \lesssim 14$ kpc. There are two overdensity regions at *i*) $\log(L/L_{\odot}) \sim 3.5$ and $d \sim 6.0$ kpc; and *ii*) $\log(L/L_{\odot}) \sim 5.0$ and $d \sim 12.0$ kpc. This is consistent with the low star formation rate in the Solar neighborhood that comprises mainly low-mass stars (the local IMF, $\xi(m) \propto m^{\alpha}$, is well constrained by assuming $\alpha \sim 1.3$ for $m < 0.5 M_{\odot}$ and $\alpha \sim 2.2$ for $m > 0.5 M_{\odot}$, Kroupa 2007). Panel B displays the detections of extended H₂ emission. It peaks at mid- to high-luminosity sources ($3.0 \lesssim \log(L/L_{\odot}) \lesssim 4.5$) located at distances $d \sim 3$ kpc, consistent with the peak *i*) from Panel A. The distribution extends up to the most luminous ($\log(L/L_{\odot}) \sim 6.5$) and far sources ($d > 24$ kpc) of the sample. The positive detections are mostly found toward sources with $d < 10$ kpc (the second peak from Panel A was not identified in Panel B), indicating that the H₂ emission is detected for the most luminous sources of the sample ($\log(L/L_{\odot}) \sim 6.0$), although it is preferably found for less luminous ones located at closer distances. The distribution of sources associated with extended continuum emission is shown in Panel C. It depicts a similar profile as that for the extended H₂ emission (Panel B). Panel D presents the distribution of the sources associated with stellar clusters. The plot peaks at mid- to high-luminosity sources ($3.5 \lesssim \log(L/L_{\odot}) \lesssim 5.0$) located at $d \lesssim 6$ kpc. This is not surprising, since most known clusters lie between the sun and Galactic center (Moisés et al. 2011).

Figure 7 displays the distribution for each H₂ morphological class defined in Section 3.1 in the luminosity vs. distance diagram. Panel A shows that the most of the BP-type sources correspond to sources with $2.5 \lesssim \log(L/L_{\odot}) \lesssim 4.5$ within distances less than $d \sim 10$ kpc. The maximum frequency of polar structures peaks at sources with $3.0 \lesssim \log(L/L_{\odot}) \lesssim 4.0$ located at $d \sim 4$ kpc. This plot indicates that jet-like structures are associated with the low

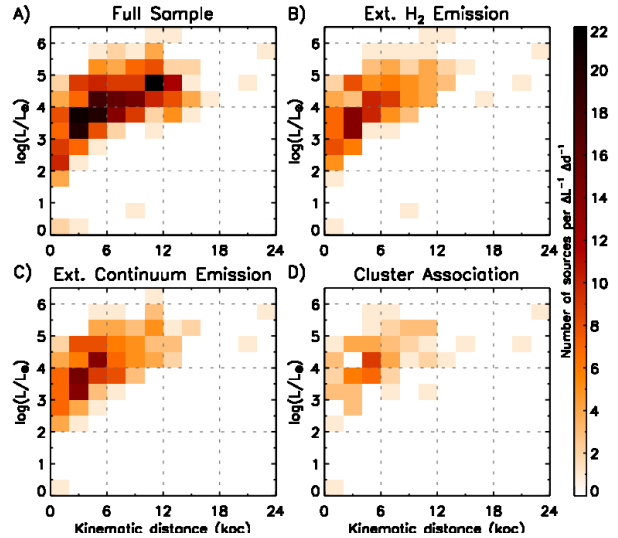


Figure 6. Global properties and results of the survey as a function of luminosity vs. distance. Each ‘pixel’ corresponds to a bin of $\Delta \log(L/L_{\odot}) = 0.5$, $\Delta d = 2.0$ kpc. The dashed lines are placed at $d = 6, 12$ and 18 kpc and $\log(L/L_{\odot}) = 2.0, 4.0$ and 6.0 . The colorbar at the right corresponds to the number of sources per each bin. Panel A: full sample; Panel B: subsample showing extended H₂ emission; Panel C: subsample showing extended continuum emission; Panel D: subsample associated with extant stellar clusters.

luminosity young stars, but not with the most luminous MYSOs. The K-type sources (Panel B) display a broader distribution towards high-luminosity sources and peak at high-luminosity sources ($\log(L/L_{\odot}) \sim 4.0$) located at distances closer than $d \lesssim 8$ kpc. The distribution of D-type sources (Panel C) is more restricted in the luminosity and distance ranges as compared to the BP- and K-type sources. The diffuse H₂ emission is associated with relatively closer ($d \lesssim 14$ kpc) mid- to high-luminosity sources [$\log(L/L_{\odot}) \gtrsim 2.5$]. That is, the radiative flux of the star must be sufficiently strong in order to generate diffuse emission. Diffuse emission has a lower surface brightness when compared to the knots or polar structures and it cannot be detected at larger distances. The non-detections distribution is shown in Panel D. This is the complementary plot of the one shown in Panel B from Figure 6. It indicates N-type sources peak towards high-luminosity sources at $d \sim 12$ kpc. Besides the peak toward larger distances, there are no significant differences between the distribution of detections and non-detections.

Finally, our data is not sufficient to prove the real nature of the increase of N-type sources towards larger distance when compared to other H₂ classes. It could be due to the fact that *i*) N-type sources may correspond to a different kind of source or are related to a specific environment or stage of massive star formation, or even *ii*) due to a systematic bias of the H₂ detection. It seems reasonable that N-type sources could include both radio quiet objects in the first stages of formation and even radio loud sources at the later stages of the pre-main sequence with no strong inflow/outflow activity. The truly non-detections of H₂ extended emission may include farther sources associated with unresolved structures. Excluding those sources associated with wrong kinematic distance values and considering the

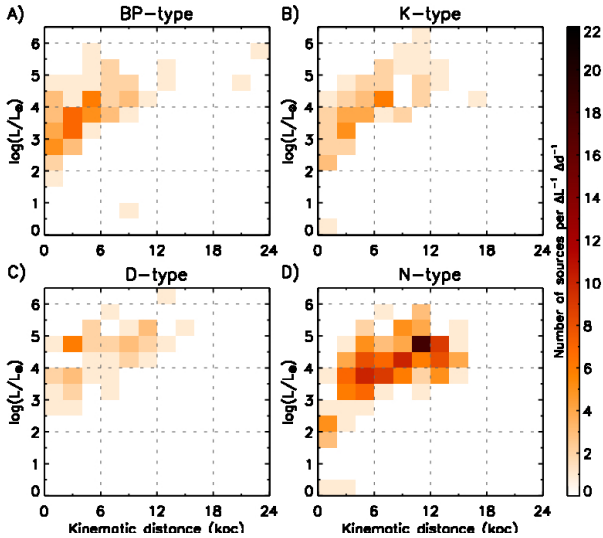


Figure 7. Two-dimensional histograms characterizing the distribution for each H_2 morphological class. Each ‘pixel’ corresponds to a bin of $\Delta \log(L/L_\odot) = 0.5$, $\Delta d = 2.0$ kpc. The colorbar at the right corresponds to the number of sources per each bin. Panels A, B, C and D present the distribution for BP-, K-, D- and N-type sources, respectively.

largest pixel scale of our observations (WIRCam has a pixel size of 0.3 arcseconds, see Section 2), it is possible to argue that we have clearly identified all the structures associated with the sources from our sample (located at distances up to ~ 15 kpc) with projected lengths greater than ~ 0.1 pc and brighter than the limiting sensitivity of our images (see details in Section 2).

3.6 Projected Length of the Structures

The projected length (ℓ_{proj} , in parsecs) of each structure was estimated as $\ell_{proj} \approx d \cdot \Delta\theta$, where d is the kinematic distance and $\Delta\theta$ is the angular size of the structure, measured on the direction of the flow. Table 3 presents the properties of each H_2 component. It contains the projected length and the position angle (PA, measured in relation of the center of each field and rotation in degrees E of N) for every diffuse, knot or polar H_2 emission structure identified on the fields. The ℓ_{proj} values measured for H_2 knots correspond to the distance from the knot to the RMS source. The aspect ratio ($R = \text{length}/\text{width}$) of the polar features is presented in the last column of the table. In order to estimate the aspect ratio of each H_2 polar structure, their width were measured perpendicularly to the direction of the flow, corresponding to the maximum projected width of the structure. The full version of this table containing 448 entries is available online at the CDS.

3.7 Sources exhibiting H_2 polar emission

The identification of polar structures driven by MYSOs is an observational signature of the accretion by circumstellar disks proposed by (Jijina & Adams 1996; Krumholz et al. 2005). Both the projected length (ℓ_{proj}) and aspect ratio ($R = \text{length}/\text{width}$) were determined for every polar emission

Table 3. Properties of the H_2 structures identified on each field.

ID	Component	ℓ_{proj} (pc)	PA ($^\circ$)	R
002	BP2(1a,b)	1.26, 0.91	50, 265	11.0, 8.0
002	D(2a,b)	3.96	200-320	-
003	D(1)	0.51	0-360	-
006	BP2(1a-f)	0.68, 0.74	70, 285	5.5, 5.9
006	K(2)	0.84	50	-
006	K(3)	0.68	290	-
007	K(1)	0.21	140	-
007	K(2)	0.50	105	-
006	K(4)	0.96	330	-
018	K(1)	0.40	305	-
018	K(2)	0.31	120	-
019	BP2(1a,b)	0.28, 0.34	315, 135	1.6, 3.1
022	D(1)	1.96	345-55	-
026	BP2(1a-h)	2.27, 2.27	125, 295	3.8, 11.0
034	K(1)	0.35	100	-
034	K(2)	0.31	0	-
034	K(3)	0.72	270	-
034	K(4)	0.65	180	-
034	K(5)	1.16	345	-
045	BP2(1a,1b)	0.76; 0.71	125, 300	2.1, 6.0

Notes. First 20 rows of the table. A full version containing 448 entries is available online at the CDS. The columns are – 1: source’s ID; 2: type of the structure (H_2 emission or cluster); 3: projected length of the structure; 4: the position angle (in degrees, measured from N to E); 5: the aspect ratio of polar structures. In the case of K-type components, ℓ_{proj} corresponds to the distance from the H_2 emission to the RMS source. For structures with two or more components, the measurements follow the same order of each label.

structure associated with each BP-type source. These values are shown in Table 3.

The quantity ℓ_{proj} is important in order to *i*) check any inconsistency on the determination of the kinematic distance associated with the source and *ii*) to identify relationships between the morphology of the extended emission and intrinsic characteristics of the driving source. Since it is a projected measurement, ℓ_{proj} corresponds to a lower limit of the real dimension of the structure ($\ell_{proj} = \ell_{real} \sin i$, where i is the inclination angle between the outflow axis and line-of-sight). The first statement needs further discussion. It is not expected to find ℓ_{proj} values greater than a few parsecs towards larger distances and, in these cases, there may be an inconsistency with the distance value. This seems to be the case of sources #164 and #165, located at the Galactic anti-centre ($l \sim 173^\circ$) and associated with a kinematic distance of 34.0 kpc. Table 3 displays a BP2-type emission located in the #164 region has $\ell_{proj} = 25$ pc and a D-type emission with $\ell_{proj} \sim 35$ pc in the same region. These values are much larger than the average projected length range of the structures found on this work (\sim few parsecs).

The 74 BP-type sources are shown in Appendix A. The H_2 maps for the other sources are available online at the CDS.

3.8 Sources associated with stellar clusters

Figure 3 indicates that 80 MYSO candidates ($\sim 23\%$ of the sample) are associated with potential stellar clusters.

Table 4. Properties of the potential stellar clusters identified on each field.

ID	RA (J2000)	Dec (J2000)	d (kpc)	ℓ_{proj} (pc)	$\Delta\theta$ (")
22	18 36 47	-07 35 39	9.6	0.85	20
34	18 43 46	-03 35 29	8.7	1.35	45
39	18 47 36	-02 01 50	9.1	0.95	25
66	19 07 01	08 18 44	11.2	0.47	20
81	19 44 24	25 48 43	15.9	0.96	15
85	20 21 55	39 59 45	4.5	0.70	35
87	20 29 37	39 01 15	4.5	0.95	40
88	20 19 40	40 56 33	3.8	1.08	60
91	20 29 25	40 11 19	4.7	0.60	30
99	20 38 56	42 22 41	3.7	0.62	40
104	20 38 37	42 37 20	1.2	0.58	100
107	20 42 34	42 56 51	1.0	0.26	55
112	21 31 45	51 15 35	5.6	1.25	45
115	21 15 55	54 43 30	10.7	0.73	20
118	21 43 02	54 56 20	7.9	1.25	30
120	21 52 57	56 39 54	7.4	0.52	15
121	22 16 10	52 21 34	4.8	0.58	25
124	22 55 29	57 09 24	6.1	0.80	30
126	22 58 45	58 47 00	5.5	2.40	60
127	22 59 03	59 28 25	5.3	0.88	55

Notes. First 20 rows of the table. A full version containing 80 entries is available online at the CDS. The columns are as follows – 1: source’s ID; 2: right ascension (J2000); 3: declination (J2000); 4: kinematic distance (based on the RMS source); 5: projected length of the cluster based in the kinematic distance (column 4) in parsecs; 6: angular diameter of the cluster in arcseconds.

The presence of MYSOs in these clusters suggests they may be very young ($\sim 10^5 - 10^6$ yr for an O9 star) due to the short timescale related to the massive star formation. The identification of clusters visible at near infrared wavelengths and associated with very young high mass objects is rare and the confirmation of such structures require follow up observations (e.g. deep J-, H- and K-band photometry) using high-angular resolution instruments in order to resolve the individual members of clusters located at distances of ~ 10 kpc. The list of cluster candidates is shown in Table B4. The table presents the central coordinates of the clusters, their angular size in arcseconds ($\Delta\theta$) and their projected diameter in parsecs (based on the kinematic distance of the RMS source in the same field). The full version of this table containing 80 entries is available at the CDS.

4 DISCUSSION

4.1 Near infrared colors

The association of each MSX source and a 2MASS counterpart was performed by Lumsden et al. (2002) in order to select the RMS sample. Thus, every positive association with a 2MASS counterpart should satisfy the criteria used by those authors, that is $J - K_s > 2.0$ mag and $F_{K_s}/F_8 > 5$, where F_8 corresponds to the flux measured at $8.3 \mu\text{m}$ in the MSX images. Two other criteria used for the mid-infrared fluxes are: $F_{21}/F_8 > 2$ and $F_8 < F_{14} < F_{21}$.

Each positive association of a MSX source and a 2MASS counterpart was included in the near infrared color-color (C-

C) diagram shown in Figure 8. The data points are distinguished by each H_2 morphological type, defined in Section 3.1. The locus of intrinsic colors for main sequence stars from Koornneef (1983) is shown as the continuous line. The dashed black line shows the location of Classical T Tauri Stars (CTTS) from Meyer et al. (1997). The black arrow corresponds to the reddening vector based on the Stead & Hoare (2009) reddening law. The black lines indicate the reddening vectors for M-type stars, O-type and CTTS. The region below the lower reddening line for the O-type stars is occupied by pre-main sequence (PMS) objects and the location of the most massive and young sources is located at higher $H-K_s$ values, to the right of the CTTS reddening line. The photometric errors given by the 2MASS catalog were estimated using the photometric error of each considered filter and the average error was estimated in 0.081 and 0.091 for the J–H and H– K_s colors, respectively.

Most of the objects in the NIR C-C diagram are located in the region occupied by PMS and MYSOs sources, that is, to the right of the O-type reddening line. This is a direct consequence of the MSX NIR color selection criteria from Lumsden et al. (2002, $J-K_s > 2.0$ mag). Approximately 20 sources are located to the left of the M-star reddening vector. The existence of sources in this region of the C-C diagram may be due to the incomplete NIR color criteria used to select the RMS sources: it is not based on individual J–H and H– K_s colors, but only on J– K_s . Another ~ 50 sources lie between the M-star reddening line and the red limit of the CTTS sequence. The last ~ 280 objects are located to the right of the CTTS reddening vector, displaying NIR colors expected for MYSO and low mass YSO candidates.

Figure 8 also displays the distribution of radio quiet/loud sources. Most of the radio loud sources display $J-H \lesssim 2.0$ mag while radio quiet sources are preferably associated with J–H values greater than 1.0 mag. Only 15 sources ($\sim 20\%$ of the radio loud subsample) have greater H-band excess. The median NIR colors for the radio quiet and loud subsamples are shown as larger black and blue crosses in Figure 8, respectively. The radio quiet subsample has $J-H_{med} = 2.02$ mag while the radio loud displays a smaller median excess, $J-H_{med} = 1.38$ mag. The median H– K_s colors are less discrepant (2.03 and 1.77 mag for the radio quiet and radio loud subsamples, respectively). These results are consistent with the fact that radio loud sources are bluer NIR objects when compared to the bulk of radio quiet ones due to the dissipation of the circumstellar medium, reducing the reddening and color excess at near-infrared wavelengths.

Comparing the distribution of each H_2 class on the NIR C-C diagram, we found that both K- (shown as triangles) and BP-type (shown as circles) sources have NIR colors compatible with low to highly reddened sources ($1.0 \lesssim A_K \lesssim 3.5$). There are only three K-type sources to the left side of the M-star reddening vector and three BP-type ones located in the same region. Although these sources are not compatible with reddened MS stars, some of the BP-type sources display higher H-band excess ($J-H \gtrsim 3.0$) when compared to K-type ones ($J-H \lesssim 3.0$). The presence of so many very reddened sources ($H-K_s \sim 4.0$) is consistent with the fact that most of the accretion occurs while the MYSO is still deeply embedded. D-type sources (shown as squares) occupy a region compatible with less reddened objects ($H-K_s \lesssim$

3.0) when compared to the BP- and K-type ones. There are only five D-type sources to the left of the M-star reddening vector. Finally, N-type sources (shown as plus symbols) do not appear to fall into any preferred region on the C-C diagram. The overall conclusion from Figure 8 is the absence of any well-defined region occupied by one of the classifications adopted in this work (either radio quiet/loud or H_2 classes).

4.2 MSX and IRAS colors

The MSX and IRAS color C-C diagrams are based on the logarithm of the flux ratios at different wavelengths [i.e. $\log(F_{14.6}/F_{8.3})$ and $\log(F_{60}/F_{12})$]. The mid-infrared (MIR) and far-infrared (FIR) C-C diagrams are shown in Figure 9. Data are shown using the same representation from Figure 8.

The MIR C-C diagram (Panel A) indicates most of the sample display $\log(F_{21.3}/F_{14.6})$ values between 0.0 and 1.2 and $\log(F_{14.6}/F_{8.3})$ between 0.0 and 0.8, being consistent with the MIR color criteria adopted by Lumsden et al. (2002) for the RMS sample selection ($F_{8.3} < F_{14.6} < F_{21.3}$). Varricatt et al. (2010) claimed that young sources in later phases (UCH II) should occupy the upper region of the $\log(F_{14.6}/F_{8.3})$ vs. $\log(F_{21.3}/F_{14.6})$ diagram and have steeper SEDs than the ones with active accretion (MYSOs). However, the median values of MIR color indexes for the radio quiet/loud subsamples indicate that radio loud sources are preferably found towards larger $\log(F_{21.3}/F_{14.6})$ values, but display similar $\log(F_{14.6}/F_{8.3})$ values than those found for radio quiet ones. In addition, we found that every radio loud source has $\log(F_{21.3}/F_{14.6}) > 0.25$.

Regarding the H_2 classes, Panel A from Figure 9 shows the ratio between BP- and K-type sources increases from larger $\log(F_{14.6}/F_{8.3})$ and $\log(F_{21.3}/F_{14.6})$ values towards smaller ones. Sources associated with diffuse H_2 emission (shown as square symbols) have a similar distribution as compared to radio loud sources. N-type sources do not display any preferred region in the Mid-IR C-C diagram.

The Far-IR C-C diagram (Panel B, Figure 9) indicates that all sources have positive FIR colors, indicating crescent SEDs at IRAS wavelengths (that is, the flux increases toward larger wavelengths). Only 5 radio loud sources are located outside the region delimited by the IRAS color criteria for UCH II regions, defined by Wood & Churchwell (1989) while radio quiet sources do not show any preferred region on the plot. As a function of the H_2 morphology, the Far-IR C-C diagram displays the fraction of sources outside the UCH II region (Wood & Churchwell 1989) increases from the D-type (only 3) to BP- ($\sim 19\%$), K- ($\sim 26\%$) and N-type ones ($\gtrsim 30\%$). Most of the D-type sources are located inside the area of UCH II regions. This is consistent with the fact that the diffuse emission may be originating from more evolved sources in a phase after the major accretion period. The Panel B from Figure 9 also indicates a correlation between D-type and radio loud sources. Combining this information with the fact that the D-type sources display a larger fraction of associations with stellar clusters (43.2%, Panel B from Figure 4), this suggests diffuse H_2 emission is a result of the global environment of the cluster and not a result of a single star.

The photometric analysis of the sample leads to the conclusion that *i*) most of the sources are located to the right

of the CTTS reddening line in the NIR C-C diagram, having colors compatible with young embedded objects. Radio quiet sources are preferably redder and dominate in the top part of the NIR C-C diagram (that is, they have greater J–H colors when compared to radio loud sources). No clearly NIR color criteria was found for any H_2 morphological class. *ii*) the MIR C-C diagram indicates the radio loud subsample is located toward $\log(F_{21.3}/F_{14.6})$ values greater than 0.25. and *iii*) most of the radio loud sources and those sources associated with diffuse H_2 emission are located inside the UCH II region in the Far-IR C-C diagram.

4.3 Polar structures and comparison with other samples

In order to check if we are dealing with some particular case of objects, we compared our results with the work from Varricatt et al. (2010), which present a smaller sample (50) of MYSO candidates. They found extended H_2 emission towards 38 of them (76%) and 25 sources were associated with polar H_2 structures, suggesting collimated jets. The fraction of the sources associated with extended H_2 emission and those which present polar structures are 1.5 and 2.4 times the values found in the present work (50.4 and 21%, respectively). This could be due to a selection effect of their sample: Their selection is based on sources that display high-velocity CO emission, which is largely used to detect emission from molecular outflows associated with young stars. Thus, there is a high probability that the sources associated with CO outflows would also exhibit a H_2 counterpart. Our survey was unbiased with respect to a prior knowledge of morphology type.

Figure 10 compares the distribution of the bolometric luminosity of the sources associated with polar structures (Panel A), the aspect ratio (R , Panel B) and the projected length (Panel C) of the polar structures driven by the BP-type sources and those found by Varricatt et al. (2010). Panel A shows the distribution of the number of sources per 0.5 dex bin of $\log(L/L_\odot)$ for the complete sample (353 objects, shown as black bars), the BP-type objects (74, grey bars) and those 25 identified by Varricatt et al. (2010, shown as black stripes). The present distribution and that of Varricatt et al. (2010) appear similar in the range of luminosity for BP-types, confirming that such polar structures are driven by both high and low luminosity sources. Panel B displays the aspect ratio of each polar component identified in both works. The data are shown as the fraction of the total number of structures (93 for the grey bars and 30 for the black striped bar, respectively). The histogram indicates the distribution of the R values for both samples is very similar. The median of each distribution is indicated by arrows and corresponds to $R = 4.8$ and 5.5 for the BP-type sources and Varricatt et al. (2010) sample, respectively. Panel C shows the distribution of the projected length of each polar structure. The plot suggests those structures identified by Varricatt et al. (2010) are relatively smaller than the ones found in the present work, although the shape of the distribution are very similar. These plots reveal that although the samples have different sizes, their global properties are very alike.

Figure 11 displays the distribution of the projected length of the polar structures as a function of the kinematic

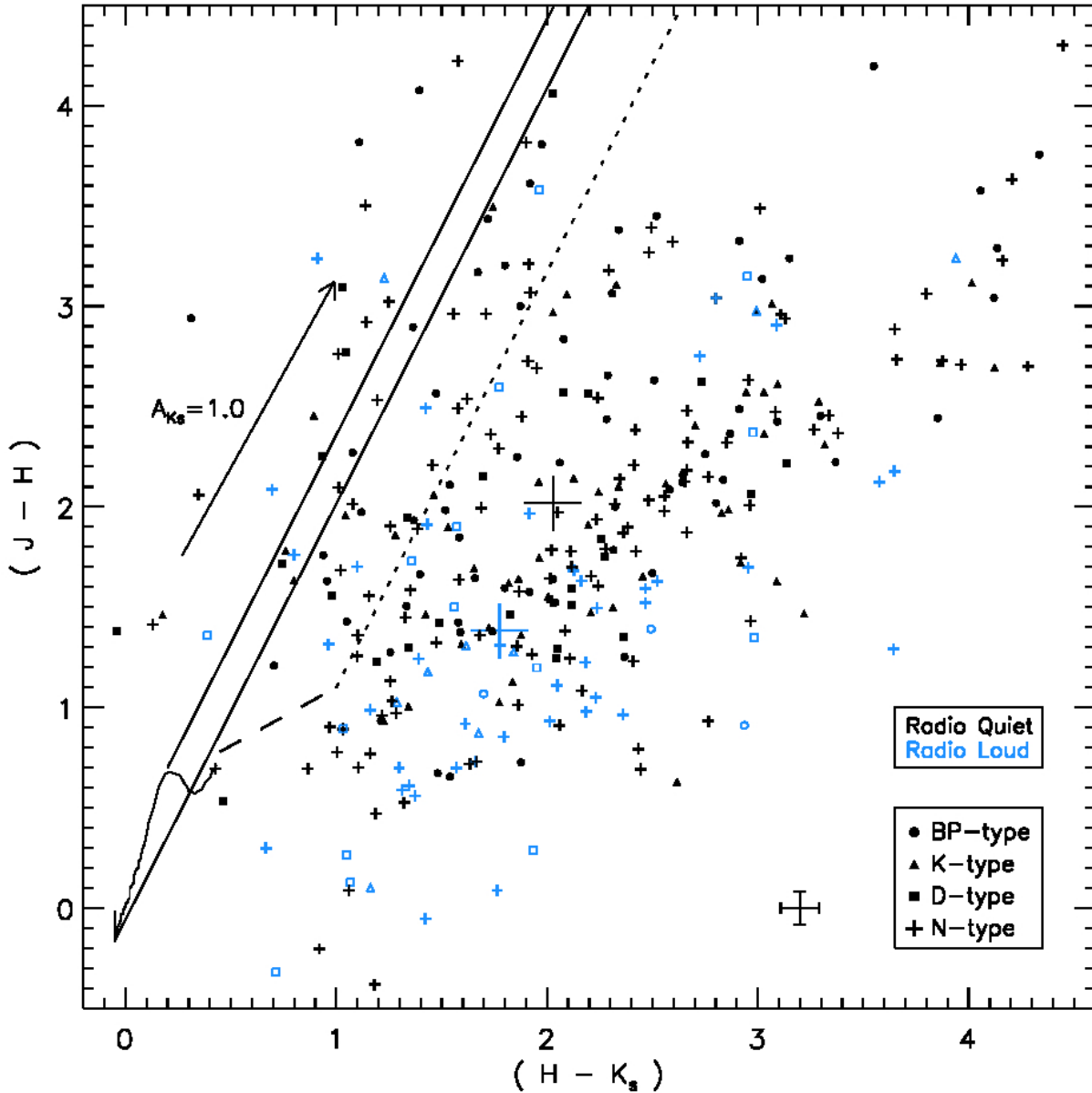


Figure 8. Near infrared color-color (C-C) diagram of the MYSO candidates with 2MASS counterparts. The black curve denotes the locii of the main sequence stars with $A_V = 0$ mag. The reddening vectors (shown as black lines) are from Stead & Hoare (2009) reddening law. The upper line corresponds to M-type stars, the middle line to O-type and the dashed lines indicate the CTTS zone. The arrow shown to the left of the M-type reddening line corresponds to $A_{K_s} = 1.0$ mag. Objects to the right of the reddening vectors have excess emission in the K_s -band and are likely embedded YSOs. Data are shown as a function of H_2 emission morphology: BP-type (\bullet), K-type (\blacktriangle), D-type (\blacksquare) and N-type ($+$). Radio quiet and radio loud sources are shown as filled black and opened blue symbols. The average photometric error of each color is shown at the bottom right corner of the plot. The larger black and blue crosses indicate the median values of radio quiet and radio loud subsamples, respectively.

distance (Panel A) and the bolometric luminosity of their driving sources (Panel B). Data from this work are shown as filled green circles while those from Varricatt et al. (2010) are shown as red opened circles. Panel A displays that smaller structures ($\ell_{proj} \sim 0.1$ pc) are found toward the entire distance range within the sample. A lack of larger structures was found towards closer distances than 1 kpc and a relative increase of the lower limit value of ℓ_{proj} was found for $d >$

5 kpc. The increasing of the lower limit is explained due to the difficult on identifying smaller structures towards farther distances and does not provide us any insight on the physical processes that are driving the outflows. The upper limit of the structures reveals two different regions on the distance domain: *i*) for $d < 1$ kpc, indicating the incompleteness of our survey towards closer distances and due the absence of massive star formation in the Solar neighbourhood; and *ii*)

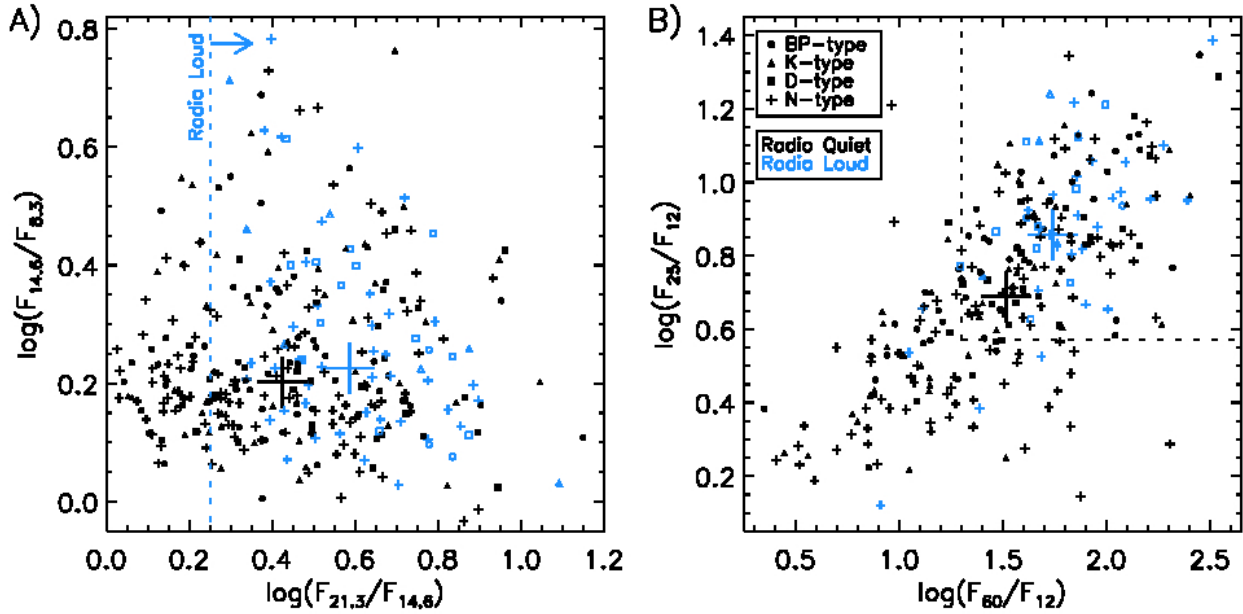


Figure 9. Panel A: Mid-infrared C-C diagram of the MYSO candidates with MSX fluxes. Panel B: Far-infrared C-C diagram of the MYSO candidates with IRAS fluxes. The C-C diagrams are based on the logarithm of the flux ratio at different wavelengths. On both plots, data are shown as a function of H_2 emission morphology: BP-type (\bullet), K-type (\blacktriangle), D-type (\blacksquare) and N-type ($+$). Filled black symbols correspond to radio quiet sources while opened blue symbols are radio loud ones. The dashed red line shown in Panel A corresponds to the $\log(F_{21.3}/F_{14.6})$ value limit for the radio loud sources. The dashed lines shown in Panel B mark the IRAS color criteria for UCH II regions, defined by Wood & Churchwell (1989).

for distances greater than 1 kpc, which indicates a relatively constant upper limit of $\ell_{proj} \sim$ few pc. There are 5 points at $d \sim 20$ kpc with $\ell_{proj} \sim 10$ pc. These points correspond to structures associated with sources #162 and #163 (shown in Appendix A), located at $\ell \sim 173^\circ$. As discussed in Section 3.7, six of our targets (#161, #162, #163, #164, #165 and #166) are located at $\ell \sim 170^\circ$. They are associated to distances farther than 16 kpc, which is larger than the expected Galactic distances at this longitudinal region. As reported by Urquhart et al. (2009a), kinematic distances of sources located closer to the Galactic anti-centre are very uncertain.

Panel B displays the same data but as a function of the bolometric luminosity of the driven source. Those points associated with uncertain Galactic distances are placed at $\log(L/L_\odot) \approx 4.6$ and 5.5 and are excluded from the overall analysis. The analysis of the Panel B is alike of that from the previous plot. Small projected lengths are found towards the entire bolometric luminosity range and the lower limit of ℓ_{proj} does not provide any important information. On the other hand, the upper limit of ℓ_{proj} traces two different regions: the first one, due to the incompleteness of our sample towards low-luminosity sources ($\log(L/L_\odot) \lesssim 2.5$), are limited by $\ell_{proj} \lesssim 0.3$ pc; for higher luminosities, the upper limit is roughly 10 times larger ($\ell_{proj} \lesssim 3.0$ pc). Liu, Ho & Zhang (2010) derives the statistical average value of the inclination angle of a randomly distribution of outflows and found $\langle i \rangle = 0.637$ rad, or $\langle i \rangle = 36.5^\circ$. That is, most of the ℓ_{proj} values corresponds to physical lengths 1.68 times larger as the same as their aspect ratio (that is, the outflows are likely to be larger and more collimated than their measured values).

Data from Varricatt et al. (2010) are within the range of

the luminosity, distance and projected length of the structures identified in the present work, indicating that both samples are consistent. The overall conclusion from Figure 11 is that the largest outflows associated to high-luminosity sources are limited to a few parsec of extension, suggesting the size of the jets may not scale with intrinsic characteristics of their driven source.

The distribution of the aspect ratio (length/width) of each polar structure is shown in Figure 12. Panel A indicates that highly collimated ($R \gtrsim 10$) structures driven by BP-type sources are found over the entire range of luminosities while the Varricatt et al. (2010) sample only displays three highly collimated structures driven by $3 \lesssim \log(L/L_\odot) \lesssim 4.5$ sources. Our sample presents several polar structures driven by high-luminosity ($\log(L/L_\odot) \gtrsim 4.0$) and less collimated ($R \lesssim 3.5$) sources than included in the sample of Varricatt et al. (2010). This may simply reflect the smaller sample size. The Spearman correlation rank for data shown in Panel A (correlation factor of 0.0147) indicates a weak correlation between R values as a function of the luminosity of the driving source. It is likely that R is a lower limit of the real aspect ratio ($R \lesssim R_{real}$) since it is based on a projected value of the true length of the structures (that is, $\ell_{proj} \lesssim \ell_{real}$).

Panel B displays the distribution of R as a function of the kinematic distance of its driving source. In this plot, we found highly collimated outflows for distances greater than 2 kpc while less collimated ones are found between 1 and 10 kpc. The plot indicates a poor correlation between the aspect ratio and distance values (Spearman rank correlation factor of -0.02). Panel C indicates that the projected length of these less collimated structures is more variable (larger width of the distribution) on scales from 0.1 to

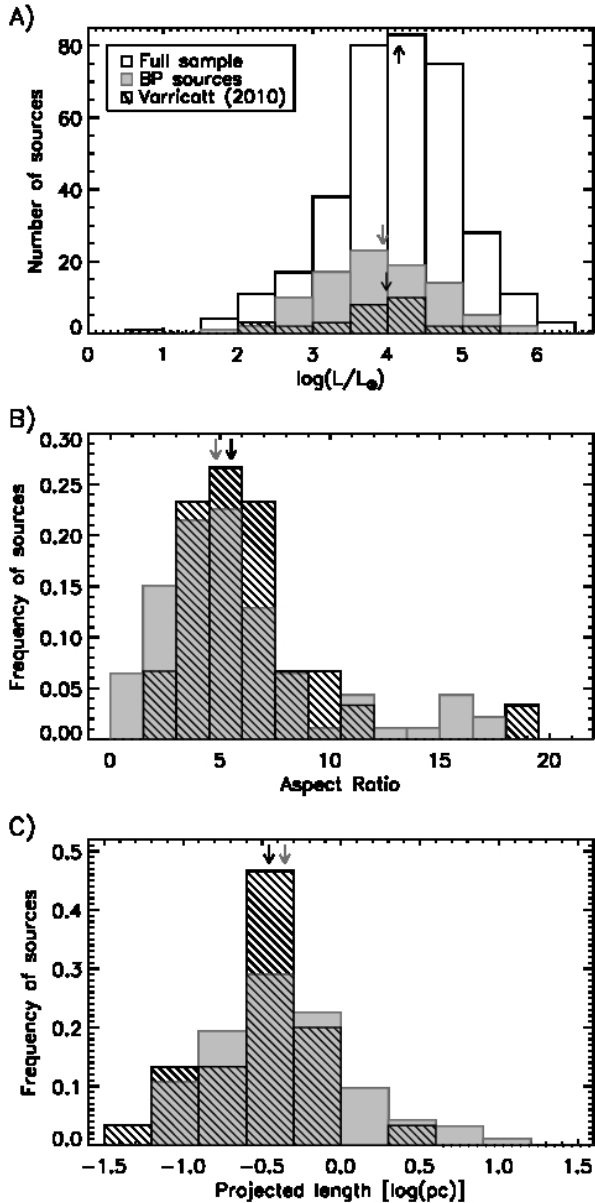


Figure 10. Distribution of the full sample (black bars), sources classified as BP-type (grey bars) and sources associated with polar structures identified by Varricatt et al. (2010, shown as black striped bars). Panel A: histogram of the bolometric luminosity using a binning of 0.5 dex; Panel B: distribution of the aspect ratio of each polar component assuming a binning of $\Delta R = 1.5$; Panel C: distribution of the projected length (in logarithmic units) of each structure using a binning of 0.3 dex. The arrows shown in the plots indicate the median values of each sample.

~ 1.0 pc, while the highly collimated outflows are associated with both smaller (~ 0.1 pc) and larger structures (~ 10 pc). There are no data between with $\ell_{proj} \gtrsim 1.0$ pc and $R \lesssim 3$. The absence of structures with these properties indicates that the mechanism that produces wider outflows is not able to sustain its structure towards larger length scales.

The overall analysis of Figure 12 indicates that both samples contains analogous structures, although several of those identified in this work are less collimated than those identified by Varricatt et al. (2010). On the other hand, there

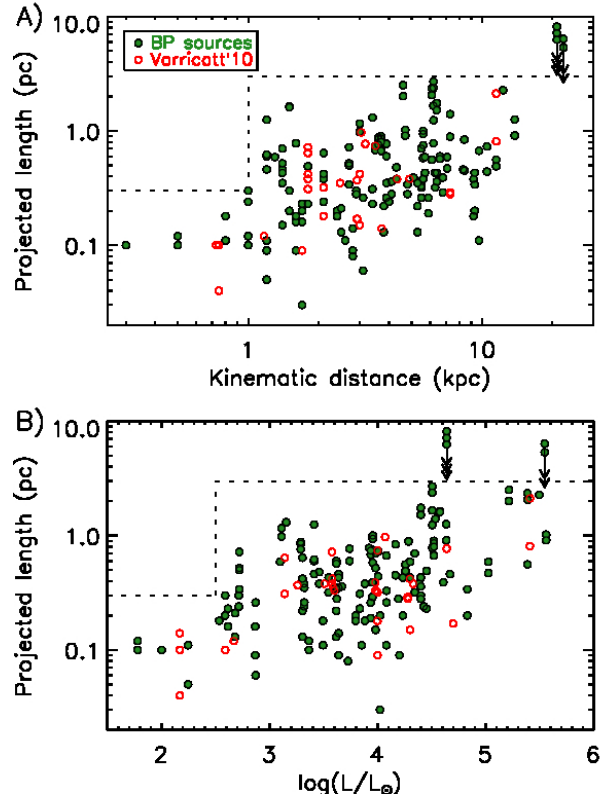


Figure 11. Distribution of the polar structures associated with BP-type objects as a function of the kinematic distance (Panel A) and the bolometric luminosity of the associated RMS source (Panel B). Data from this work is shown as filled green circles while those from Varricatt et al. (2010) is indicated by opened red circles. Filled black and red lines correspond to tentative fittings of our and Varricatt data, respectively. Dashed lines are placed at $d = 1.0$ kpc and $\log(L/L_{\odot}) = 2.5$, indicating a changing in the upper limit of ℓ_{proj} . Data associated with black arrows indicates the upper limit of the values due to problems on the kinematic distance determination (see text for details).

is no correlation between the aspect ratio of the polar emission and the bolometric luminosity of their driving sources.

4.4 Masses of the outflows

An outflow with length equal to its projected length (ℓ_{proj}) and its width given by $\Delta w \approx \ell_{proj}/R$ could be approximated by a conical structure with volume $V = \pi \cdot \Delta w^2 \cdot \ell_{proj}/3 = \pi \ell_{proj}^3/3R^2$. Assuming a typical density of an outflow associated with a massive young star ($n = 10^3 - 10^4 \text{ cm}^{-3}$ Codella et al. 2013), one can estimate the outflow mass, $M_{out} = V \cdot n \cdot m_{H_2}$, where m_{H_2} corresponds to the H_2 molecular mass. In terms of the observable quantities, we have $M_{out} = 4.3 \left(\frac{\ell_{proj}}{1.0 \text{ pc}} \right)^3 \left(\frac{R}{3.0} \right)^{-2} \left(\frac{n}{10^3 \text{ cm}^{-3}} \right) M_{\odot}$.

Figure 13 displays the outflow mass (M_{out}) in solar mass units as a function of the bolometric luminosity (Panel A) and the mass of its driving source (assuming $L \propto M^{3.5}$, Panel B). M_{out} was estimated assuming the minimum (shown as opened circles) and maximum density (shown as filled circles) from Codella et al. (2013, $n = 10^3 - 10^4 \text{ cm}^{-3}$). The maximum and minimum values determined for a sin-

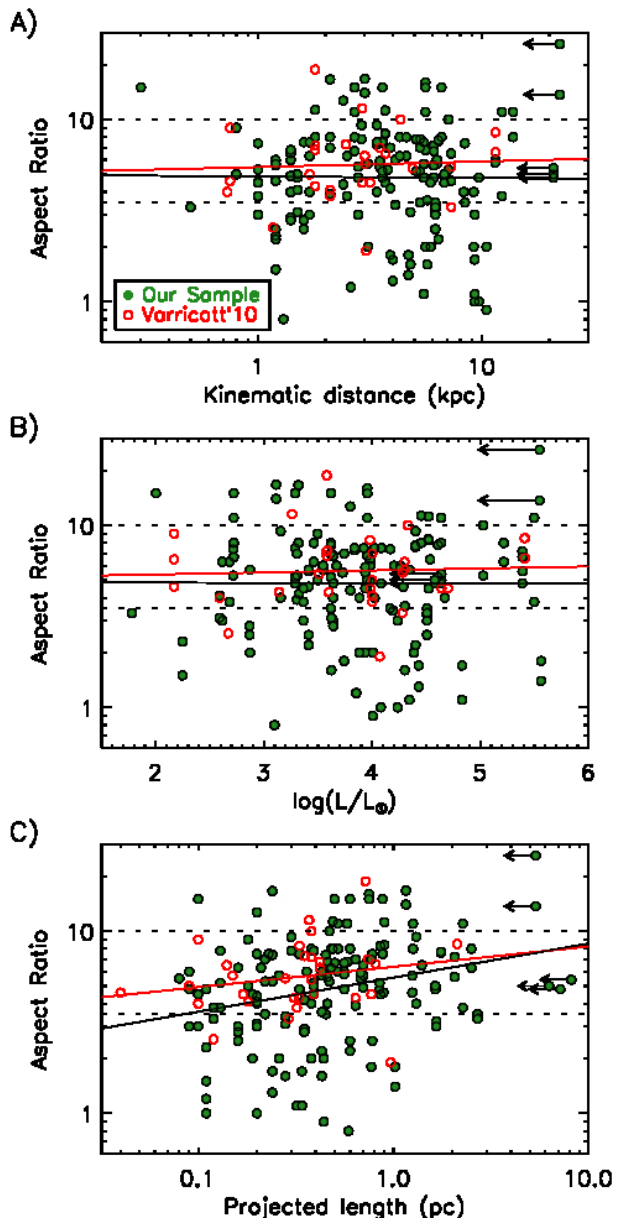


Figure 12. Distribution of the aspect ratio of the polar emission associated with BP-type sources. The data are shown as a function of the logarithm of the kinematic distance (Panel A) and as a function of the luminosity of the associated RMS source (Panel B), and as a function of the projected length of each structure (Panel C). Data from this work is shown as filled green circles while those from Varricatt et al. (2010) are shown as opened red circles. The horizontal dashed lines corresponds to $R=3.5$ and $R=10.0$. Filled black and red lines correspond to tentative fittings of our and Varricatt data, respectively. Data associated with black arrows indicates the upper limit of the values due to problems on the kinematic distance determination (see text for details).

gle point are connected by a gray line. In case of multiple components, the mass of each component was summed and, thus, M_{out} corresponds to the total outflow mass ejected by the source. The plots also display the median mass out flow values for the following mass ranges (and corresponding luminosity ranges): 0-4, 4-8, 8-15, 15-20, 20-30 and 30-40 M_{\odot} (and for both values of density). The green shadowed re-

gion is delimited by the maximum (shown as filled triangles and connected by the filled green line) and minimum masses (shown as open triangles and connected by the dashed green line). Panel A shows M_{out} ranges from 10^{-2} to $10^5 M_{\odot}$. The data have a larger dispersion between $\log(L/L_{\odot}) \sim 3$ and ~ 5 , where most of the BP-sources are located, but the median values clearly indicate a tendency for M_{out} to increase with the bolometric luminosity of the driving source ($M_{out} \propto L^{\alpha}$, with $\alpha \approx 1.15$). Panel B displays the outflow mass as a function of the mass of its driving source. This plot indicates a slight increase of the M_{out} value as a function of the central mass star. It is expected that most of the mass not transferred to the central star is ejected in an outflow. In another words, one can estimate the efficiency of the star formation assuming that $\eta = M_{star}/(M_{star} + M_{out})$. Panel C displays the star formation efficiency as a function of the central mass. The median values indicate that η decreases toward high mass stars. Most of the stars with $M \lesssim 15 M_{\odot}$ display η values higher than 70%, even considering the highest density for the outflows. The efficiency starts to decrease to 50% for $M \sim 15 - 20 M_{\odot}$, and displays the lowest values for $M \sim 30 - 40 M_{\odot}$. That is, giant molecular clouds with masses $\sim 1000 M_{\odot}$ are necessary to form very massive stars. Krumholz et al. (2009) have simulated the formation of a binary system with 41.5 and 29.2 M_{\odot} from an initial cloud with $M=100 M_{\odot}$. The process ended with $\eta = 70\%$ without considering any mass loss by outflow effects. The authors suggests that if one considers outflow activity, this value should drop to $\eta \sim 50\%$. These points are shown in Panel C as red triangles. Comparing with our observations, the efficiency determined by Krumholz et al. (2009) is reasonable for the $\sim 30 M_{\odot}$ star but is higher than observed for the $\sim 40 M_{\odot}$ one.

4.5 Collimation effects at different luminosity ranges

The last sections have shown that young stellar objects in different luminosity ranges drive outflows with indistinguishable aspect ratios, although the largest outflows are found for the most luminous sources. In order to study the intrinsic properties of the outflows, we must compare a high-luminosity MYSO with a low-luminosity one, located nearby each other and relatively close to the sun. G109.8715+02.1156 (#129, Fig. A129), also known as Cepheus A (Rodriguez et al. 1994; Torrelles et al. 1996), is a high-luminosity source ($\log(L/L_{\odot}) = 4.58$) located at $d=1.5$ kpc. G110.4771+01.4803 (#132, Fig. A132), known as Cepheus E (Lefloch et al. 1996) is an intermediate mass star ($\log(L/L_{\odot}) = 2.59$) located in the same region of the sky and with the same kinematic distance. Both sources shares the same physical scale shown in Figure 14. The high-luminosity source Cepheus A displays a bipolar outflow oriented in the E-W direction. The east lobe has a projected length of $\ell_{proj} = 1.64$ pc and its aspect ratio was estimated as $R=4.8$. The lower-luminosity source Cepheus E exhibits a bipolar outflow oriented in the N-S direction. The southern lobe has a projected length of $\ell_{proj} = 0.20$ pc and its aspect ratio is $R = 3.1$.

Figure 14 displays both sources aligned in the same direction and sharing the same physical scale. The H_2 map of Cepheus A exhibits several inner components within the

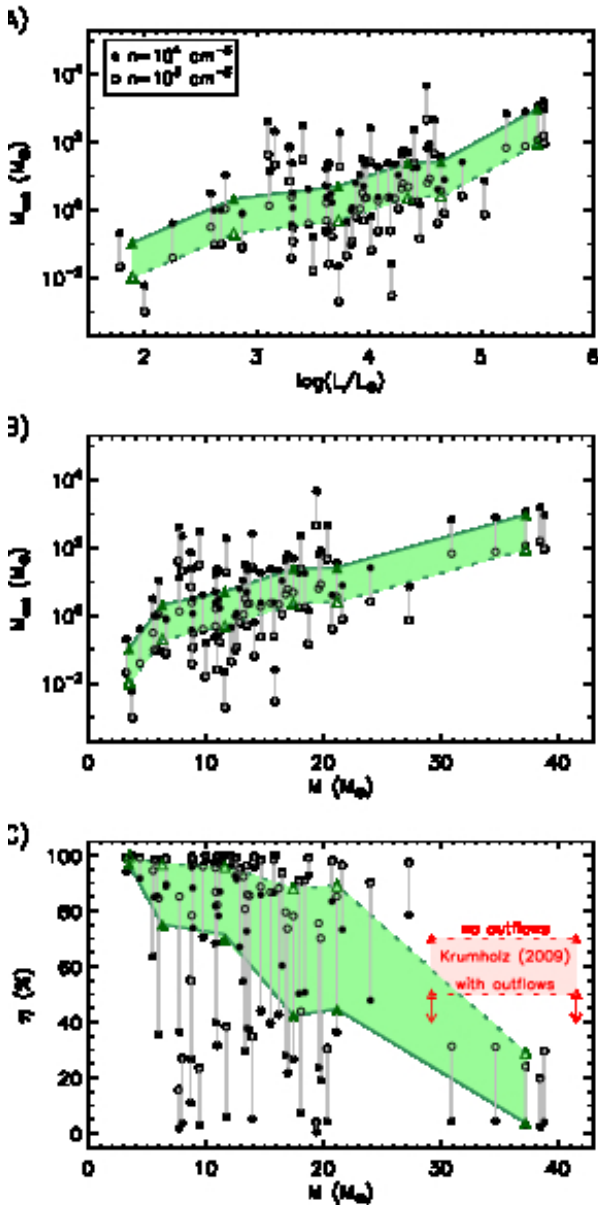


Figure 13. Distribution of the outflow mass associated with each as a function of the bolometric luminosity (Panel A) and the central mass (Panel B) for the BP-type sources. Panel C displays the star formation efficiency as a function of the central mass. Filled and opened circles correspond to the maximum and minimum particle density of the outflows, respectively. Median values of the mass of the out flow for each mass range (0-4, 4-8, 8-15, 15-20, 20-30 and 30-40 M_{\odot}) are shown as green triangles and are connected by green lines (filled/solid for the higher density). Data from Krumholz et al. (2009) are shown as red triangles and connected by dashed red lines. Filled symbols indicate the results without considering outflow effects while the opened symbols indicate the efficiency if outflow activity was included.

main structure of the bipolar outflow, suggesting either the driving source has a considerable precessing motion or even there are multiple sources producing outflows in the same region. This effect was not observed for Cepheus E, which exhibits a well defined single outflow structure. Previously, we showed that larger structures are driven by high luminosity

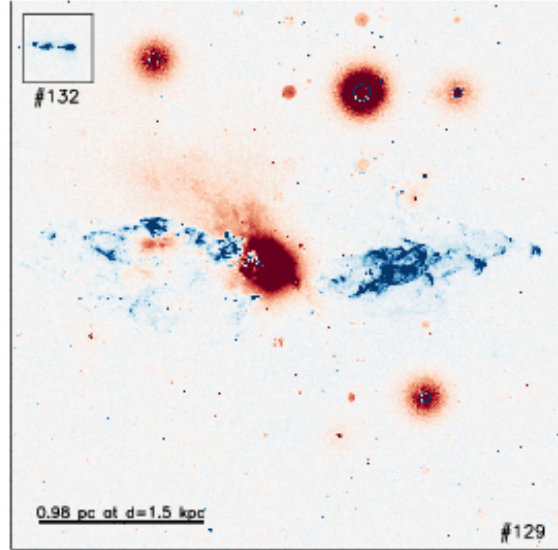


Figure 14. Comparison between bipolar outflows driven by a MYSO (Cepheus A, source #129, $\log(L/L_{\odot}) = 4.58$) and a YSO (Cepheus E, source #132, $\log(L/L_{\odot}) = 2.59$), both located in the Cepheus region at the same kinematic distance ($d=1.5$ kpc). Both H₂-maps are within the same scaling, indicated by the horizontal ruler in the bottom left side of the image. Cep E inset has been rotated through 90 deg, so N is to the left.

sources and that there are no structures larger than ~ 1.0 pc with aspect ratio values smaller than $R \sim 3.0$. Thus, both precession and the presence of multiple and active sources driving outflows would produce an enlargement of the global aspect ratio of the observed structure, such as the case for Cepheus A. Recently, Peters et al. (2014) have reproduced the global properties of the Cepheus A outflow on a three-dimensional simulation considering individual jets from multiple embedded stellar sources. This suggests some of the BP features may be classified as having low collimation when in fact the individual flows are highly collimated but enlarged by the effect of multiple sources and so appearing to have a broader opening morphology.

5 SUMMARY AND CONCLUSIONS

We have presented observations of 353 MYSO candidates observed through H₂ $\nu=1-0$ S(1) and continuum narrow-band filters. We use the angularly resolved images to characterize the nature of massive young stellar objects (MYSOs) with an eye to understanding the formation mechanism of massive stars. This work confirms and extends the results of Varricatt et al. (2010).

The analysis of our observations lead to the following conclusions:

- (i) 178 of the sources ($\approx 50\%$) display extended H₂ emission: 21% exhibit polar structures, 17% are associated with knots or amorphous H₂ emission and $\approx 12\%$ corresponds to diffuse H₂ emission;
- (ii) 74 of MYSOs with H₂ emission ($\approx 21\%$) exhibit collimated structures and bipolar outflows and most of these are

so called radio quiet sources (i.e. not compact or extended H II regions). The association with collimated outflows is taken as observational evidence for the accretion scenario and suggests that MYSOs are formed through disc accretion (as for low mass YSOs) and most of the accretion occurs on timescales less than 10^5 years;

(iii) the data suggest that larger outflow structures are found toward high-luminosity sources. The low-luminosity sources cannot drive very large outflows or even be associated with diffuse emission, which requires higher radiative fluxes;

(iv) the data do not display a clearly correlation between the size of the outflow structures and the properties of their driven source. The upper limit of the projected lengths of the outflows is roughly constant (a few parsecs) for a large range of bolometric luminosity;

(v) the low-luminosity sources exhibit smaller outflows (~ 0.1 pc) and are not associated with diffuse H_2 emission, which requires higher radiative fluxes;

(vi) there is no correlation between the aspect ratio (length/width of the flow) of the polar structures and the bolometric luminosity of their driving sources;

(vii) our data show a lack of poorly collimated large outflows, suggesting that the structure of the outflows cannot be maintained/supported by an ejection flux driven at very broad opening angles;

(viii) Considering the mass enclosed by the outflows, we found that the star formation efficiency decreases towards high-mass stars, indicating they expel up to ~ 10 times the amount of mass accreted into the central source;

(ix) Only $\approx 25\%$ of the sample (89) is associated with infrared-visible stellar clusters. Two of these sources are associated with polar H_2 emission.

ACKNOWLEDGMENTS

FN is grateful to CNPq and FAPESP support. AD and CLB acknowledge FAPESP for continuous financial support. We thank Sergio Scarano Jr., Cristina Armond and Tiago Ribeiro, who dedicated much effort to obtaining high-quality imaging for SOAR programs and Eder Martioli, Karun Thanjavur for the same effort on CFHT programs. We acknowledge all the discussion and suggestions given by the TERAPIX team which were very helpful.

We also thank the comments and suggestions made by the anonymous referee, which improved the quality of the revised version of this article.

Based on observations obtained with WIRCcam, a joint project of CFHT, Taiwan, Korea, Canada, France, and the Canada-France-Hawaii Telescope (CFHT) which is operated by the National Research Council (NRC) of Canada, the Institut National des Sciences de l'Univers of the Centre National de la Recherche Scientifique of France, and the University of Hawaii.

Based on observations obtained at the Southern Astrophysical Research (SOAR) telescope, which is a joint project of the Ministério da Ciência, Tecnologia, e Inovação (MCTI) da República Federativa do Brasil, the U.S. National Optical Astronomy Observatory (NOAO), the University of North Carolina at Chapel Hill (UNC), and Michigan State University (MSU).

This research has made use of the VizieR catalogue access tool, CDS, Strasbourg, France.

REFERENCES

- Bachiller R., 1996, ARAA, 34, 111
 Bally J., Reipurth B., Walawender J., Armond T., 2002, AJ, 124, 2152
 Bally J., Zinnecker H., 2005, AJ, 129, 2281
 Bertin E., 2006, in Gabriel C., Arviset C., Ponz D., Enrique S., eds, Astronomical Data Analysis Software and Systems XV Vol. 351 of Astronomical Society of the Pacific Conference Series, Automatic Astrometric and Photometric Calibration with SCAMP. p. 112
 Bertin E., Arnouts S., 1996, A&As, 117, 393
 Beuther H., Schilke P., Sridharan T. K., Menten K. M., Walmsley C. M., Wyrowski F., 2002, A&A, 383, 892
 Beuther H., Zhang Q., Sridharan T. K., Chen Y., 2005, ApJ, 628, 800
 Bik A., Thi W. F., 2004, A&A, 427, L13
 Blum R. D., Barbosa C. L., Damineli A., Conti P. S., Ridgway S., 2004, ApJ, 617, 1167
 Bonnell I. A., Bate M. R., Clarke C. J., Pringle J. E., 2001, MNRAS, 323, 785
 Bonnell I. A., Bate M. R., Zinnecker H., 1998, MNRAS, 298, 93
 Bontemps S., Andre P., Terebey S., Cabrit S., 1996, A&A, 311, 858
 Churchwell E., 2002, ARAA, 40, 27
 Codella C., Beltrán M. T., Cesaroni R., Moscadelli L., Neri R., Vasta M., Zhang Q., 2013, A&A, 550, A81
 Davies B., Lumsden S. L., Hoare M. G., Oudmaijer R. D., de Wit W., 2010, MNRAS, 402, 1504
 Depoy D. L., Atwood B., Byard P. L., Frogel J., O'Brien T. P., 1993, in Fowler A. M., ed., Infrared Detectors and Instrumentation Vol. 1946 of Society of Photo-Optical Instrumentation Engineers (SPIE) Conference Series, Ohio State Infrared Imager/Spectrometer (OSIRIS). pp 667–672
 Erben T., Schirmer M., Dietrich J. P., Cordes O., Haberbzettel L., Hettterscheidt M., Hildebrandt H., Schmithuesen O., et al., 2005, Astronomische Nachrichten, 326, 432
 Hanson M. M., Howarth I. D., Conti P. S., 1997, ApJ, 489, 698
 Jijina J., Adams F. C., 1996, ApJ, 462, 874
 Kim K., Kurtz S. E., 2006, ApJ, 643, 978
 Koornneef J., 1983, A&A, 128, 84
 Kroupa P., 2007, in Vazdekis A., Peletier R., eds, IAU Symposium Vol. 241 of IAU Symposium, The stellar initial mass function. pp 109–119
 Krumholz M. R., Klein R. I., McKee C. F., Offner S. S. R., Cunningham A. J., 2009, Science, 323, 754
 Krumholz M. R., McKee C. F., Klein R. I., 2005, ApJ, 618, L33
 Lefloch B., Eisloffel J., Lazareff B., 1996, A&A, 313, L17
 Liu H. B., Ho P. T. P., and Zhang Q., 2010, ApJ, 725, 2190
 Loh E. D., Biel J. D., Davis M. W., Laporte R., Loh O. Y., Verhanovitz N. J., 2012, PASP, 124, 343
 López-Sepulcre A., Codella C., Cesaroni R., Marcelino N., Walmsley C. M., 2009, A&A, 499, 811

- Lumsden S. L., Hoare M. G., Oudmaijer R. D., Richards D., 2002, *MNRAS*, 336, 621
- Martí J., Rodríguez L. F., Reipurth B., 1998, *ApJ*, 502, 337
- Martins F., Schaerer D., Hillier D. J., 2005, *A&A*, 436, 1049
- Meyer M. R., Calvet N., Hillenbrand L. A., 1997, *AJ*, 114, 288
- Moisés A. P., Daminieli A., Figuerêdo E., Blum R. D., Conti P. S., Barbosa C. L., 2011, *MNRAS*, 411, 705
- Mottram J. C., et al., 2011, *A&A*, 525, A149+
- Murakawa K., Lumsden S. L., Oudmaijer R. D., Davies B., Wheelwright H. E., Hoare M. G., Ilee J. D., 2013, *MNRAS*, 436, 511
- Navarete F., Figueredo E., Daminieli A., Moisés A. P., Blum R. D., Conti P. S., 2011, *AJ*, 142, 67
- Palla F., 1996, in Beckwith S., Staude J., Quetz A., Natta A., eds, *Disks and Outflows Around Young Stars Vol. 465 of Lecture Notes in Physics*, Berlin Springer Verlag, *The Quest for Evolutionary Diagrams of Young Stellar Objects (Review)*. p. 143
- Panagia N., 1973, *AJ*, 78, 929
- Peters T., Klaassen P. D., Mac Low M.-M., Schrön M., Federrath C., Smith M. D., Klessen R. S., 2014, *ApJ*, 788, 14
- Puget P., Stadler E., Doyon R., Gigan P., Thibault S., et al., 2004, in A. F. M. Moorwood & M. Iye ed., *Society of Photo-Optical Instrumentation Engineers (SPIE) Conference Series Vol. 5492 of Presented at the Society of Photo-Optical Instrumentation Engineers (SPIE) Conference*, WIRCam: the infrared wide-field camera for the Canada-France-Hawaii Telescope. pp 978–987
- Richer J. S., Shepherd D. S., Cabrit S., Bachiller R., Churchwell E., 2000, *Protostars and Planets IV*, pp 867–+
- Rodríguez L. F., Garay G., Curiel S., Ramirez S., Torrelles J. M., Gomez Y., Velazquez A., 1994, *ApJL*, 430, L65
- Schirmer M., 2013, *ApJS*, 209, 21
- Shepherd D. S., Churchwell E., 1996, *ApJ*, 457, 267
- Shepherd D. S., Testi L., Stark D. P., 2003, *ApJ*, 584, 882
- Shu F. H., Adams F. C., Lizano S., 1987, *ARAA*, 25, 23
- Skrutskie M. F., Cutri R. M., Stiening R., Weinberg M. D., et al., 2006, *AJ*, 131, 1163
- Sollins P. K., Hunter T. R., Battat J., Beuther H., Ho P. T. P., Lim J., Liu S. Y., Ohashi N., Sridharan T. K., Su Y. N., Zhao J.-H., Zhang Q., 2004, *ApJL*, 616, L35
- Stahler S. W., Palla F., Ho P. T. P., 2000, *Protostars and Planets IV*, pp 327–+
- Stead J. J., Hoare M. G., 2009, *MNRAS*, 400, 731
- Torrelles J. M., Gomez J. F., Rodríguez L. F., Curiel S., Ho P. T. P., Garay G., 1996, *ApJL*, 457, L107+
- Urquhart J. S., Busfield A. L., Hoare M. G., Lumsden S. L., Clarke A. J., Moore T. J. T., Mottram J. C., Oudmaijer R. D., 2007, *A&A*, 461, 11
- Urquhart J. S., et al., 2007, *A&A*, 474, 891
- Urquhart J. S., et al., 2008, *A&A*, 487, 253
- Urquhart J. S., et al., 2009a, *A&A*, 501, 539
- Urquhart J. S., et al., 2009b, *A&A*, 507, 795
- Urquhart J. S., Morgan L. K., Figura C. C., Moore T. J. T., Lumsden S. L., Hoare M. G., et al., 2011, *MNRAS*, 418, 1689
- Vaidya B., Fendt C., Beuther H., Porth O., 2011, *ApJ*, 742, 56
- Varricatt W. P., Davis C. J., Ramsay S., Todd S. P., 2010, *MNRAS*, 404, 661
- Wood D. O. S., Churchwell E., 1989, *ApJ*, 340, 265
- Wu Y., Wei Y., Zhao M., Shi Y., Yu W., Qin S., Huang M., 2004, *A&A*, 426, 503
- Zhang Q., Hunter T. R., Brand J., Sridharan T. K., Cesaroni R., Molinari S., Wang J., Kramer M., 2005, *ApJ*, 625, 864

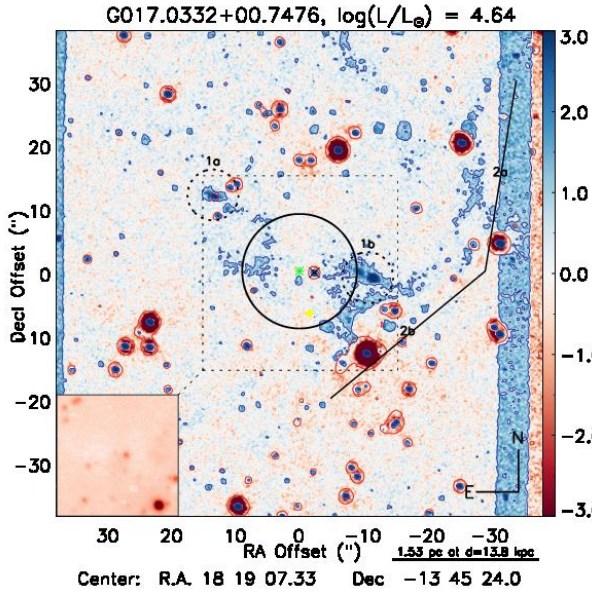


Figure A2. G017.0332+00.7476, $\log(L/L_\odot) = 4.64$, $d=13.8$ kpc, Sp. Type: O9.5 V, $H-K_s = 1.26$ mag. BP2(1a,1b): 1.26, 0.91 pc; 50° , 265° ; $R=11.0$, 8.0 ; $D(2a,2b)$: 3.96 pc; $200-320^\circ$.

APPENDIX A: INDIVIDUAL COMMENTS ON THE SOURCES WITH EXTENDED H_2 EMISSION

The mass-luminosity relation $L \propto M^{3.5}$ was adopted for an estimation of the central mass. The spectral type was inferred using the relations given by Martins et al. (2005) and Panagia (1973) for the O-type stars on the MS and the B-type stars on the Zero Age Main Sequence (ZAMS). The orientations are given by North (N), East (E), South-West (SW) and so on. The caption of each image displays the following information: MSX name of the source, $\log(L/L_\odot)$, distance, Spectral type classification and structures present on the field shown as “Morphological classification” (label): ℓ_{proj} ; PA; R (if available)’ (i.e. BP1(1): 0.91 pc; 8.5; 60°). A full description of the images is presented in Figure 1.

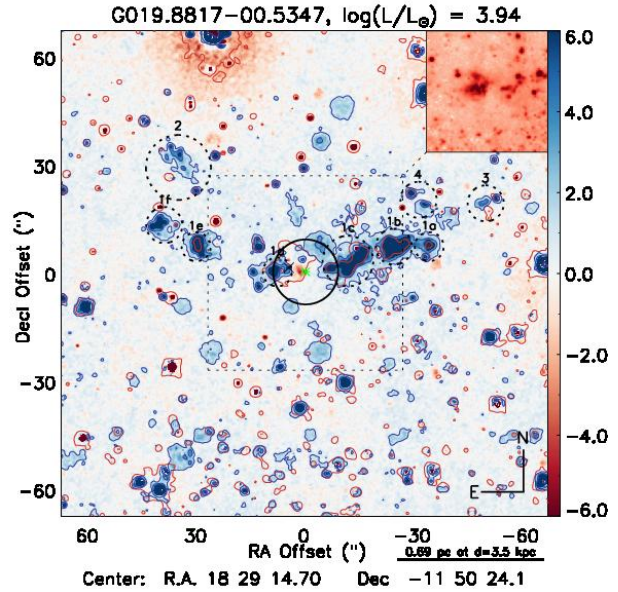


Figure A6. G019.8817-00.5347, $\log(L/L_\odot) = 3.94$, $d=3.5$ kpc, Sp. Type: B1 V₀, $H-K_s = 1.63$ mag. BP2(1a,1f): 0.68, 0.74 pc; 70° , 285° ; $R=5.5$, 5.9 ; $K(2)$: 0.84 pc; 50° ; $K(3)$: 0.68 pc; 290° ; $K(4)$: 0.96 pc; 330° .

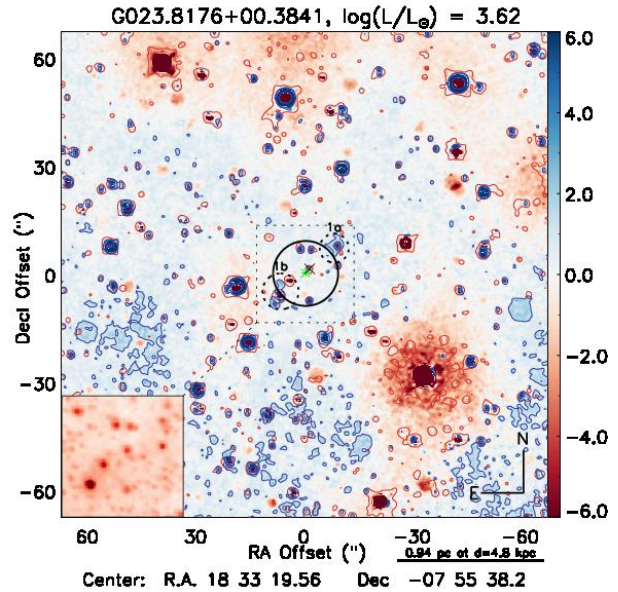


Figure A19. G023.8176+00.3841, $\log(L/L_\odot) = 3.62$, $d=4.8$ kpc, Sp. Type: B2 V₀, $H-K_s = 0.67$ mag. BP2(1a,1b): 0.28, 0.34 pc; 315° , 135° ; 1.6, 3.1.

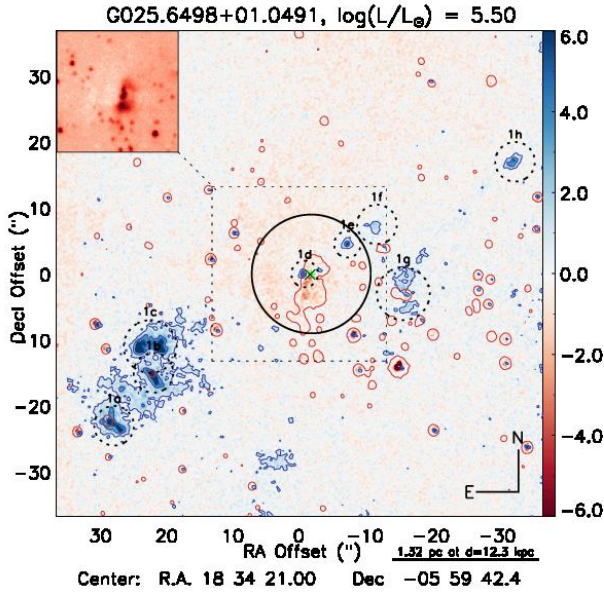


Figure A26. G025.6498+01.0491, $\log(L/L_{\odot}) = 5.50$, $d=12.3$ kpc, Sp. Type: O5.5 V, $H-K_s = 3.61$ mag. BP2(1a-1h): 2.27, 2.27 pc; 125° , 295° ; 3.8, 11.0.

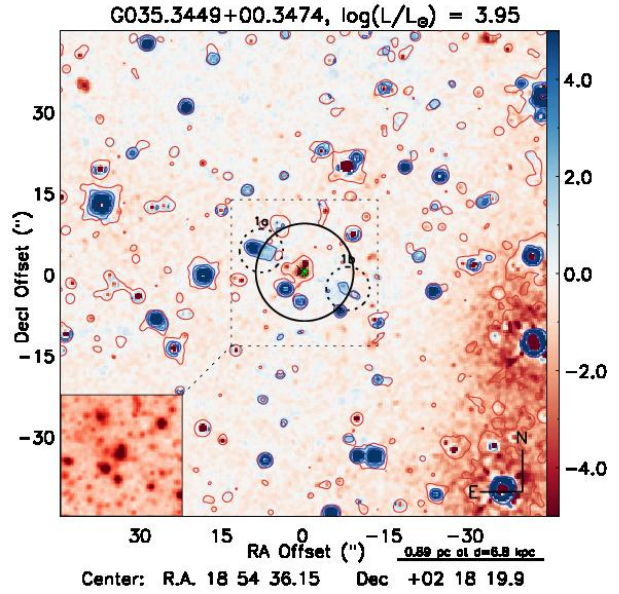


Figure A55. G035.3449+00.3474, $\log(L/L_{\odot}) = 3.95$, $d=6.8$ kpc, Sp. Type: B1 V₀, $H-K_s = 1.52$ mag. BP2(1a,1b): 0.39, 0.29 pc; 60° , 250° ; 4.5, 5.0.

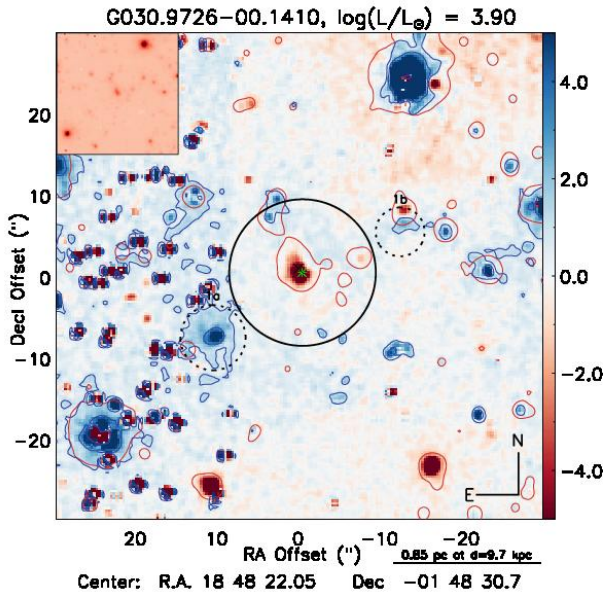


Figure A45. G030.9726-00.1410, $\log(L/L_{\odot}) = 3.90$, $d=9.7$ kpc, Sp. Type: B1 V₀, $H-K_s = 3.03$ mag. BP2(1a,1b): 0.76, 0.71 pc; 125° , 300° ; 2.1, 6.0.

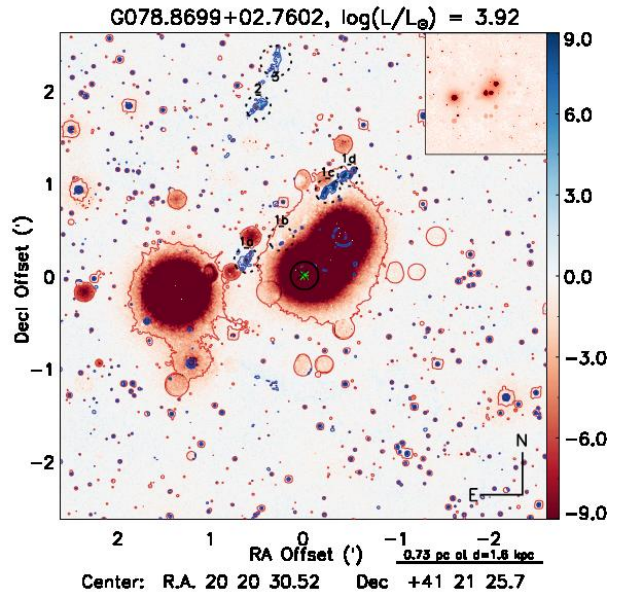


Figure A90. G078.8699+02.7602, $\log(L/L_{\odot}) = 3.92$, $d=1.6$ kpc, Sp. Type: B1 V₀, $H-K_s = 2.20$ mag. BP2(1a,1b,1c,1d): 0.78 pc; 80° , 35° , 345° , 335° ; 7.5; K(2): 0.96 pc; 5° ; K(3): 1.08 pc; 15° .

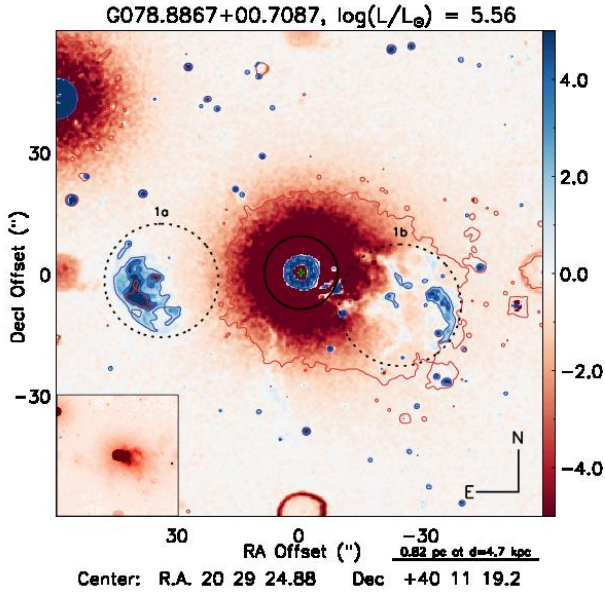


Figure A91. G078.8867+00.7087, $\log(L/L_\odot) = 5.56$, $d=4.7$ kpc, Sp. Type: O5 V, $H-K_s = 4.20$ mag. BP2(1a,1b): 1.02, 0.91 pc; 100° , 250° ; 1.8, 1.4.

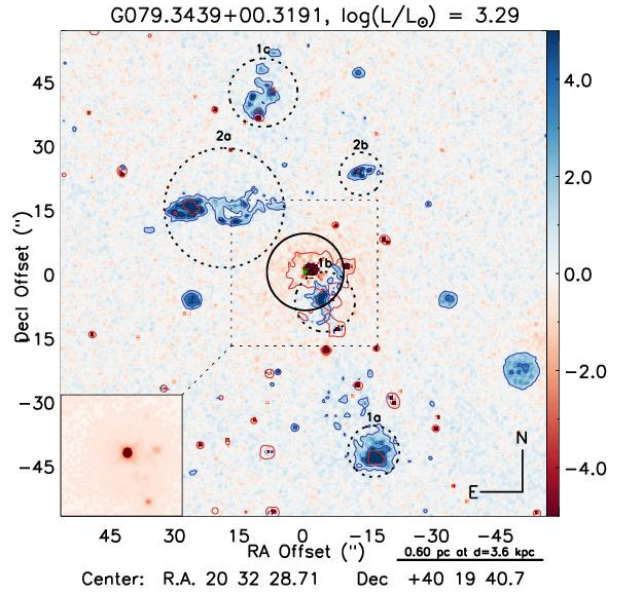


Figure A97. G079.3439+00.3191, $\log(L/L_\odot) = 3.29$, $d=0.60$ kpc, Sp. Type: B3 V₀, $H-K_s = 2.45$ mag. BP2(1a,1b): 0.85, 0.76 pc; 200° , 15° ; 4.8, 5.2.

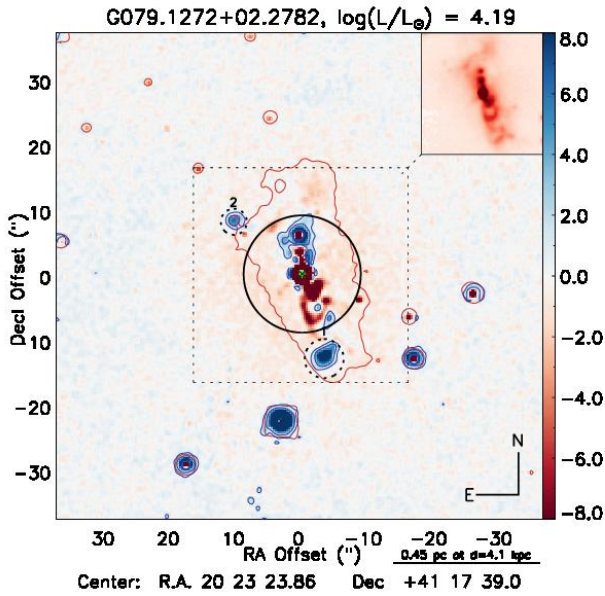


Figure A92. G079.1272+02.2782, $\log(L/L_\odot) = 4.19$, $d=4.1$ kpc, Sp. Type: B0.5 V₀, $H-K_s = 2.60$ mag. K(1): 0.28 pc; 60; BP2(2): 0.28 pc; 0° , 195° ; 3.4.

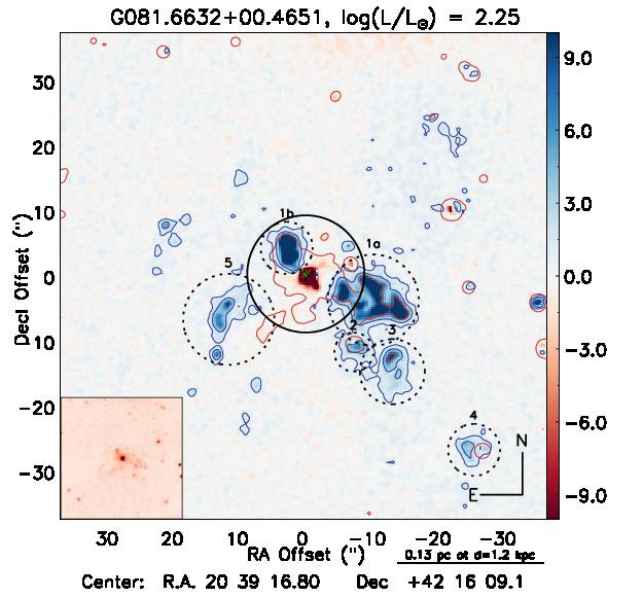


Figure A98. G081.6632+00.4651, $\log(L/L_\odot) = 2.25$, $d=1.2$ kpc, Sp. Type: <B3 V₀, $H-K_s = 3.82$ mag. BP2(1a,1b): 0.11, 0.05 pc; 250° , 30° ; 2.3, 1.5; K(2): 0.09 pc; 215° ; K(3): 0.14 pc; 225° ; K(4): 0.23 pc; 225° ; K(5): 0.10 pc; 115° .

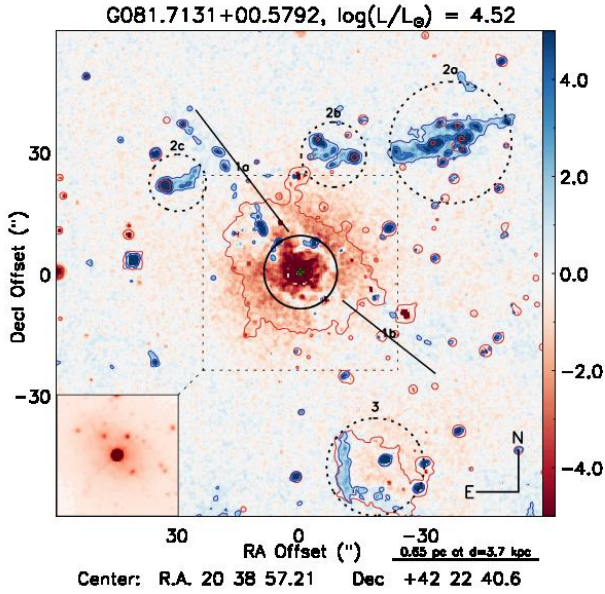


Figure A99. G081.7131+00.5792, $\log(L/L_{\odot}) = 4.52$, $d=3.7$ kpc, Sp. Type: B0 V, $H-K_s = 2.13$ mag. BP2(1a,1b): 0.90, 0.67 pc; 40° , 235° ; 11.2, 8.4; BP2(2a,2b): 0.86, 0.80 pc; 50° , 310° ; 4.5, 8.3; D(3): 1.12 pc; 195° .

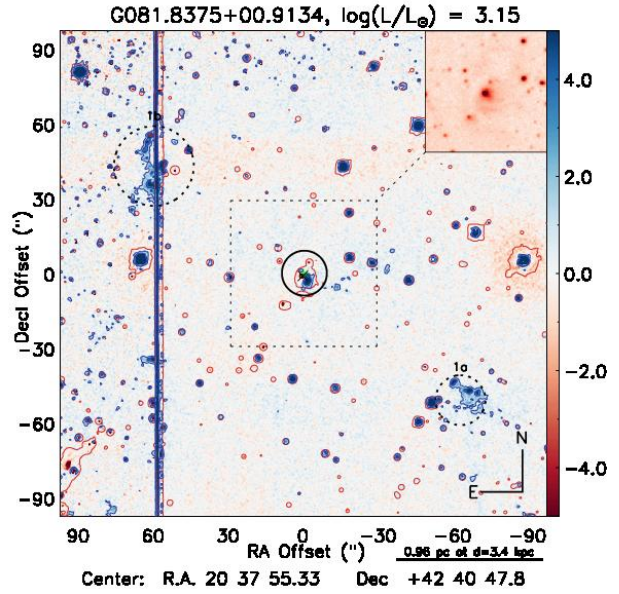


Figure A103. G081.8375+00.9134, $\log(L/L_{\odot}) = 3.15$, $d=3.4$ kpc, Sp. Type: B3 V₀, $H-K_s = 3.20$ mag. BP2(1a,1b): 1.31, 1.31 pc; 55° , 235° ; 4.0, 9.3.

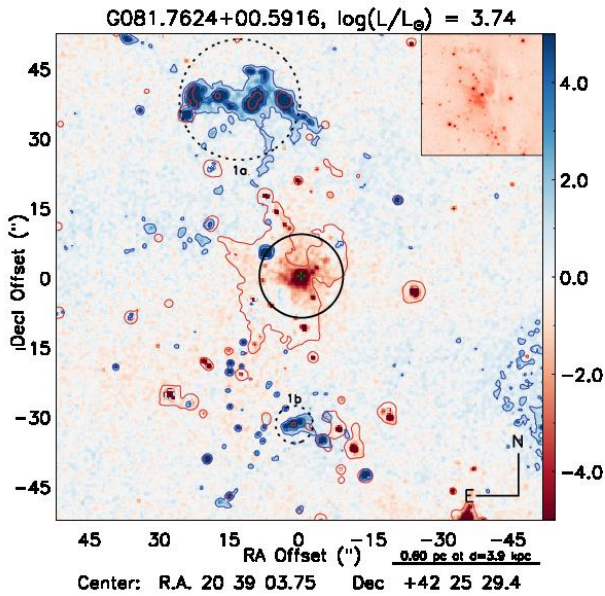


Figure A102. G081.7624+00.5916, $\log(L/L_{\odot}) = 3.74$, $d=3.9$ kpc, Sp. Type: B1 V₀, $H-K_s = 3.81$ mag. BP2(1a,1b): 0.77, 0.60 pc; 20° , 175° ; 1.8, 7.0.

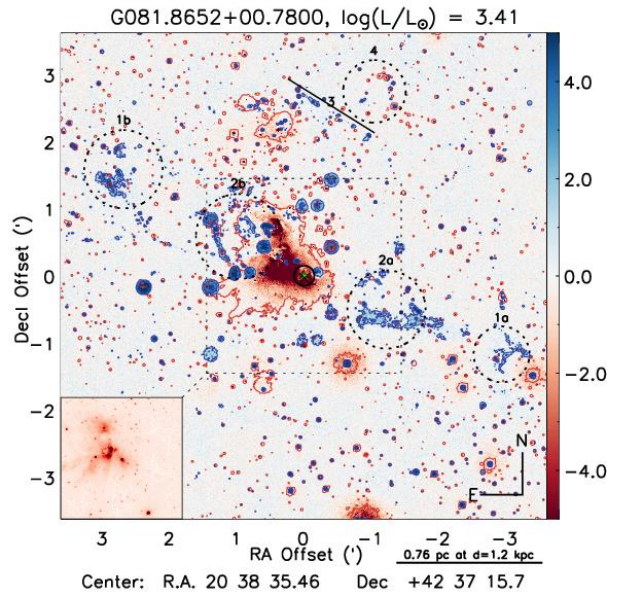


Figure A104. G081.8652+00.7800, $\log(L/L_{\odot}) = 3.41$, $d=1.2$ kpc, Sp. Type: B3 V₀, $H-K_s = 3.29$ mag. BP2(1a,1b): 1.25, 1.25 pc; 60° , 250° ; 4.6, 5.7; BP2(2a,2b): 0.60, 0.62 pc; 60° , 250° ; 2.2, 2.5; BP2(3): 0.46 pc; 350° ; 5.6; K(4): 1.14 pc; 340° .

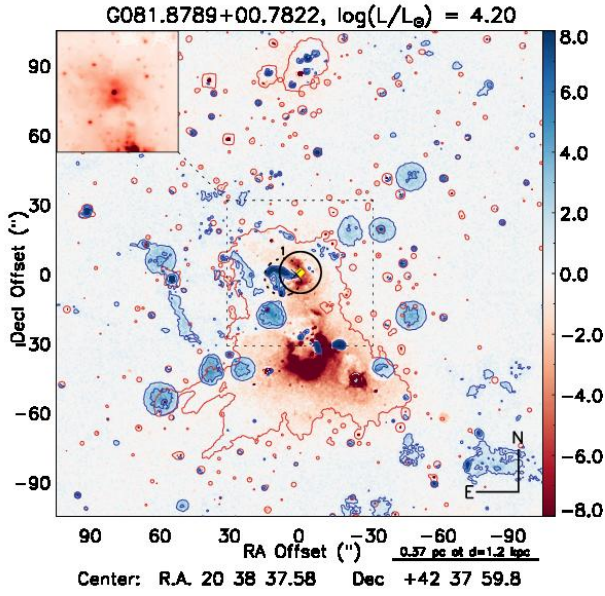


Figure A105. G081.8789+00.7822, $\log(L/L_{\odot}) = 4.20$, $d=1.2$ kpc, Sp. Type: B0.5 V₀, $H-K_s = 1.39$ mag. BP1(1): 0.09 pc; 105°; 6.0.

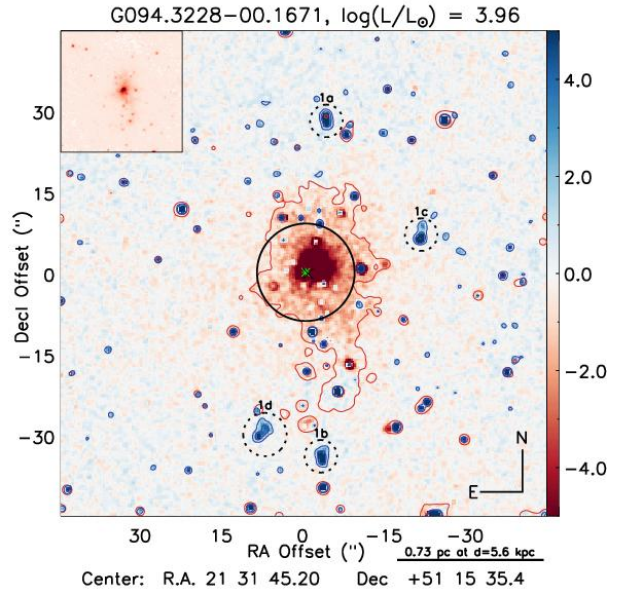


Figure A112. G094.3228-00.1671, $\log(L/L_{\odot}) = 3.96$, $d=5.6$ kpc, Sp. Type: B1 V₀, $H-K_s = 2.22$ mag. BP4(1a,1b,1c,1d): 0.75, 1.00, 0.58, 0.94 pc; 355°, 185°, 290°, 165°; 16.0, 15.0, 6.8, 11.0.

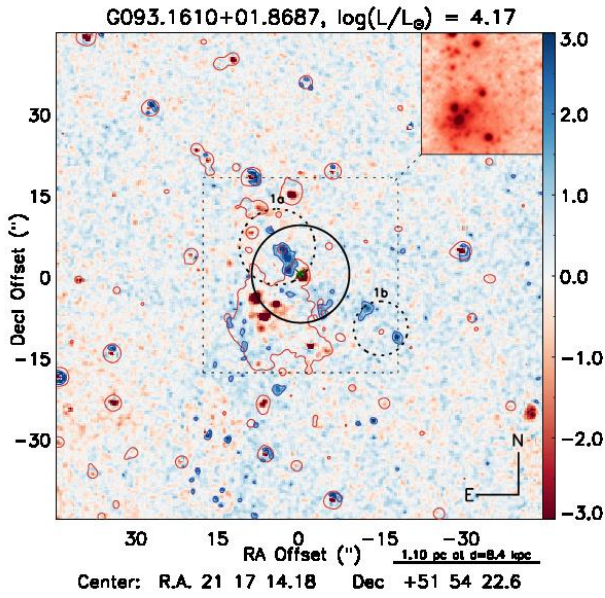


Figure A111. G093.1610+01.8687, $\log(L/L_{\odot}) = 4.17$, $d=8.4$ kpc, Sp. Type: B0.5 V₀, $H-K_s = 0.73$ mag. BP2(1a,1b): 0.45, 0.84 pc; 45°, 240°; 3.5, 7.4.

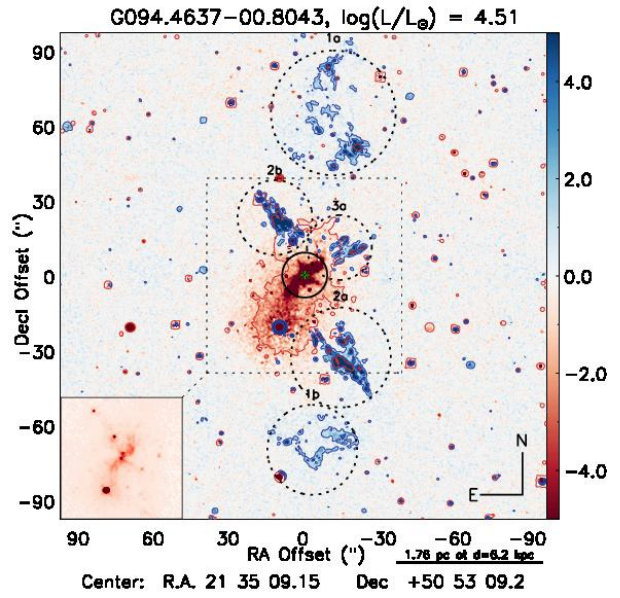


Figure A113. G094.4637-00.8043, $\log(L/L_{\odot}) = 4.51$, $d=6.2$ kpc, Sp. Type: B0 V₀, $H-K_s = 2.90$ mag. BP5(1a,1b): 2.70, 2.38 pc; 355°, 180°; 3.5, 3.3; BP5(2a,2b): 1.66, 1.24 pc; 210°, 30°; 3.2, 3.0; BP5(3a): 0.78 pc; 300°; 2.5.

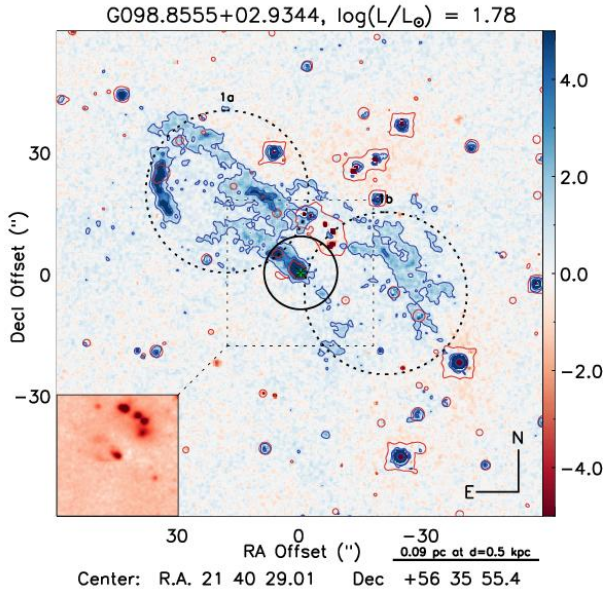


Figure A119. G098.8555+02.9344, $\log(L/L_{\odot}) = 1.78$, $d=0.5$ kpc, Sp. Type: $<B3 V_0$, $H-K_s = 1.51$ mag. BP2(1a,1b): 0.12, 0.10 pc; 45° , 260° ; 3.3, -.

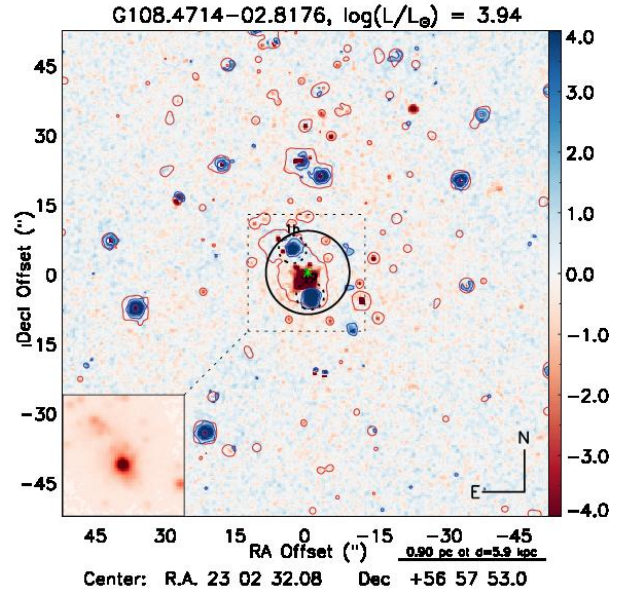


Figure A125. G108.4714-02.8176, $\log(L/L_{\odot}) = 3.94$, $d=5.9$ kpc, Sp. Type: $B1 V_0$, $H-K_s = 2.16$ mag. BP2(1a,1b): 0.19, 0.26 pc; 20° , 195° ; 2.0, 4.5.

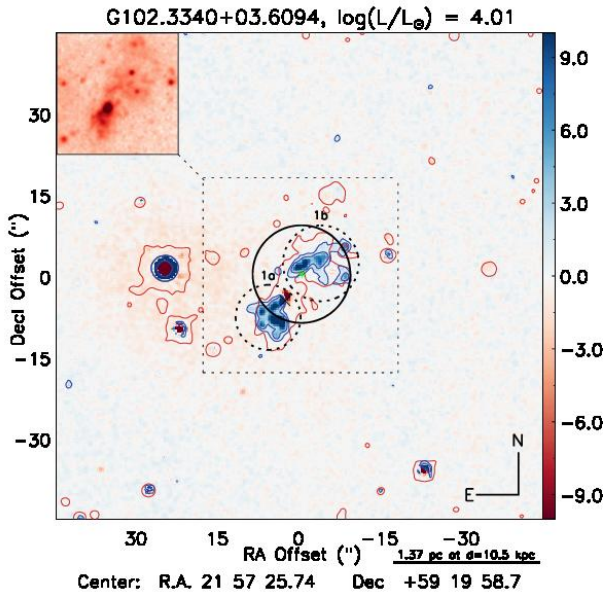


Figure A122. G102.3340+03.6094, $\log(L/L_{\odot}) = 4.01$, $d=10.5$ kpc, Sp. Type: $B1 V_0$, $H-K_s = 1.51$ mag. BP2(1a,1b): 0.44, 0.73 pc; 135° , 315° ; 0.9, 2.0.

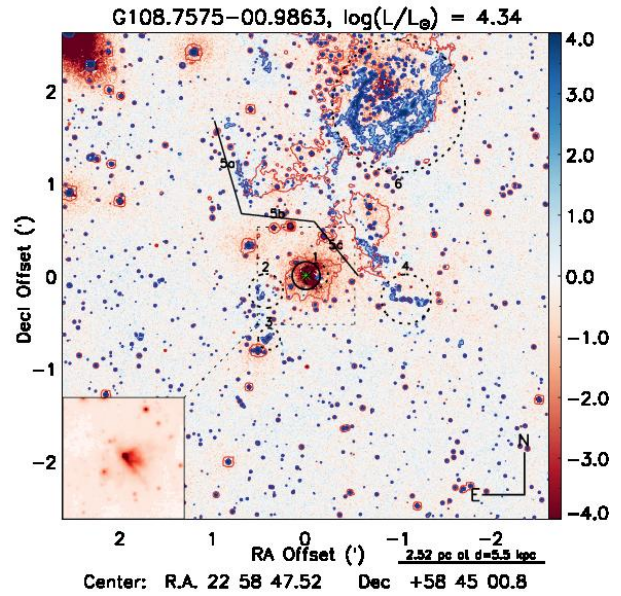


Figure A126. G108.7575-00.9863, $\log(L/L_{\odot}) = 4.35$, $d=5.5$ kpc, Sp. Type: $B0.5 V_0$, $H-K_s = 5.05$ mag. BP1(1): 0.32 pc; 270° ; 1.1; K(2): 0.98 pc; 110° ; K(3): 1.30 pc; 150° ; BP1(4): 0.70 pc; 255° ; 5.7; D(5a,5b,5c): 4.10 pc; $275^{\circ} < \theta < 30^{\circ}$; D(6): 2.40 pc; 50° , 240° .

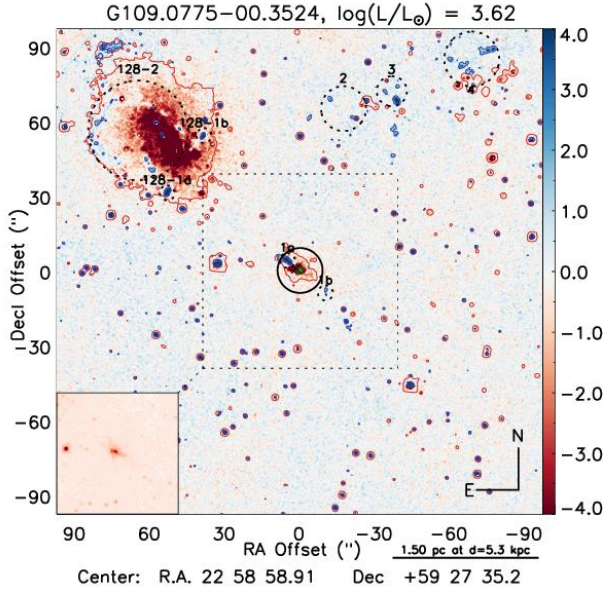


Figure A127. G109.0775-00.3524, $\log(L/L_\odot) = 3.62$, $d=5.3$ kpc, Sp. Type: B2 V₀, H-K_s = 3.01 mag. BP2(1a,1b): 0.22, 0.35 pc; 60°, 230°; 3.5, 7.0; BP2(128-1a,128-1b): -, 40°, 60°; 5.2, 7.8; D(128-2): -, 50°; K(2): 1.80 pc; 345°; K(3): 2.10 pc; 335°; K(4): 2.81 pc; 320°.

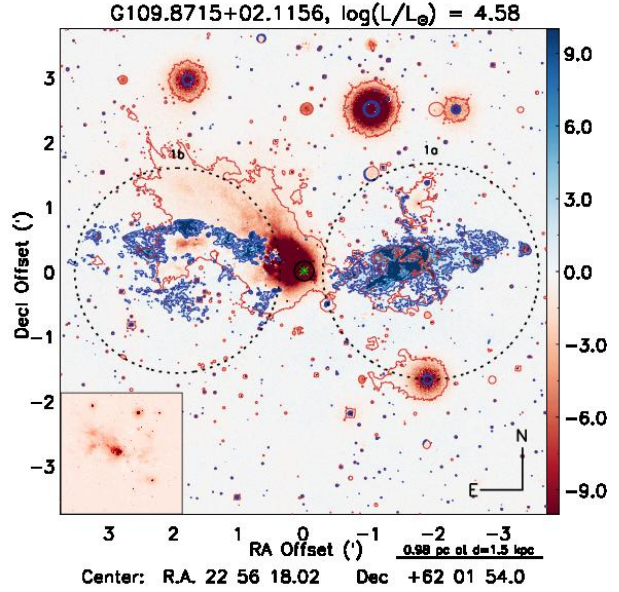


Figure A129. G109.8715+02.1156, $\log(L/L_\odot) = 4.58$, $d=1.5$ kpc, Sp. Type: B0 V₀, H-K_s = 2.44 mag. BP2(1a,1b): 1.64, 1.61 pc; 75°, 275°; 4.8, 5.0.

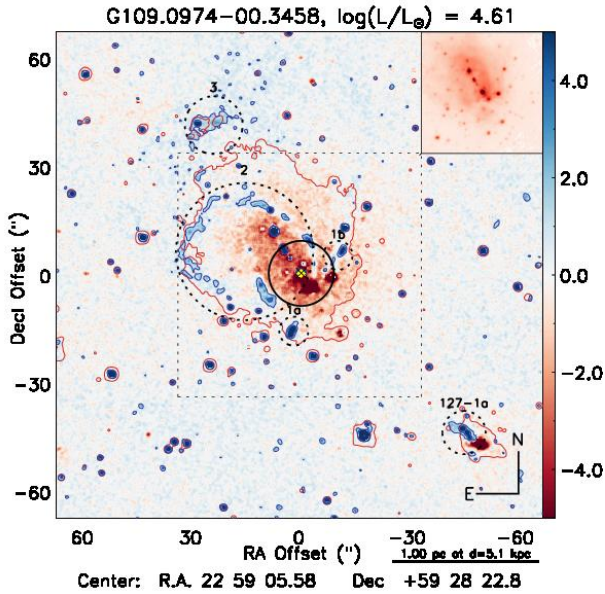


Figure A128. G109.0974-00.3458, $\log(L/L_\odot) = 4.61$, $d=5.1$ kpc, Sp. Type: B0 V₀, H-K_s = 1.07 mag. BP2(1a,1b): 0.39, 0.39 pc; 150°, 320°; 5.2, 7.8; D(2): 0.93 pc; 55°; K(3): 1.25 pc; 35°.

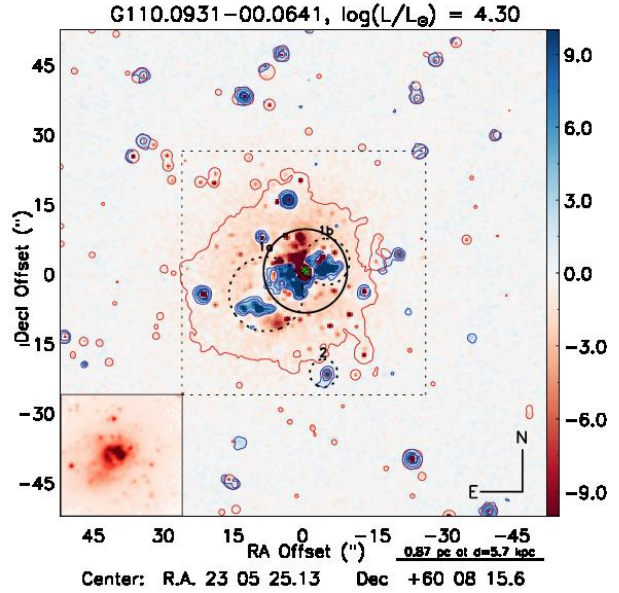


Figure A130. G110.0931-00.0641, $\log(L/L_\odot) = 4.30$, $d=5.7$ kpc, Sp. Type: B0.5 V₀, H-K_s = 1.60 mag. BP2(1a,1b): 0.43, 0.59 pc; 125°, 275°; 1.6, 3.6; K(2): 0.64 pc; 195°.

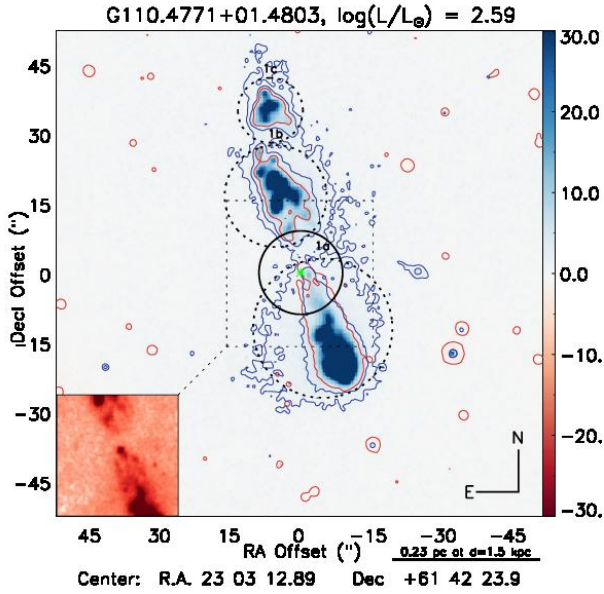


Figure A132. G110.4771+01.4803, $\log(L/L_{\odot}) = 2.59$, $d=1.5$ kpc, Sp. Type: B3 V₀. BP2(1a,1b,1c): 0.20, 0.30 pc; 15°, 205°; 3.1, 4.1.

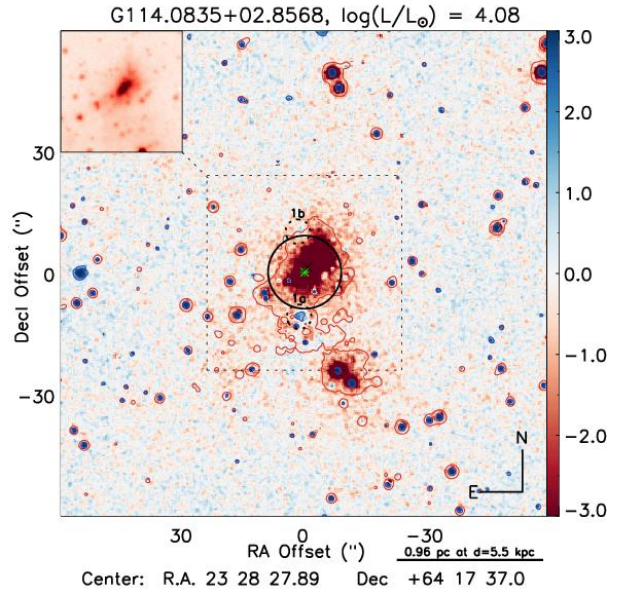


Figure A139. G114.0835+02.8568, $\log(L/L_{\odot}) = 4.08$, $d=5.5$ kpc, Sp. Type: B0.5 V₀, H-K_s = 3.00 mag. BP2(1a,1b): 0.35, 0.26 pc; 160°, 15°; 4.8, 7.5.

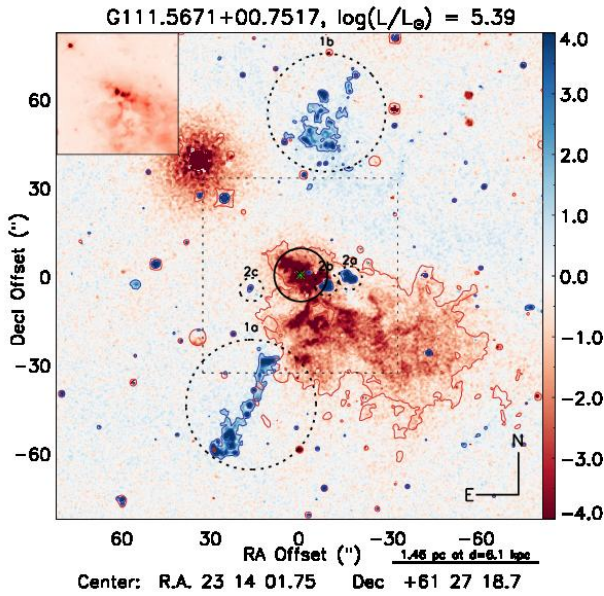


Figure A136. G111.5671+00.7517, $\log(L/L_{\odot}) = 5.39$, $d=6.1$ kpc, Sp. Type: O6 V, H-K_s = 3.76 mag. BP4(1a,1b): 2.06, 2.35 pc; 155°, 350°; 7.2, 5.6; BP4(2a,2b,2c): 0.56, 0.56 pc; 95°, 270°; 4.8, 6.7.

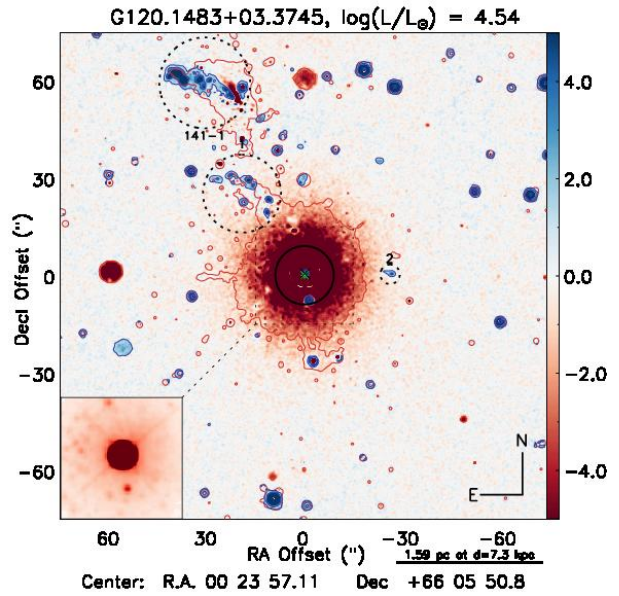


Figure A140. G120.1483+03.3745, $\log(L/L_{\odot}) = 4.54$, $d=7.3$ kpc, Sp. Type: B0 V₀, H-K_s = 2.02 mag. BP1(1): 1.40 pc; 65°; 6.5; K(2): 0.94 pc; 270°. BP1(141-1): -; 30°; 4.6.

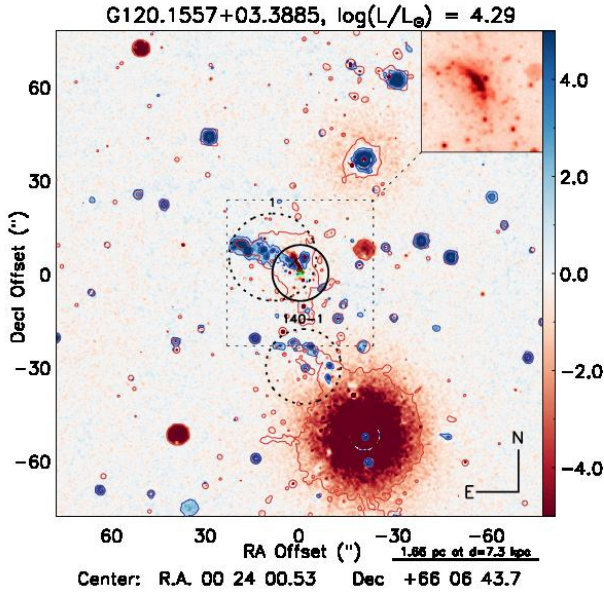


Figure A141. G120.1557+03.3885, $\log(L/L_{\odot}) = 4.29$, $d=7.3$ kpc, Sp. Type: B0.5 V₀, H-K_s = 2.27 mag. BP1(1): 0.89 pc; 65°; 4.6. BP1(140-1): -; 185°; 6.5.

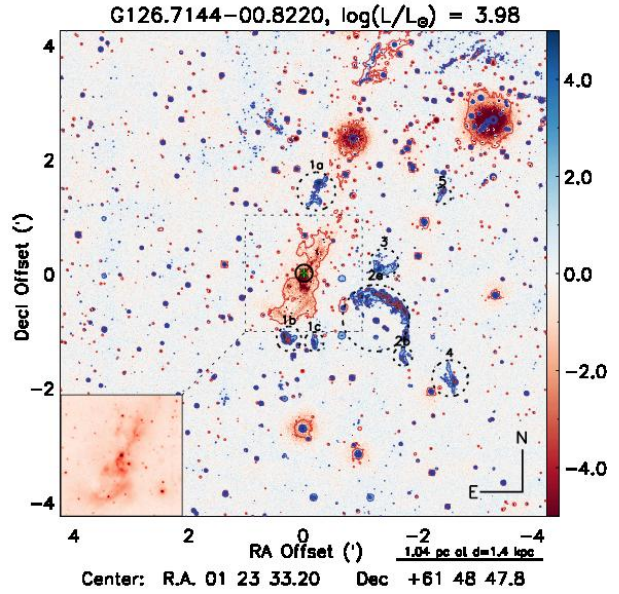


Figure A145. G126.7144-00.8220, $\log(L/L_{\odot}) = 3.98$, $d=1.4$ kpc, Sp. Type: B1 V₀, H-K_s = 4.08 mag. BP2(1a,1b,1c): 0.70, 0.52, 0.52 pc; 350°, 160°, 185°; 6.5, 4.9, 5.6; BP2(2a,2b): 0.52, 0.15 pc; 245°, 230°; K(3): 0.57 pc; 280°; K(4): 1.35 pc; 235°; K(5): 1.13 pc; 305°.

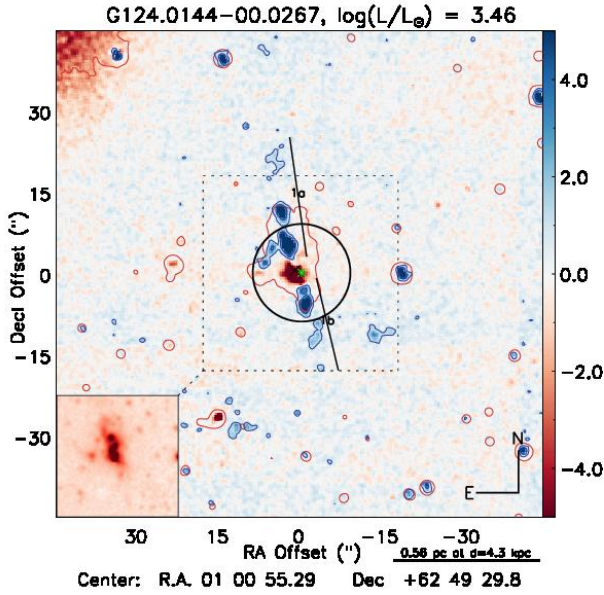


Figure A142. G124.0144-00.0267, $\log(L/L_{\odot}) = 3.46$, $d=4.3$ kpc, Sp. Type: B2 V₀, H-K_s = 1.38 mag. BP2(1a,1b): 0.48, 0.38 pc; 10°, 200°; 8.0, 6.3.

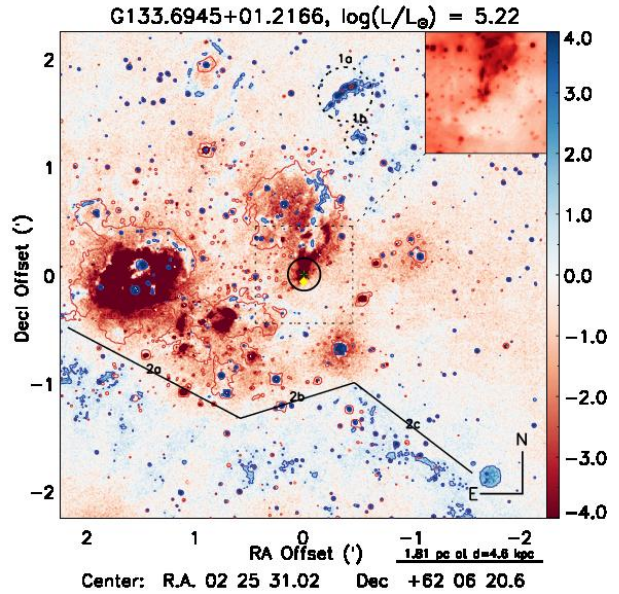


Figure A146. G133.6945+01.2166, $\log(L/L_{\odot}) = 5.22$, $d=4.6$ kpc, Sp. Type: O6.5 V, H-K_s = 3.38 mag. BP1(1a,1b): 2.51, 2.01 pc; 350°, 340°; 6.3, 8.0; D(2a,2b,2c): 5.24 pc; 100-225°.

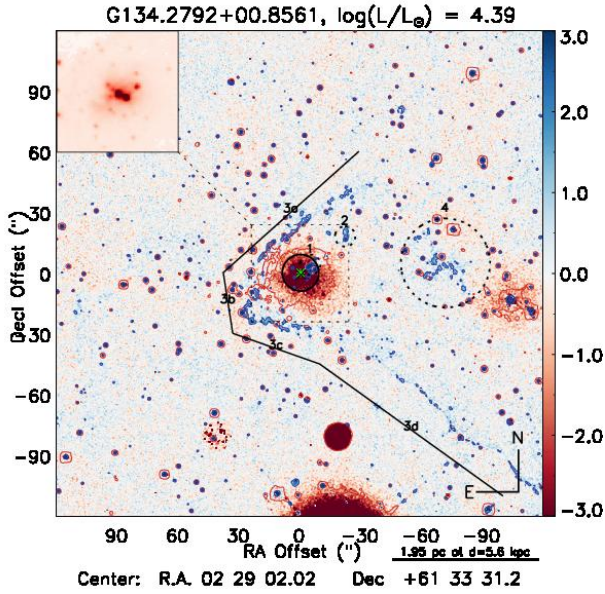


Figure A149. G134.2792+00.8561, $\log(L/L_{\odot}) = 4.39$, $d=5.6$ kpc, Sp. Type: B0.5 V₀, $H-K_s = 1.85$ mag. BP1(1): 0.38 pc; 310°; 2.0; K(2): 0.92 pc; 320°. D(3a,3b,3c,3d): 4.88 pc; 320°. D(2): 1.90 pc; 275°.

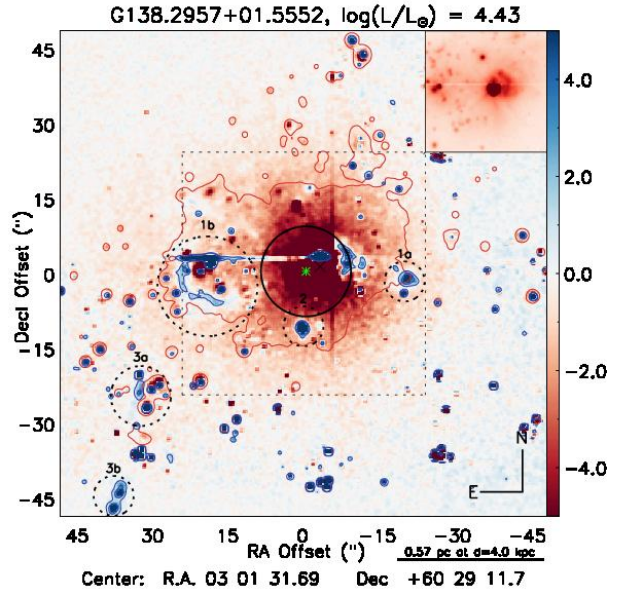


Figure A153. G138.2957+01.5552, $\log(L/L_{\odot}) = 4.43$, $d=4.0$ kpc, Sp. Type: B0 V, $H-K_s = 2.66$ mag. BP2(1a,1b): 0.24, 0.24 pc; 270°, 90°; 1.7, 1.3; K(2): 0.28 pc; 180°; BP1(3a,3b): 0.28, 0.28 pc; 125°, 140°; 7.0, 7.0.

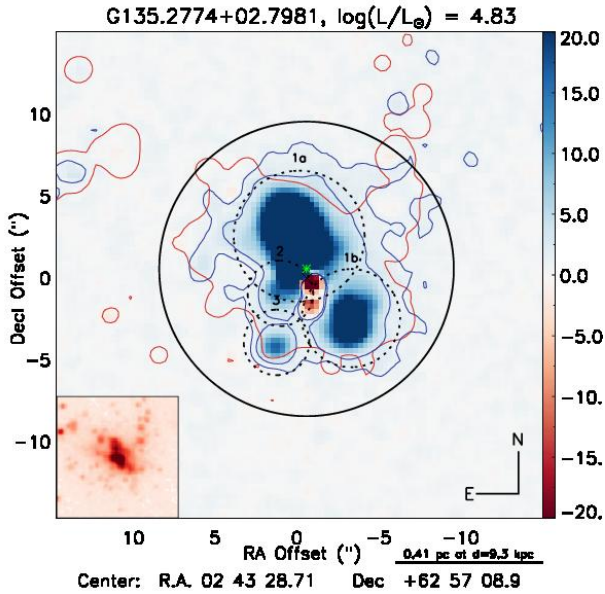


Figure A150. G135.2774+02.7981, $\log(L/L_{\odot}) = 4.83$, $d=9.3$ kpc, Sp. Type: O8.5 V, $H-K_s = 1.64$ mag. BP2(1a,1b): 0.34, 0.20 pc; 15°, 240°; 1.7, 1.1; K(2): 0.17 pc; 135°.

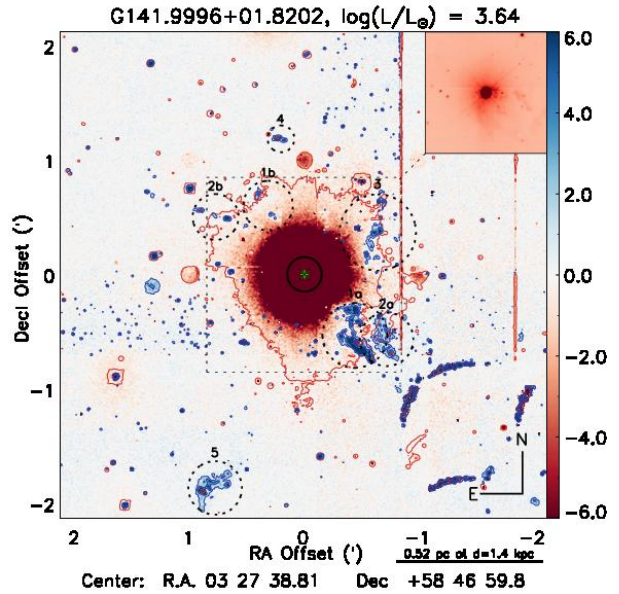


Figure A155. G141.9996+01.8202, $\log(L/L_{\odot}) = 3.64$, $d=1.4$ kpc, Sp. Type: B2 V₀, $H-K_s = 1.93$ mag. BP4(1a,1b): 0.35, 0.35 pc; 230°, 30°; 2.9, 2.8; BP4(2a,2b): 0.46, 0.43 pc; 235°, 60°; 4.0, 6.8; K(3): 0.38 pc; 300°; K(4): 0.49 pc; 15°; K(5): 0.31 pc; 155°.

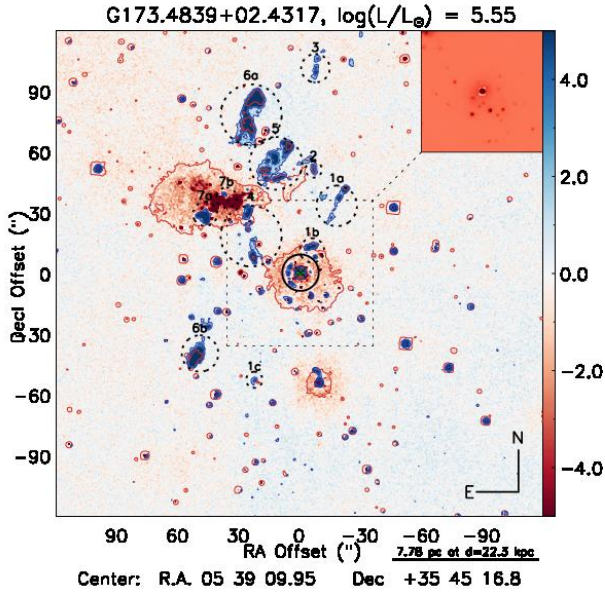


Figure A162. G173.4839+02.4317, $\log(L/L_\odot) = 5.55$, $d=22.3$ kpc, Sp. Type: O5 V, $H-K_s = 1.38$ mag. BP8(1a,1b,1c): 5.36, 6.38 pc; 330° , 150° ; 13.7, 26.0; BP8(4): -, 50° ; BP8(6a,6b): -, 20° , 125° ; BP8(7a,7b): -, 60° , 50° ; K(2): 5.99 pc; 355° ; K(3): 11.60 pc; 355° ; K(5): -, 15° .

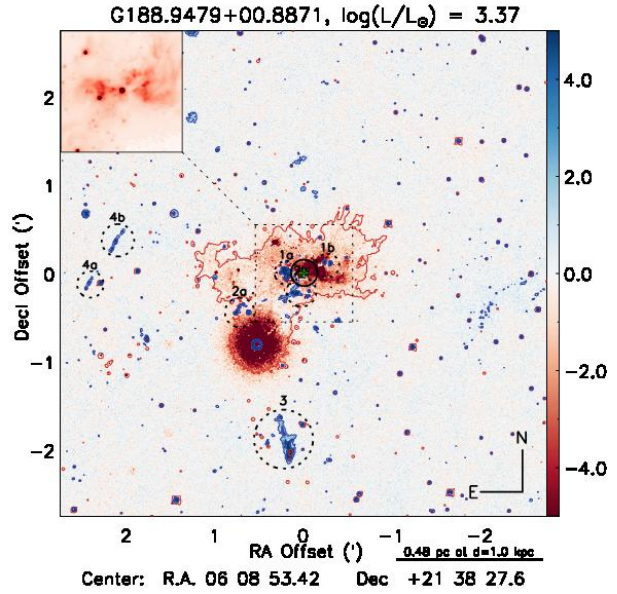


Figure A167. G188.9479+00.8871, $\log(L/L_\odot) = 3.37$, $d=1.0$ kpc, Sp. Type: B3 V₀, $H-K_s = 2.42$ mag. BP4(1a,1b): 0.10, 0.10 pc; 105° , 285° ; 3.0, 4.5; BP4(2a,2b): 0.12, 0.12 pc; 120° , 135° ; 3.8, 3.8; BP1(3): 0.48 pc; 165° ; 8.2; BP2(4a,4b): 0.13, 0.13 pc; 85° ; 12.5, 12.5.

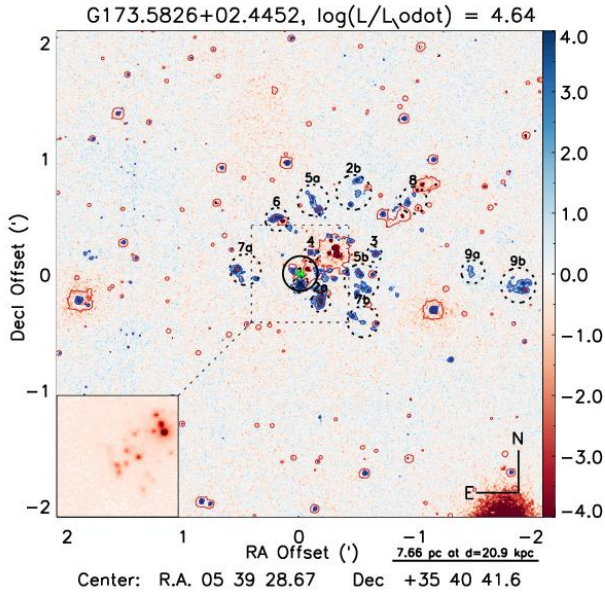


Figure A163. G173.5826+02.4452, $\log(L/L_\odot) = 4.64$, $d=20.9$ kpc, Sp. Type: O9.5 V, $H-K_s = 1.76$ mag. K(1): 0.72 pc; 180° ; BP6(2a,2b): 7.16 pc; 210° , 330° ; 4.8; BP6(5a,5b): 6.28 pc; 0° , 265° ; 5.0; BP6(7a,7b): 8.16 pc; 90° , 135° ; 5.4; K(3): 3.89 pc; 285° ; K(4): 0.88 pc; 345° ; K(6): 3.39 pc; 30° ; K(9a): 7.66 pc; 270° ; K(9b): 10.17 pc; 270° .

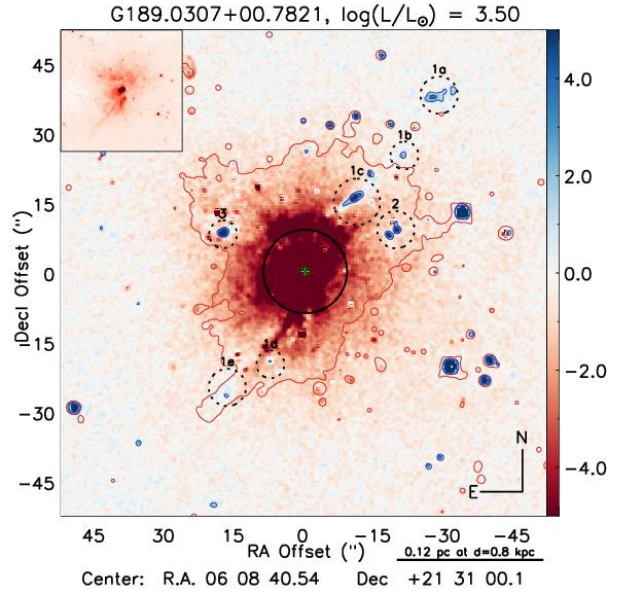


Figure A168. G189.0307+00.7821, $\log(L/L_\odot) = 3.50$, $d=0.8$ kpc, Sp. Type: B2 V₀, $H-K_s = 4.06$ mag. BP2(1a-1e): 0.18, 0.11 pc; 320° , 140° ; 9.0, 5.0.

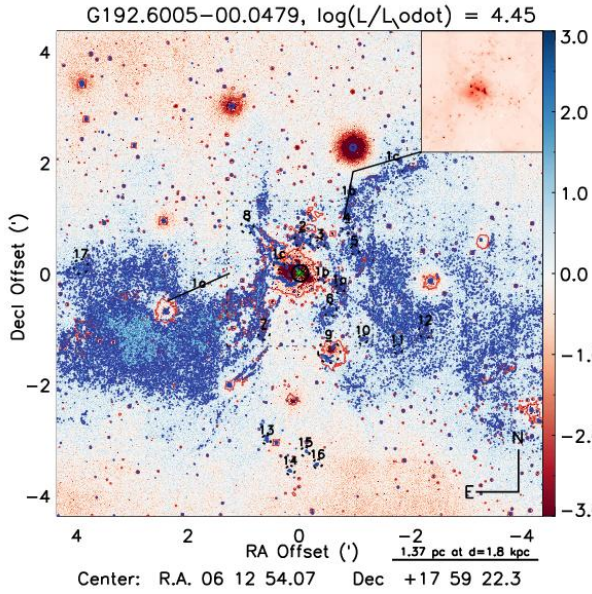


Figure A171. G192.6005-00.0479, $\log(L/L_{\odot}) = 4.45$, $d=1.8$ kpc, Sp. Type: B0 V, $H-K_s = 2.63$ mag. BP2(1a,1b,1c): 0.49, 0.23 pc; 245°, 70°; 11.3, 8.0; K(2-12); D(13a,13b,13c): 3.15 pc.

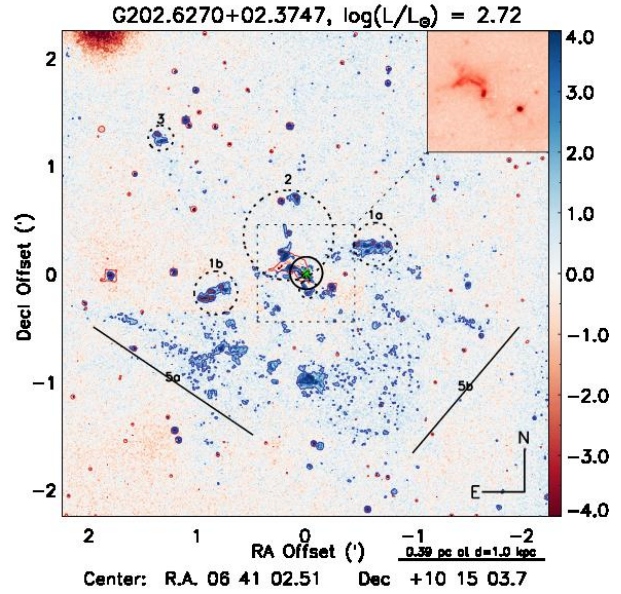


Figure A179. G202.6270+02.3747, $\log(L/L_{\odot}) = 2.72$, $d=1.0$ kpc, Sp. Type: <B3 V₀, $H-K_s = 2.94$ mag. BP3(1a,1b): 0.24, 0.30 pc; 105°, 285°; 5.3, 7.4; BP3(2): 0.22 pc; 10°; 6.3; K(3): 0.56 pc; 50°; K(4): 0.04 pc; 185°; D(5a,5b): 1.00 pc; 100-260°.

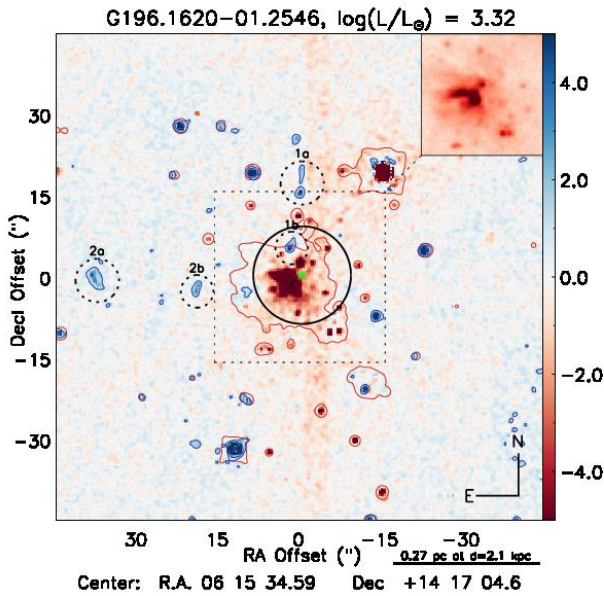


Figure A176. G196.1620-01.2546, $\log(L/L_{\odot}) = 3.32$, $d=2.1$ kpc, Sp. Type: B0 V₀, $H-K_s = 2.09$ mag. BP2(1a,1b): 0.24 pc; 0°, 16.6; BP2(2a,2b): 0.38 pc; 90°, 270°; 8.0.

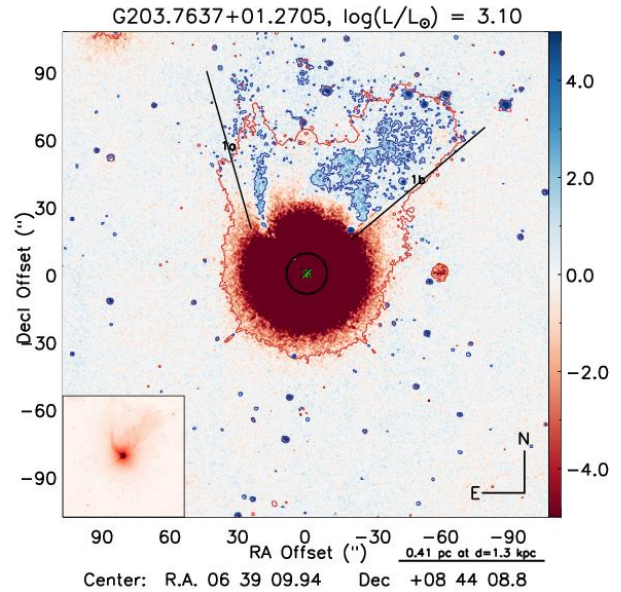


Figure A181. G203.7637+01.2705, $\log(L/L_{\odot}) = 3.10$, $d=1.3$ kpc, Sp. Type: B3 V₀, $H-K_s = 1.64$ mag. BP1(1a,1b): 0.59 pc; < 30°, > 310°; 0.8.

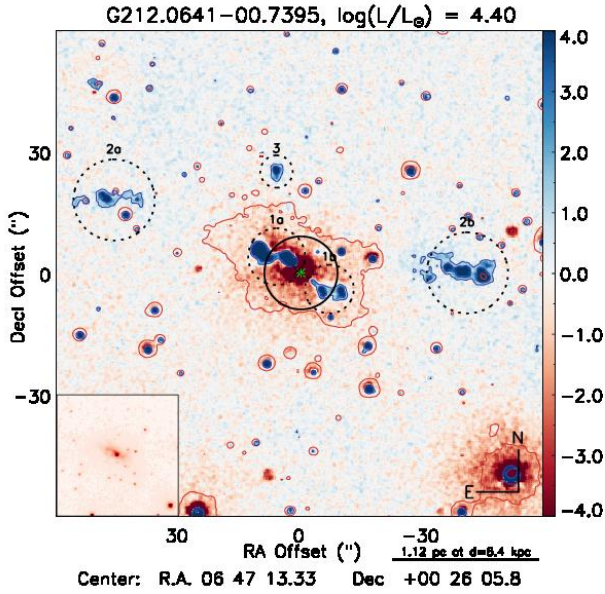


Figure A183. G212.0641-00.7395, $\log(L/L_\odot) = 4.40$, $d=6.4$ kpc, Sp. Type: B0 V, $H-K_s = 2.00$ mag. BP4(1a,1b): 0.43, 0.36 pc; 60° , 240° ; 2.2, 2.2; BP4(2a,2b): 1.75, 1.52 pc; 65° , 270° ; 7.6, 7.7; K(3): 0.89 pc; 15° .

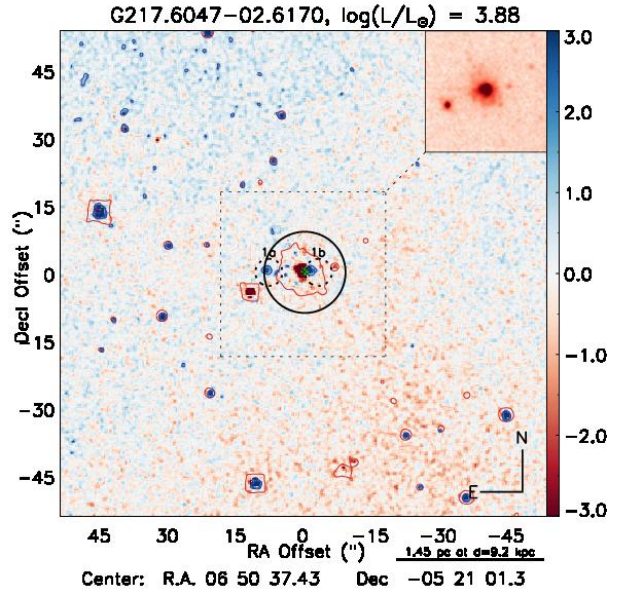


Figure A189. G217.6047-02.6170, $\log(L/L_\odot) = 3.88$, $d=9.2$ kpc, Sp. Type: B1 V₀, $H-K_s = 1.93$ mag. BP2(1a,1b): 0.38, 0.18 pc; 90° , 270° ; 4.0, 2.0.

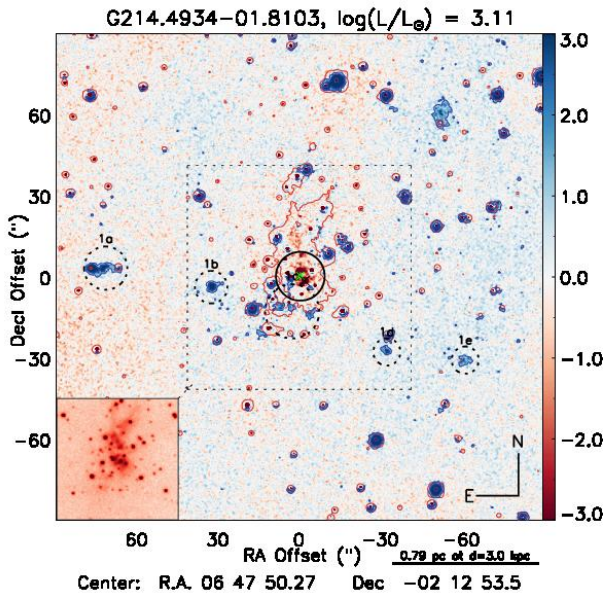


Figure A187. G214.4934-01.8103, $\log(L/L_\odot) = 3.11$, $d=3.0$ kpc, Sp. Type: B3 V₀, $H-K_s = 0.66$ mag. BP2(1a-1e): 1.16, 0.98 pc; 90° , 240° ; 16.7, 14.0.

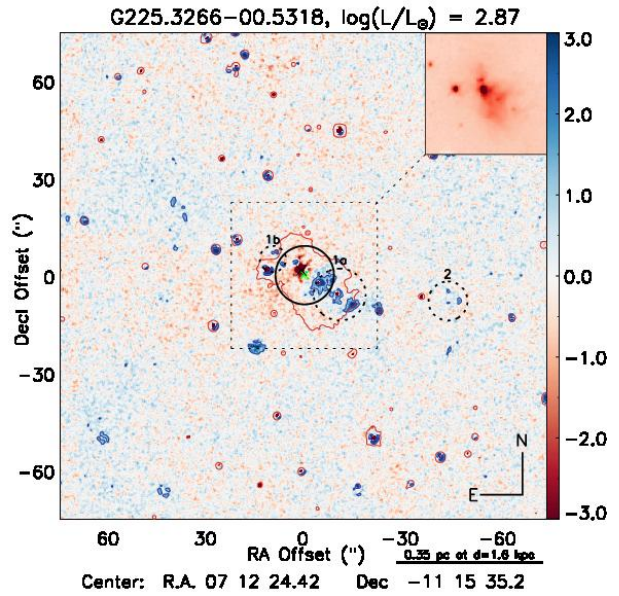


Figure A193. G225.3266-00.5318, $\log(L/L_\odot) = 2.87$, $d=1.6$ kpc, Sp. Type: <B3 V₀, $H-K_s = 2.44$ mag. BP2(1a,1b): 0.16, 0.09 pc; 230° , 50° ; 2.8, 2.5; K(2): 0.38 pc; 260° .

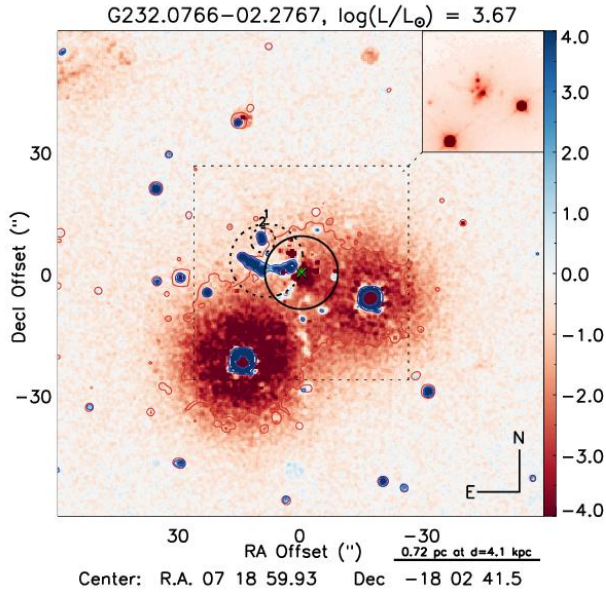


Figure A196. G232.0766-02.2767, $\log(L/L_{\odot}) = 3.67$, $d=4.1$ kpc, Sp. Type: B2 V₀, H-K_s = 1.66 mag. BP1(1): 0.36 pc; 85°; 6.0; K(2): 0.30 pc; 50°.

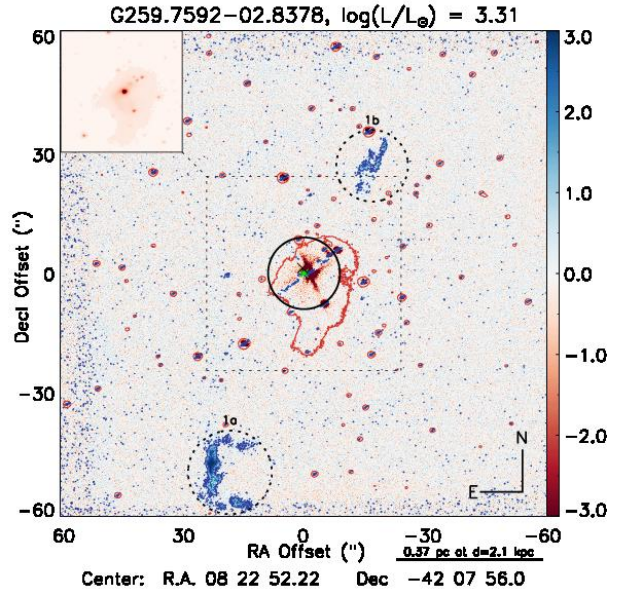


Figure A206. G259.7592-02.8378, $\log(L/L_{\odot}) = 3.31$, $d=2.1$ kpc, Sp. Type: B3 V₀, H-K_s = 3.04 mag. BP2(1a,1b): 0.64, 0.42 pc; 160°, 330°; 3.9, 7.0.

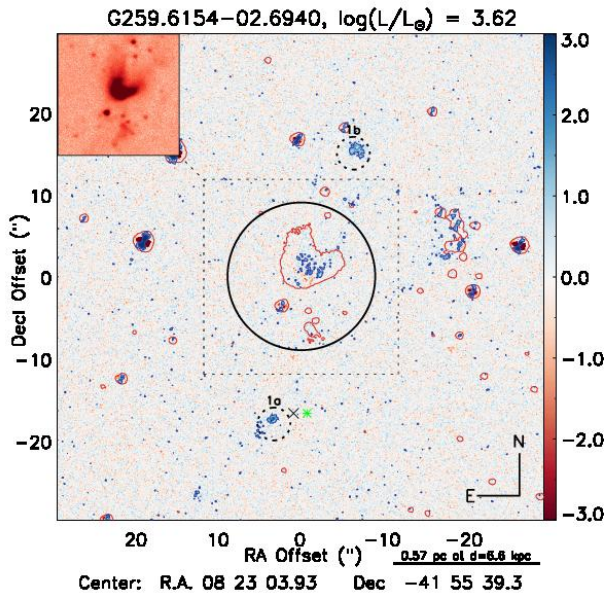


Figure A204. G259.6154-02.6940, $\log(L/L_{\odot}) = 3.62$, $d=6.6$ kpc, Sp. Type: B2 V₀, H-K_s = 1.58 mag. BP2(1a,1b): 0.6, 0.57 pc; 170°, 340°; 15.0, 8.0.

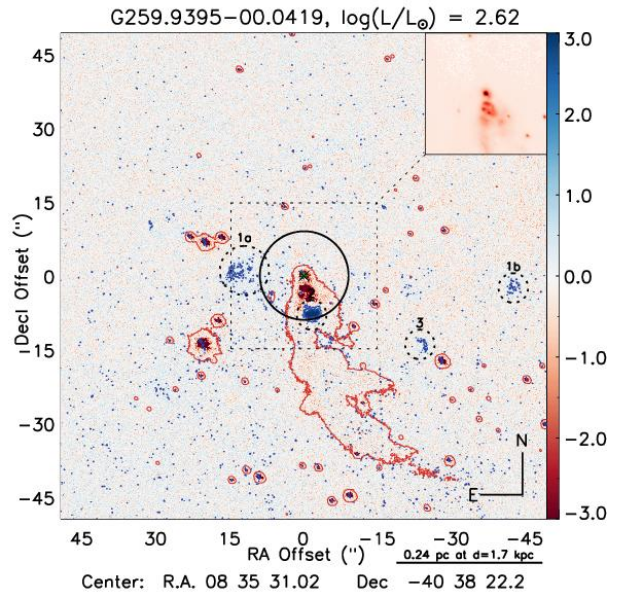


Figure A207. G259.9395-00.0419, $\log(L/L_{\odot}) = 2.62$, $d=1.7$ kpc, Sp. Type: <B3 V₀, H-K_s = 1.79 mag. BP2(1a,1b): 0.16, 0.23 pc; 90°, 240°; 3.0, 6.3; K(2): 0.07 pc; 200°; K(3): 0.23 pc; 240°.

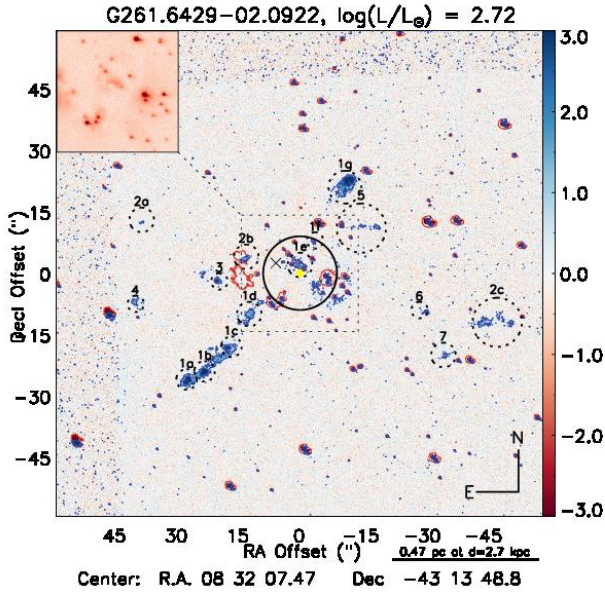


Figure A209. G261.6429-02.0922, $\log(L/L_{\odot}) = 2.72$, $d=2.7$ kpc, Sp. Type: $<B3 V_0$, $H-K_s = 0.91$ mag. BP4(1a-1g): 0.50, 0.34 pc; 135° , 330° ; 15.0, 6.7; BP4(2a-2c): 0.52, 0.72 pc; 75° , 255° ; 11.0, 8.0; K(3): 0.26 pc; 90° ; K(4): 0.56 pc; 100° ; K(5): 0.30 pc; 320° ; K(6): 0.43 pc; 255° ; K(7): 0.52 pc; 240° .

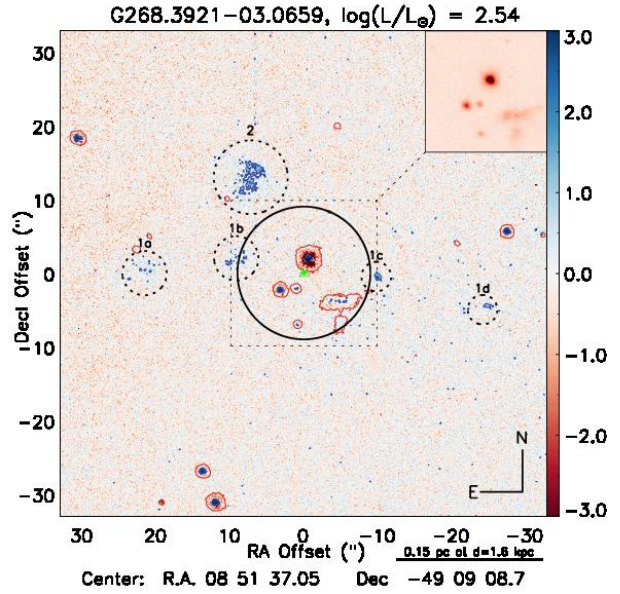


Figure A220. G268.3921-03.0659, $\log(L/L_{\odot}) = 2.54$, $d=1.6$ kpc, Sp. Type: $<B3 V_0$, $H-K_s = 0.71$ mag. BP2(1a,b,c,d): 0.18, 0.18 pc; K(2): 0.12 pc.

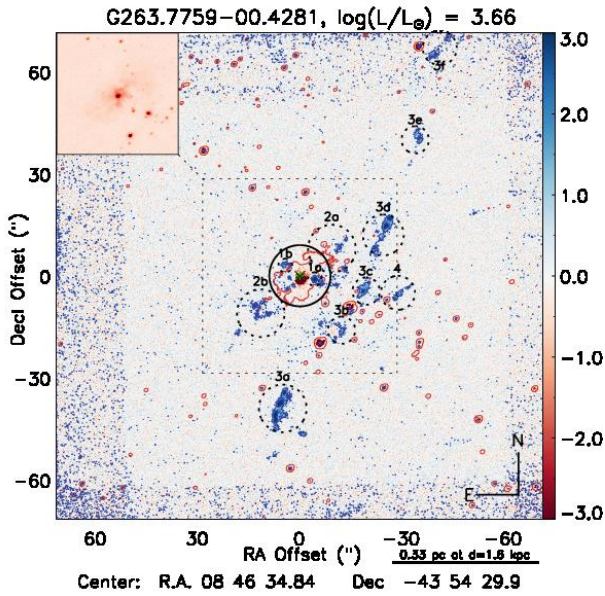


Figure A212. G263.7759-00.4281, $\log(L/L_{\odot}) = 3.66$, $d=1.6$ kpc, Sp. Type: $B2 V_0$, $H-K_s = 3.24$ mag. BP4(1a,b): 0.04, 0.05 pc; 65° , 245° ; BP4(2a,b): 0.30 pc; 315° , 130° ; BP2(3a-f): 0.38, 0.58 pc; 170° , 230° , 260° , 265° , 320° , 330° ; 7.5, 11.8.

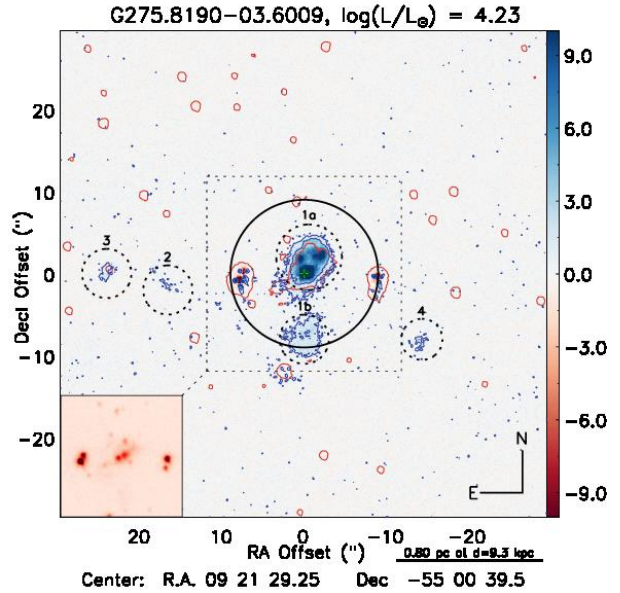


Figure A228. G275.8190-03.6009, $\log(L/L_{\odot}) = 4.23$, $d=9.3$ kpc, Sp. Type: $B0.5 V_0$, $H-K_s = 2.57$ mag. BP2(1a,1b): 0.2, 0.43 pc; 0° , 180° ; 1.0, 3.0; K(2): 0.74 pc; 85° ; K(3): 1.09 pc; 85° ; K(4): 0.71 pc; 250° .

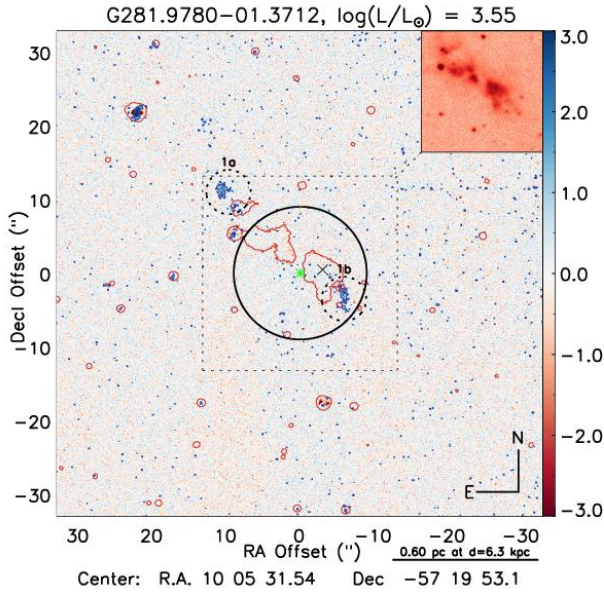


Figure A231. G281.9780-01.3712, $\log(L/L_{\odot}) = 3.55$, $d=6.3$ kpc, Sp. Type: B2 V₀, $H-K_s = 2.84$ mag. BP2(1a,1b): 0.43, 0.32 pc; 50°, 230°; 5.7, 6.0.

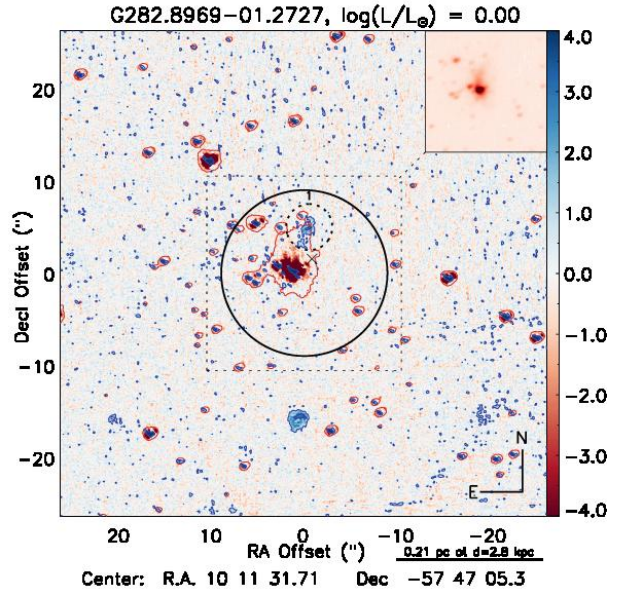


Figure A234. G282.8969-01.2727, $d=2.8$ kpc, $H-K_s = 2.12$ mag. BP1(1): 0.08 pc; 350°; 5.5.

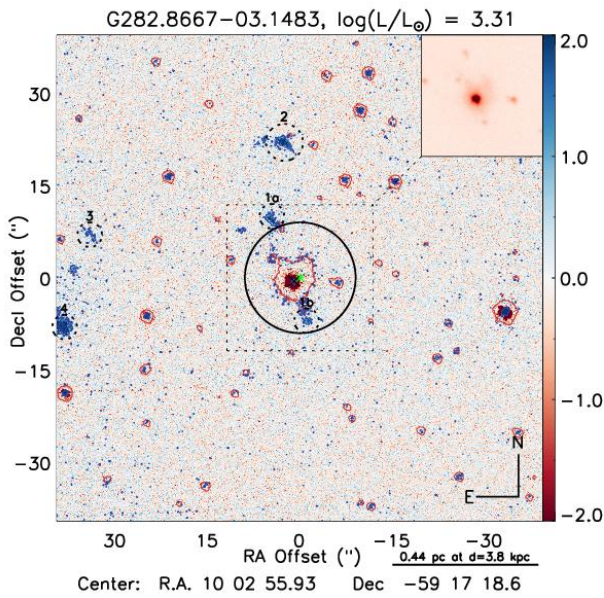


Figure A233. G282.8667-03.1483, $\log(L/L_{\odot}) = 3.85$, $d=2.6$ kpc, Sp. Type: B3 V₀, $H-K_s = 3.45$ mag. BP2(1a,1b): 0.22, 0.13 pc; 20°, 200°; 7.0, 5.3; K(2): 0.42 pc; 5°; K(3): 0.63 pc; 75°; K(4): 0.69 pc; 110°.

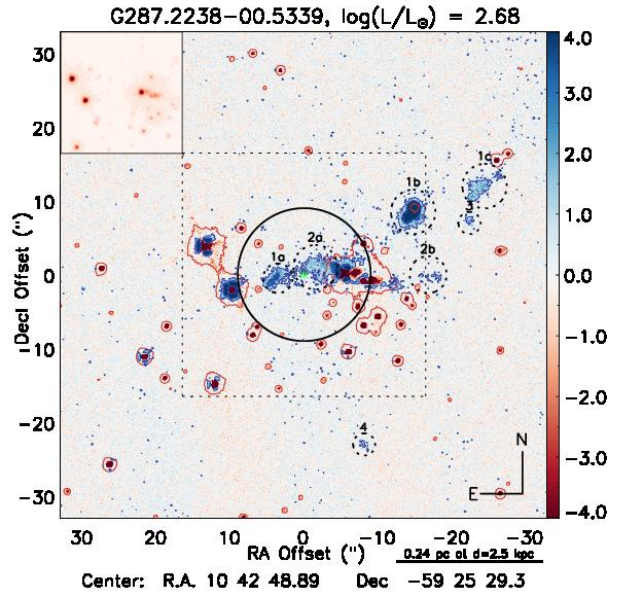


Figure A237. G287.2238-00.5339, $\log(L/L_{\odot}) = 2.68$, $d=2.5$ kpc, Sp. Type: <B3 V₀, $H-K_s = 1.43$ mag. BP4(1a,1b,1c): 0.21, 0.21 pc; 115°, 295°; 6.3, 6.3; BP4(2a,2b): 0.13, 0.13 pc; 85°, 265°; 3.8, 3.8; K(3): 0.23 pc; 295°; K(4): 0.29 pc; 200°.

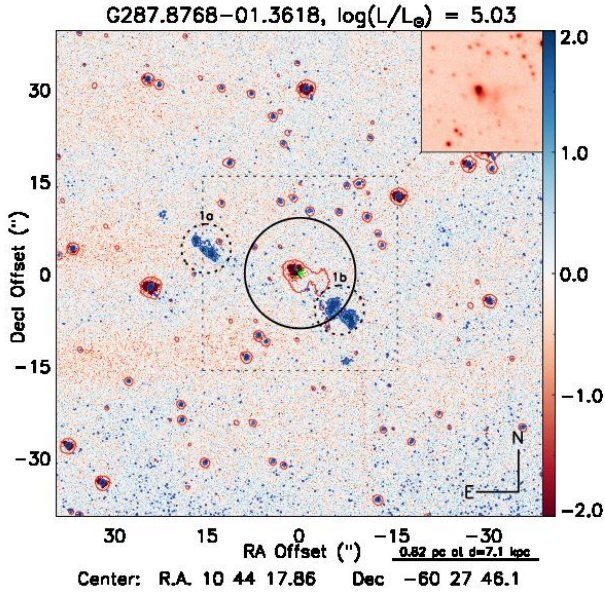


Figure A238. G287.8768-01.3618, $\log(L/L_\odot) = 3.85$, $d=2.6$ kpc, Sp. Type: O7.5 V, $H-K_s = 3.33$ mag. BP2(1a,1b): 0.47, 0.59 pc; 65° , 245° ; 5.3, 10.0.

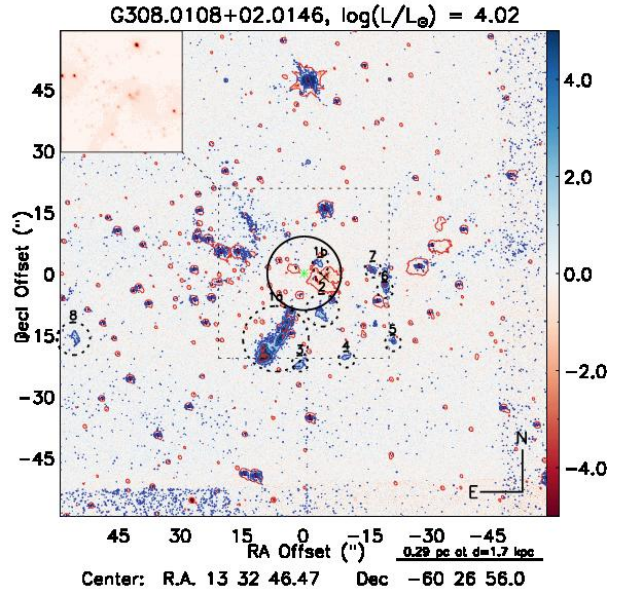


Figure A274. G308.0108+02.0146, $\log(L/L_\odot) = 4.02$, $d=1.7$ kpc, Sp. Type: B1 V₀, $H-K_s = 3.43$ mag. BP2(1a,1b): 0.20, 0.03 pc; 150° , 330° ; 4.0, 7.5; K(2): 0.08 pc; 205° ; K(3): 0.18 pc; 175° ; K(4): 0.18 pc; 205° ; K(5): 0.21 pc; 235° ; K(6): 0.14 pc; 265° ; K(7): 0.12 pc; 280° .

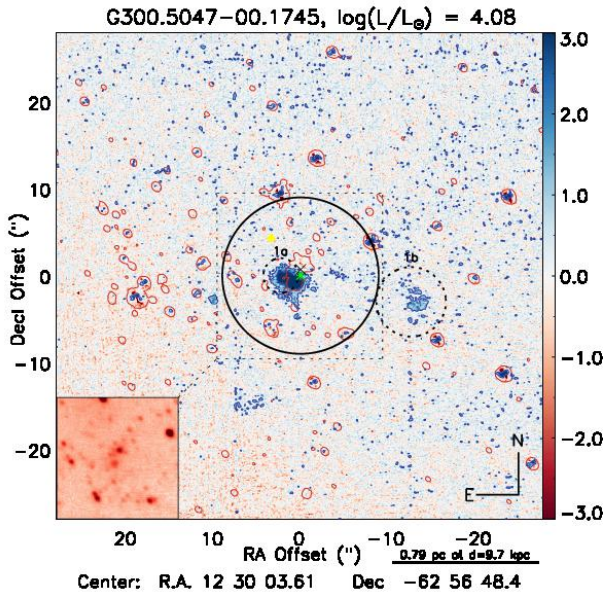


Figure A255. G300.5047-00.1745, $\log(L/L_\odot) = 4.08$, $d=9.7$ kpc, Sp. Type: B0.5 V₀, $H-K_s = 1.25$ mag. BP2(1a,1b): 0.11, 0.67 pc; 80° , 260° ; 1.0, 4.8.

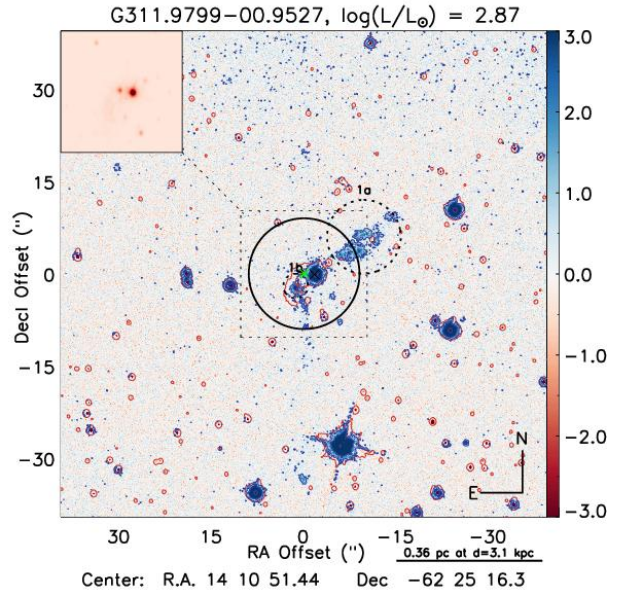


Figure A287. G311.9799-00.9527, $\log(L/L_\odot) = 2.87$, $d=3.1$ kpc, Sp. Type: <B3 V₀, $H-K_s = 0.93$ mag. BP2(1a,1b): 0.26, 0.06 pc; 305° , 125° ; 5.7, 2.0.

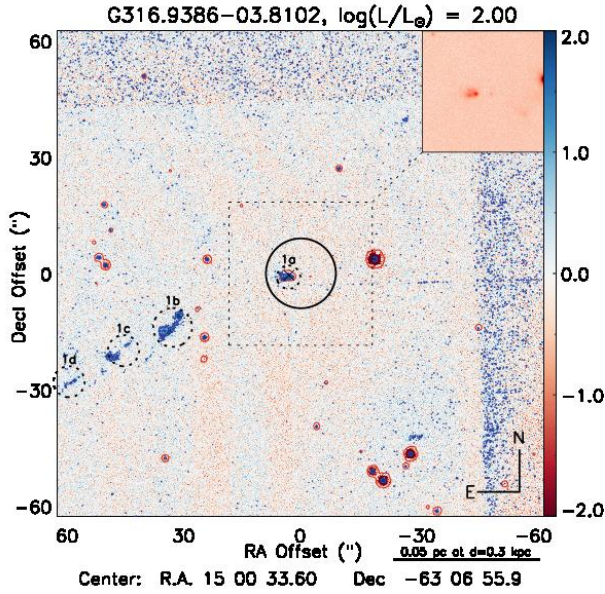


Figure A292. G316.9386-03.8102, $\log(L/L_{\odot}) = 2.00$, $d=0.3$ kpc, Sp. Type: $<B3 V_0$, $H-K_s = 1.97$ mag. BP1(1a,1b,1c,1d): 0.10 pc; 115° ; 15.0 .

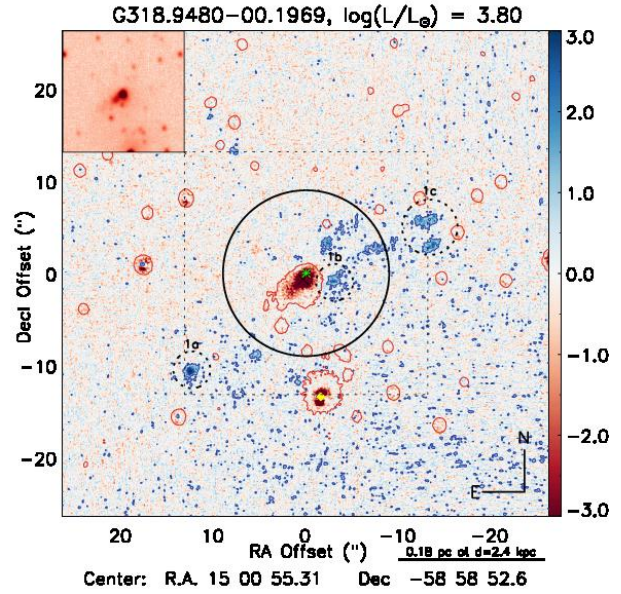


Figure A296. G318.9480-00.1969, $\log(L/L_{\odot}) = 3.80$, $d=2.4$ kpc, Sp. Type: $B1 V_0$ star, $H-K_s = 3.06$ mag. BP2(1a,1b,1c): 0.20, 0.18 pc; 125° , 300° ; 12.7 , 4.4 .

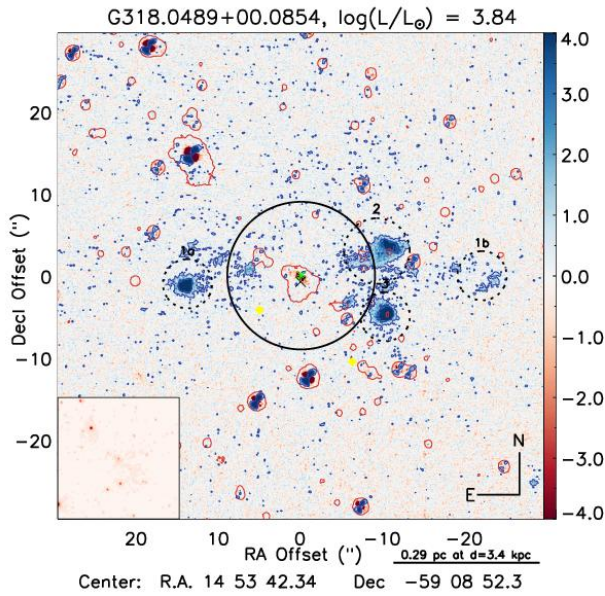


Figure A295. G318.0489+00.0854, $\log(L/L_{\odot}) = 3.84$, $d=3.4$ kpc, Sp. Type: $B1 V_0$, $H-K_s = 3.17$ mag. BP4(1a,1b,2,3): 0.23, 0.31 pc; 90° , 270° , 290° , 245° ; 7.3 , 7.5 .

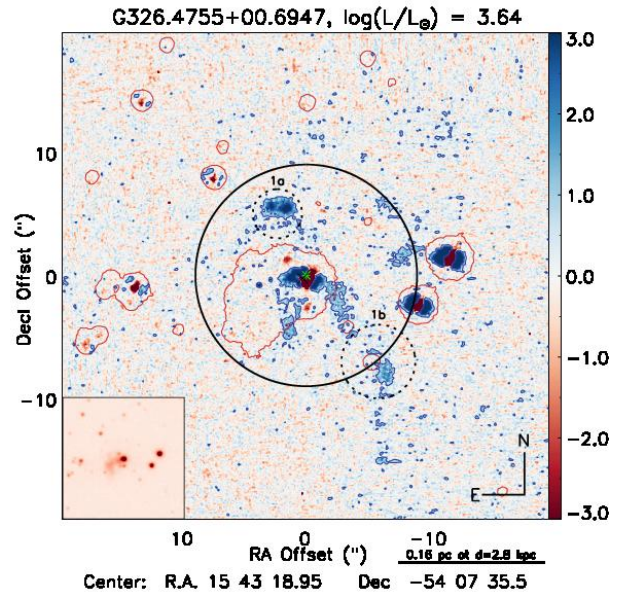


Figure A307. G326.4755+00.6947, $\log(L/L_{\odot}) = 3.64$, $d=2.8$ kpc, Sp. Type: $B2 V_0$, $H-K_s = 3.14$ mag. BP2(1a,1b): 0.09, 0.14 pc; 35° , 215° ; 3.0 , 4.8 .

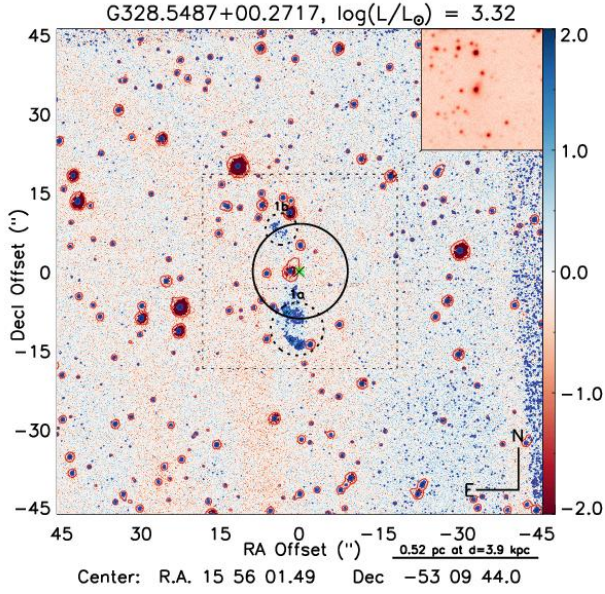


Figure A315. G328.5487+00.2717, $\log(L/L_\odot) = 3.32$, $d=3.9$ kpc, Sp. Type: B3 V₀, $H-K_s = 2.25$ mag. BP2(1a,1b): 0.35, 0.26 pc; 10° , 185° ; 4.2, 5.3.

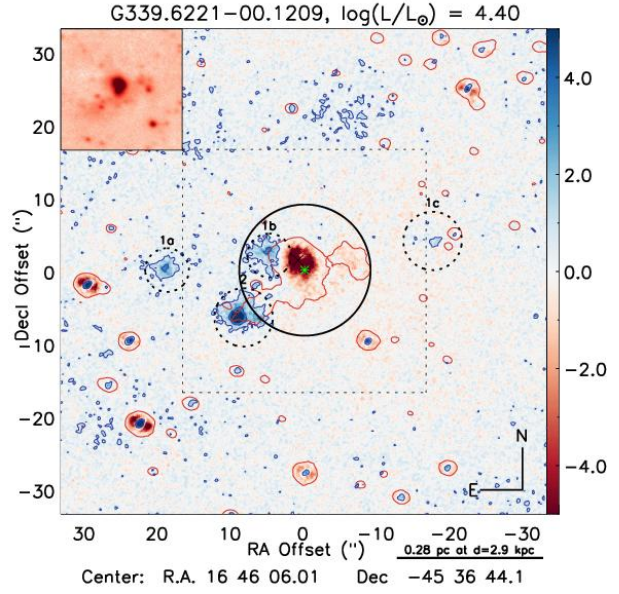


Figure A341. G339.6221-00.1209, $\log(L/L_\odot) = 4.40$, $d=2.9$ kpc, Sp. Type: B0 V, $H-K_s = 2.49$ mag. BP2(1a,1b,1c): 0.30, 0.28 pc; 90° , 75° , 275° ; 7.8, 9.3; K(2): 0.19 pc; 135° .

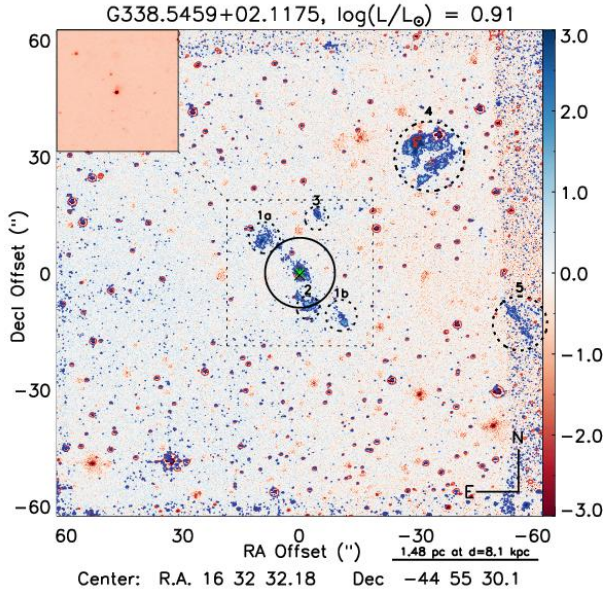


Figure A337. G338.5459+02.1175, $\log(L/L_\odot) = 0.91$, $d=8.1$ kpc, Sp. Type: <B3 V₀, $H-K_s = 1.42$ mag. BP2(1a,1b): 0.49, 0.61 pc; 45° , 225° ; 5.3, 6.7; K(2): 0.34 pc; 205° ; K(3): 0.62 pc; 345° ; D(4): 1.83 pc; 315° ; D(5): 2.14 pc; 255° .

APPENDIX B: FULL TABLES

Table B1. Log of observations.

ID	MSX name	R.A. (J2000)	Decl. (J2000)	d_{kin} (kpc)	$\log(L/L_\odot)$	Telescope	Semester
001	G016.7981+00.1264	18:20:55.28	-14:15:30.80	14.6	5.14	SOAR	2011A
002	G017.0332+00.7476	18:19:07.33	-13:45:23.60	13.8	4.64	SOAR	2011A
003	G017.6380+00.1566	18:22:26.37	-13:30:12.00	2.3	4.77	SOAR	2011A
004	G018.6608+00.0372	18:24:50.24	-12:39:22.40	10.8	4.29	CFHT	2012A
005	G019.7268-00.1132	18:27:25.20	-11:46:59.10	11.7	4.53	CFHT	2012A
006	G019.8817-00.5347	18:29:14.68	-11:50:23.60	3.5	3.94	CFHT	2012A
007	G019.9224-00.2577	18:28:18.96	-11:40:36.70	11.4	4.29	CFHT	2012A
008	G019.9386-00.2079	18:28:09.88	-11:38:22.90	4.5	3.35	CFHT	2012A
009	G020.5143+00.4936	18:26:43.49	-10:48:18.50	13.6	4.10	CFHT	2012A
010	G020.7438-00.0952	18:29:16.96	-10:52:27.10	11.7	4.95	SOAR	2011A
011	G020.7491-00.0898	18:29:16.39	-10:52:01.20	11.7	4.95	SOAR	2011A
012	G022.3554+00.0655	18:31:44.20	-9:22:17.00	5.2	4.23	CFHT	2012A
013	G023.2628+00.0713	18:33:24.76	-8:33:50.00	4.9	3.88	CFHT	2012A
014	G023.3891+00.1851	18:33:14.32	-8:23:57.40	4.8	4.67	SOAR	2011A
015	G023.4394-00.2394	18:34:51.32	-8:32:55.00	6.0	4.36	CFHT	2012A
016	G023.5852+00.0287	18:34:10.00	-8:17:51.00	6.1	4.12	CFHT	2012A
017	G023.6566-00.1273	18:34:51.56	-8:18:21.60	5.0	4.17	CFHT	2012A
018	G023.7097+00.1701	18:33:53.49	-8:07:18.40	6.4	4.94	CFHT	2012A
019	G023.8176+00.3841	18:33:19.54	-7:55:37.80	4.8	3.62	CFHT	2012A
020	G023.8983+00.0648	18:34:37.18	-8:00:12.40	3.0	3.86	CFHT	2012A
021	G024.0946+00.4565	18:33:34.92	-7:38:53.50	5.6	3.50	CFHT	2012A
022	G024.5076-00.2222	18:36:46.87	-7:35:38.40	9.6	5.06	CFHT	2012A
023	G024.6343-00.3233	18:37:22.68	-7:31:41.50	12.3	4.90	CFHT	2012A
024	G024.7320+00.1530	18:35:50.91	-7:13:27.20	9.1	4.26	CFHT	2012A
025	G025.4118+00.1052	18:37:16.99	-6:38:25.40	5.7	3.97	CFHT	2012A
026	G025.6498+01.0491	18:34:20.89	-5:59:42.50	12.3	5.50	SOAR	2011A
027	G026.0552+00.5421	18:36:54.62	-5:52:05.50	12.1	4.38	CFHT	2012A
028	G026.4897-00.5455	18:41:35.92	-5:58:50.70	10.8	4.58	SOAR	2011A
029	G026.5254-00.2667	18:40:40.25	-5:49:12.90	8.9	3.72	CFHT	2012A
030	G026.5972-00.0241	18:39:55.91	-5:38:44.70	13.3	4.81	CFHT	2012A
031	G026.6085-00.2122	18:40:37.58	-5:43:21.30	8.8	4.48	CFHT	2012A
032	G027.1852-00.0812	18:41:13.26	-5:08:57.70	2.0	3.35	CFHT	2012A
033	G028.6096+00.0170	18:43:28.49	-3:50:19.30	8.8	5.29	CFHT	2012A
034	G028.8621+00.0657	18:43:46.24	-3:35:29.20	8.7	5.30	CFHT	2012A
035	G029.5867-00.6598	18:47:41.01	-3:16:40.40	10.0	4.28	CFHT	2012A
036	G030.2531+00.0536	18:47:31.70	-3:15:14.00	10.1	4.25	CFHT	2012A
037	G029.5904-00.6144	18:46:21.47	-2:21:35.40	10.2	4.60	CFHT	2012A
038	G030.2971+00.0549	18:46:25.79	-2:19:13.70	12.0	4.31	CFHT	2012A
039	G030.6877-00.0729	18:47:36.19	-2:01:49.40	9.1	5.22	CFHT	2012A
040	G030.6931-00.0474	18:47:31.31	-2:00:50.40	9.2	5.07	CFHT	2012A
041	G030.7206-00.0826	18:47:41.85	-2:00:20.10	5.6	4.56	CFHT	2012A
042	G030.8053-00.0403	18:47:42.11	-1:54:39.60	8.8	5.01	CFHT	2012A
043	G030.8185+00.2729	18:46:36.58	-1:45:22.40	6.2	4.09	CFHT	2012A
044	G030.9585+00.0862	18:47:31.83	-1:42:59.60	11.8	4.70	CFHT	2012A
045	G030.9726-00.1410	18:48:22.03	-1:48:30.30	9.7	3.90	CFHT	2012A
046	G030.9959-00.0771	18:48:10.65	-1:45:25.30	9.5	4.21	CFHT	2012A
047	G031.1593+00.0456	18:48:02.67	-1:33:24.40	11.8	4.06	CFHT	2012A
048	G032.0451+00.0589	18:49:36.56	0:45:45.40	8.3	4.76	SOAR	2011A
049	G032.7946+00.2053	18:50:27.43	0:01:42.60	13.3	4.57	SOAR	2011A
050	G033.3891+00.1989	18:51:33.82	0:29:51.00	5.5	4.08	CFHT	2012A
051	G033.3933+00.0100	18:52:14.66	0:24:55.00	6.9	4.17	CFHT	2012A
052	G033.5237+00.0198	18:52:26.83	0:32:08.50	6.9	3.98	CFHT	2012A
053	G034.7123-00.5946	18:56:48.23	1:18:47.50	3.0	3.95	CFHT	2012A
054	G034.8211+00.3519	18:53:37.88	1:50:30.50	10.2	4.84	SOAR	2011A
055	G035.3449+00.3474	18:54:36.14	2:18:20.20	6.8	3.95	CFHT	2012A
056	G035.8546+00.2663	18:55:49.41	2:43:21.00	2.0	3.12	CFHT	2012A
057	G036.9194+00.4825	18:56:59.78	3:46:03.90	12.7	4.00	CFHT	2012A
058	G037.3412-00.0600	18:59:42.28	3:53:49.10	9.8	4.19	CFHT	2012A
059	G037.4974+00.5301	18:57:53.37	4:18:17.50	0.6	2.12	CFHT	2012A
060	G038.3543-00.9519	19:04:44.86	4:23:17.88	1.1	0.00	CFHT	2011B
061	G039.3880-00.1421	19:03:45.29	5:40:42.40	4.6	3.39	CFHT	2011B
062	G039.4943-00.9933	19:06:59.68	5:22:53.40	3.6	3.90	CFHT	2011B
063	G039.9284-00.3741	19:05:35.27	6:03:01.30	8.9	3.82	CFHT	2011B
064	G040.4247+00.6989	19:02:39.62	6:59:08.50	0.8	1.64	CFHT	2011B

Table B1 – *continued* Log of observations.

ID	MSX name	R.A. (J2000)	Decl. (J2000)	d_{kin} (kpc)	$\log(L/L_{\odot})$	Telescope	Semester
065	G041.0780-00.6365	19:08:39.23	6:57:07.20	7.0	3.57	CFHT	2011B
066	G042.0977+00.3521	19:07:00.53	8:18:44.30	11.2	4.81	SOAR	2011A
067	G042.1099-00.4466	19:09:53.57	7:57:14.50	8.7	3.95	CFHT	2011B
068	G043.0786+00.0033	19:10:05.01	9:01:15.60	0.9	1.63	CFHT	2011B
069	G043.1497+00.0272	19:10:05.01	9:01:15.60	12.3	4.67	CFHT	2011B
070	G043.1650-00.0285	19:10:21.80	9:05:02.90	11.6	6.28	CFHT	2011B
071	G043.1679+00.0095	19:10:13.45	9:06:12.90	11.7	5.87	CFHT	2011B
072	G043.1759+00.0244	19:10:11.64	9:07:05.50	11.7	5.64	CFHT	2011B
073	G043.1824-00.0260	19:10:23.25	9:06:02.10	11.7	5.42	CFHT	2011B
074	G043.2376-00.0433	19:10:33.16	9:08:29.40	11.9	5.12	CFHT	2011B
075	G043.7955-00.1275	19:11:54.07	9:35:50.20	9.2	5.16	SOAR	2011A
076	G043.8152-00.1172	19:11:54.09	9:37:10.50	8.9	3.99	CFHT	2011B
077	G043.9956-00.0111	19:11:51.64	9:49:40.40	6.9	4.32	CFHT	2011B
078	G044.2836-00.5249	19:14:14.92	9:50:43.80	6.1	3.88	CFHT	2011B
079	G045.1894-00.4387	19:15:39.00	10:41:14.30	5.9	3.84	CFHT	2011B
080	G053.0366+00.1110	19:28:55.65	17:51:59.50	10.0	3.60	CFHT	2010B
081	G061.7201+00.8630	19:44:23.64	25:48:43.40	15.9	4.89	CFHT	2010B
082	G076.0902+00.1412	20:23:27.29	37:34:53.90	4.5	3.85	CFHT	2010B
083	G076.1877+00.0974	20:23:55.10	37:38:09.70	4.9	4.91	CFHT	2010B
084	G077.4052-01.2136	20:32:54.10	37:51:29.70	4.6	3.67	CFHT	2010B
085	G077.8999+01.7678	20:21:55.01	39:59:45.50	4.5	3.88	CFHT	2010B
086	G077.9550+00.0058	20:29:31.76	39:01:20.70	4.7	4.24	CFHT	2010B
087	G077.9637-00.0075	20:29:36.88	39:01:15.60	4.5	5.14	CFHT	2010B
088	G078.4373+02.6584	20:19:38.49	40:56:33.70	3.8	4.71	CFHT	2010B
089	G078.7641+01.6862	20:24:51.66	40:39:25.20	12.4	4.77	CFHT	2010B
090	G078.8699+02.7602	20:20:30.48	41:21:25.90	1.6	3.92	CFHT	2010B
091	G078.8867+00.7087	20:29:24.86	40:11:19.40	4.7	5.56	CFHT	2010B
092	G079.1272+02.2782	20:23:23.83	41:17:39.30	4.1	4.19	CFHT	2010B
093	G079.3202+01.3131	20:28:10.24	40:53:37.80	8.5	4.69	CFHT	2010B
094	G079.3248+01.2901	20:28:16.15	40:52:57.90	8.5	4.72	CFHT	2010B
095	G079.3305+01.2823	20:28:20.03	40:53:03.10	8.6	4.36	CFHT	2010B
096	G079.3398+00.3417	20:32:22.17	40:20:17.10	3.6	3.28	CFHT	2010B
097	G079.3439+00.3191	20:32:28.68	40:19:41.10	3.6	3.29	CFHT	2010B
098	G081.6632+00.4651	20:39:16.77	42:16:09.40	1.2	2.25	CFHT	2010B
099	G081.7131+00.5792	20:38:57.19	42:22:40.90	3.7	4.52	CFHT	2010B
100	G081.7220+00.5699	20:39:01.01	42:22:50.20	3.9	3.54	CFHT	2010B
101	G081.7522+00.5906	20:39:02.01	42:24:58.60	3.8	4.11	CFHT	2010B
102	G081.7624+00.5916	20:39:03.72	42:25:29.60	3.9	3.74	CFHT	2010B
103	G081.8375+00.9134	20:37:55.31	42:40:48.00	3.4	3.16	CFHT	2010B
104	G081.8652+00.7800	20:38:35.42	42:37:15.90	1.2	3.41	CFHT	2010B
105	G081.8789+00.7822	20:38:37.56	42:38:00.20	1.2	4.20	CFHT	2010B
106	G082.0333+02.3249	20:32:21.91	43:40:56.20	3.0	4.00	CFHT	2010B
107	G082.5682+00.4040	20:42:33.76	42:56:51.30	1.0	3.32	CFHT	2010B
108	G084.5978+00.1408	20:50:42.81	44:21:55.40	2.9	3.10	CFHT	2010B
109	G085.0331+00.3629	20:51:18.38	44:50:33.00	2.7	3.22	CFHT	2010B
110	G090.7764+02.8281	21:02:21.50	50:48:34.50	3.1	3.39	CFHT	2010B
111	G093.1610+01.8687	21:17:14.17	51:54:23.00	8.4	4.17	CFHT	2010B
112	G094.3228-00.1671	21:31:45.16	51:15:35.60	5.6	3.96	CFHT	2010B
113	G094.4637-00.8043	21:35:09.11	50:53:09.60	6.2	4.51	CFHT	2010B
114	G094.6028-01.7966	21:39:58.25	50:14:20.90	6.2	4.84	CFHT	2010B
115	G095.0531+03.9724	21:15:55.63	54:43:31.00	10.7	4.27	CFHT	2010B
116	G096.4353+01.3233	21:35:21.23	53:47:12.00	8.7	4.26	CFHT	2010B
117	G097.9978+01.4688	21:42:43.19	54:55:51.90	8.1	3.85	CFHT	2010B
118	G098.0361+01.4462	21:43:01.46	54:56:18.90	7.9	5.16	CFHT	2010B
119	G098.8555+02.9344	21:40:28.98	56:35:55.60	0.5	1.78	CFHT	2010B
120	G100.2124+01.8829	21:52:57.15	56:39:54.20	7.4	4.22	CFHT	2010B
121	G100.3779-03.5784	22:16:10.35	52:21:34.70	4.8	4.46	CFHT	2010B
122	G102.3340+03.6094	21:57:25.70	59:19:59.10	10.5	4.01	CFHT	2010B
123	G102.3533+03.6360	21:57:25.19	59:21:56.60	10.7	5.23	CFHT	2010B
124	G107.6823-02.2423	22:55:29.82	57:09:24.90	6.1	3.84	CFHT	2010B
125	G108.4714-02.8176	23:02:32.03	56:57:53.20	5.9	3.94	CFHT	2010B
126	G108.7575-00.9863	22:58:47.49	58:45:01.00	5.5	4.35	CFHT	2010B
127	G109.0775-00.3524	22:58:58.89	59:27:35.60	5.3	3.62	CFHT	2010B
128	G109.0974-00.3458	22:59:05.52	59:28:23.20	5.1	4.61	CFHT	2010B

Table B1 – continued Log of observations.

ID	MSX name	R.A. (J2000)	Decl. (J2000)	d_{kin} (kpc)	$\log(L/L_\odot)$	Telescope	Semester
129	G109.8715+02.1156	22:56:17.97	62:01:54.40	1.5	4.58	CFHT	2010B
130	G110.0931-00.0641	23:05:25.08	60:08:16.00	5.7	4.30	CFHT	2010B
131	G110.1082+00.0473	23:05:10.15	60:14:42.70	5.6	4.69	CFHT	2010B
132	G110.4771+01.4803	23:03:12.86	61:42:24.10	1.5	2.59	CFHT	2010B
133	G111.5234+00.8004	23:13:32.39	61:29:06.20	6.2	4.56	CFHT	2010B
134	G111.5320+00.7593	23:13:43.89	61:26:58.20	6.1	4.33	CFHT	2010B
135	G111.5423+00.7776	23:13:45.36	61:28:10.30	6.1	5.90	CFHT	2010B
136	G111.5671+00.7517	23:14:01.70	61:27:19.00	6.1	5.39	CFHT	2010B
137	G111.5851+00.7976	23:14:01.68	61:30:16.50	6.0	4.45	CFHT	2010B
138	G111.6115+00.3735	23:15:31.22	61:07:09.40	6.0	5.31	CFHT	2010B
139	G114.0835+02.8568	23:28:27.86	64:17:37.30	5.5	4.08	CFHT	2010B
140	G120.1483+03.3745	0:23:57.07	66:05:51.00	7.3	4.54	CFHT	2010B
141	G120.1557+03.3885	0:24:00.50	66:06:43.90	7.3	4.29	CFHT	2010B
142	G124.0144-00.0267	1:00:55.24	62:49:30.00	4.3	3.46	CFHT	2010B
143	G125.6045+02.1038	1:16:36.21	64:50:38.40	5.5	3.89	CFHT	2010B
144	G126.4274-01.2348	1:20:44.25	61:26:16.00	1.3	2.23	CFHT	2010B
145	G126.7144-00.8220	1:23:33.17	61:48:48.20	1.4	3.98	CFHT	2010B
146	G133.6945+01.2166	2:25:30.99	62:06:20.90	4.6	5.22	CFHT	2010B
147	G133.7150+01.2155	2:25:40.77	62:05:52.40	4.6	5.22	CFHT	2010B
148	G133.7354+01.1827	2:25:44.51	62:03:36.00	3.8	4.64	CFHT	2010B
149	G134.2792+00.8561	2:29:01.96	61:33:31.60	5.6	4.39	CFHT	2010B
150	G135.2774+02.7981	2:43:28.65	62:57:09.30	9.3	4.83	CFHT	2010B
151	G136.3542+00.9543	2:45:10.41	60:49:37.50	7.5	4.06	CFHT	2011A
152	G136.5370+02.8934	2:53:43.36	62:29:23.60	5.3	3.36	CFHT	2011A
153	G138.2957+01.5552	3:01:31.63	60:29:12.10	4.0	4.43	CFHT	2011A
154	G139.9091+00.1969	3:07:24.52	58:30:43.30	4.3	4.30	CFHT	2012A
155	G141.9996+01.8202	3:27:38.76	58:47:00.10	1.4	3.64	CFHT	2011A
156	G142.2446+01.4299	3:27:31.37	58:19:21.80	5.7	4.46	CFHT	2011A
157	G143.8118-01.5699	3:24:51.04	54:57:30.60	3.5	4.27	CFHT	2011A
158	G144.6678-00.7136	3:33:10.01	55:10:54.90	2.8	2.87	CFHT	2011A
159	G148.1201+00.2928	3:56:15.36	53:52:13.00	4.3	3.84	CFHT	2011A
160	G151.6120-00.4575	4:10:11.86	50:59:54.40	8.9	4.61	CFHT	2011A
161	G172.8742+02.2687	5:36:52.46	36:10:57.30	16.8	4.34	CFHT	2011A
162	G173.4839+02.4317	5:39:09.92	35:45:17.20	22.3	5.55	CFHT	2012A
163	G173.5826+02.4452	5:39:28.65	35:40:41.80	20.9	4.64	CFHT	2012A
164	G173.6328+02.8064	5:41:07.03	35:49:34.80	34.0	5.94	CFHT	2010B
165	G173.6339+02.8218	5:41:11.18	35:50:03.40	34.0	6.18	CFHT	2010B
166	G173.7215+02.6924	5:40:52.36	35:41:29.40	24.4	5.88	CFHT	2010B
167	G188.9479+00.8871	6:08:53.40	21:38:28.10	1.0	3.37	CFHT	2010B
168	G189.0307+00.7821	6:08:40.52	21:31:00.40	0.8	3.50	CFHT	2010B
169	G189.8557+00.5011	6:09:20.01	20:39:33.40	2.7	3.33	CFHT	2010B
170	G192.5843-00.0417	6:12:53.44	18:00:24.40	2.2	3.48	CFHT	2010B
171	G192.6005-00.0479	6:12:54.04	17:59:22.50	1.8	4.45	CFHT	2010B
172	G192.9089-00.6259	6:13:04.03	17:58:36.10	1.7	2.82	CFHT	2010B
173	G192.6308-00.0194	6:11:23.69	17:26:29.70	8.0	4.78	CFHT	2010B
174	G194.9259-01.1946	6:13:21.11	15:23:57.10	3.9	4.00	CFHT	2010B
175	G194.9349-01.2224	6:13:16.14	15:22:43.30	3.7	3.97	CFHT	2011B
176	G196.1620-01.2546	6:15:34.56	14:17:04.90	2.1	3.32	CFHT	2011B
177	G196.4542-01.6777	6:14:36.82	13:49:35.80	3.9	4.70	CFHT	2011B
178	G200.0789-01.6323	6:21:47.59	10:39:21.50	7.9	4.15	CFHT	2011B
179	G202.6270+02.3747	6:41:02.49	10:15:03.90	1.0	2.72	CFHT	2011B
180	G203.3166+02.0564	6:41:10.12	9:29:33.70	1.0	3.50	CFHT	2011B
181	G203.7637+01.2705	6:39:09.91	8:44:09.20	1.3	3.10	CFHT	2011B
182	G206.7804-01.9395	6:33:15.91	4:34:54.10	1.8	3.42	CFHT	2011B
183	G212.0641-00.7395	6:47:13.31	0:26:06.00	6.4	4.40	CFHT	2011B
184	G212.2344-03.5038	6:37:41.59	0:58:37.70	6.7	3.65	CFHT	2011B
185	G212.9626+01.2954	6:56:06.32	0:33:47.70	5.7	3.37	CFHT	2011B
186	G213.9180+00.3786	6:54:35.14	0:42:17.80	5.3	3.32	CFHT	2011B
187	G214.4934-01.8103	6:47:50.25	-2:12:53.20	3.0	3.11	CFHT	2011B
188	G215.8902-02.0094	6:49:40.23	-3:32:52.40	8.3	3.69	CFHT	2011B
189	G217.6047-02.6170	6:50:37.41	-5:21:00.90	9.2	3.88	CFHT	2011B
190	G222.4278-03.1357	6:57:35.20	-9:52:40.80	1.1	2.73	CFHT	2011B
191	G224.6065-02.5563	7:03:43.16	-11:33:06.20	1.3	3.52	CFHT	2011B
192	G224.6075-01.0063	7:09:20.55	-10:50:28.10	1.6	3.20	CFHT	2011B

Table B1 – *continued* Log of observations.

ID	MSX name	R.A. (J2000)	Decl. (J2000)	d_{kin} (kpc)	$\log(L/L_{\odot})$	Telescope	Semester
193	G225.3266-00.5318	7:12:24.40	-11:15:34.90	1.6	2.87	CFHT	2011B
194	G231.7986-01.9682	7:19:35.92	-17:39:18.00	4.3	3.74	CFHT	2011B
195	G231.9005-02.1378	7:19:10.17	-17:49:27.40	4.4	2.96	CFHT	2011B
196	G232.0766-02.2767	7:18:59.92	-18:02:41.20	4.1	3.67	CFHT	2011B
197	G232.6207+00.9959	7:32:09.66	-16:58:12.80	1.6	4.00	CFHT	2011B
198	G233.8306-00.1803	7:30:16.65	-18:35:48.80	4.4	4.27	CFHT	2011B
199	G242.9402-00.4501	7:48:43.12	-26:39:31.30	6.7	3.71	SOAR	2011B
200	G251.2337-01.9535	8:02:43.10	-34:31:49.00	5.9	4.31	SOAR	2011B
201	G254.0491-00.5615	8:15:57.12	-36:08:08.10	4.1	3.85	SOAR	2011B
202	G259.0453-01.5559	8:26:17.22	-40:48:40.50	7.0	4.06	SOAR	2011B
203	G259.0459-01.9107	8:24:43.58	-41:00:55.84	2.2	2.18	SOAR	2011B
204	G259.6154-02.6940	8:23:03.92	-41:55:39.21	6.6	3.62	SOAR	2011B
205	G259.6695-01.3181	8:29:13.82	-41:10:48.30	7.0	3.40	SOAR	2011B
206	G259.7592-02.8378	8:22:52.22	-42:07:55.90	2.1	3.31	SOAR	2011B
207	G259.9395-00.0419	8:35:31.01	-40:38:22.10	1.7	2.62	SOAR	2011B
208	G260.9252+00.1149	8:39:20.20	-41:19:50.80	2.0	3.07	SOAR	2011B
209	G261.6429-02.0922	8:32:07.46	-43:13:48.70	2.7	2.72	SOAR	2011B
210	G263.5846-03.9973	8:29:53.20	-45:55:09.50	14.9	3.97	SOAR	2011B
211	G263.7434+00.1161	8:48:48.64	-43:32:29.00	2.6	3.85	SOAR	2011B
212	G263.7759-00.4281	8:46:34.84	-43:54:29.80	1.6	3.66	SOAR	2011B
213	G264.1444+02.0190	8:58:12.81	-42:37:38.60	2.0	3.83	SOAR	2011B
214	G264.2918+01.4700	8:56:27.71	-43:05:47.40	1.9	3.97	SOAR	2011B
215	G265.1438+01.4548	8:59:27.53	-43:45:17.84	2.0	3.75	SOAR	2011B
216	G265.3344+01.3916	8:59:53.20	-43:56:13.90	1.9	2.55	SOAR	2011B
217	G267.7336-01.1058	8:58:04.20	-47:23:10.00	2.1	3.66	SOAR	2011B
218	G267.9094+01.7816	9:11:14.23	-45:35:11.00	1.1	2.60	SOAR	2011B
219	G268.0594-00.8040	9:00:41.06	-47:26:01.60	2.1	2.70	SOAR	2011B
220	G268.3921-03.0659	8:51:37.05	-49:09:08.60	1.6	2.54	SOAR	2011B
221	G268.3957-00.4842	9:03:24.93	-47:28:11.99	3.1	3.91	SOAR	2011B
222	G268.4222-00.8490	9:01:54.28	-47:44:09.60	1.9	4.90	SOAR	2011B
223	G268.4452-00.8442	9:02:01.00	-47:45:00.30	1.9	2.35	SOAR	2011B
224	G269.5205-01.2510	9:04:29.25	-48:49:24.90	2.3	2.83	SOAR	2011B
225	G269.7431-00.3193	9:09:32.98	-48:21:33.70	10.4	4.93	SOAR	2012B
226	G269.8539-00.0630	9:11:08.33	-48:15:56.30	10.2	5.08	SOAR	2012B
227	G271.2225-01.7712	9:09:11.16	-50:25:55.30	10.5	4.69	SOAR	2012B
228	G275.8190-03.6009	9:21:29.24	-55:00:39.50	9.3	4.23	SOAR	2012B
229	G281.0472-01.5432	9:59:15.84	-56:54:45.39	1.6	3.88	SOAR	2011B
230	G281.2206-01.2556	10:01:33.79	-56:47:17.87	0.2	0.07	SOAR	2011B
231	G281.9780-01.3712	10:05:31.53	-57:19:53.00	6.3	3.55	SOAR	2011B
232	G282.7848-01.2869	10:10:46.73	-57:43:55.92	2.7	0.00	SOAR	2011B
233	G282.8667-03.1483	10:02:55.92	-59:17:18.60	3.8	3.31	SOAR	2012B
234	G282.8969-01.2727	10:11:31.70	-57:47:05.28	2.8	3.73	SOAR	2011B
235	G284.6942-00.3600	10:26:36.40	-58:00:32.00	6.2	4.83	SOAR	2012B
236	G286.2086+00.1694	10:38:32.70	-58:19:14.30	2.3	4.89	SOAR	2012B
237	G287.2238-00.5339	10:42:48.88	-59:25:29.20	2.5	2.68	SOAR	2011B
238	G287.8768-01.3618	10:44:17.85	-60:27:46.00	7.1	5.03	SOAR	2012B
239	G287.8893-00.9316	10:46:00.23	-60:05:16.80	2.5	2.67	SOAR	2011B
240	G288.1760-00.8351	10:48:24.23	-60:08:02.00	6.1	4.77	SOAR	2012B
241	G288.9865+00.2533	10:58:00.27	-59:30:44.90	6.6	3.50	SOAR	2012B
242	G289.9446-00.8909	11:01:10.67	-60:57:08.30	9.4	5.52	SOAR	2012B
243	G290.8768-01.2170	11:07:11.38	-61:37:31.60	8.0	4.50	SOAR	2012B
244	G291.5765-00.4310	11:15:04.60	-61:09:37.40	7.9	5.64	SOAR	2012B
245	G293.5607-00.6703	11:30:07.10	-62:03:12.90	3.3	4.66	SOAR	2012B
246	G294.6168-02.3440	11:34:32.85	-63:58:03.00	0.8	2.13	SOAR	2011B
247	G295.1523-00.5890	11:43:25.23	-62:25:40.80	10.8	5.27	SOAR	2012B
248	G295.1662-00.5802	11:43:33.43	-62:25:27.10	11.0	4.58	SOAR	2012B
249	G295.5570-01.3787	11:45:04.73	-63:17:46.10	11.1	4.87	SOAR	2012B
250	G296.4036-01.0185	11:53:08.22	-63:08:56.60	10.4	4.41	SOAR	2012B
251	G296.7256-01.0382	11:55:52.75	-63:14:18.90	10.0	5.00	SOAR	2012B
252	G296.8926-01.3050	11:56:49.75	-63:32:04.90	9.9	4.22	SOAR	2012A
253	G298.8591-00.4372	12:15:25.27	-63:01:17.00	11.1	5.20	SOAR	2012A
254	G300.3412-00.2190	12:28:36.09	-62:58:33.20	4.2	3.76	SOAR	2012A
255	G300.5047-00.1745	12:30:03.60	-62:56:48.40	9.7	4.08	SOAR	2012A
256	G300.7221+01.2007	12:32:50.83	-61:35:28.60	4.1	4.15	SOAR	2012B

Table B1 – continued Log of observations.

ID	MSX name	R.A. (J2000)	Decl. (J2000)	d_{kin} (kpc)	$\log(L/L_\odot)$	Telescope	Semester
257	G301.8147+00.7808	12:41:53.86	-62:04:14.60	4.4	4.33	SOAR	2012A
258	G302.1515-00.9488	12:44:21.93	-63:48:36.00	12.1	3.83	SOAR	2012A
259	G302.4546-00.7401	12:47:08.62	-63:36:30.00	12.6	4.36	SOAR	2012A
260	G302.4867-00.0308	12:47:31.72	-62:53:57.40	4.5	4.10	SOAR	2012A
261	G302.5005-00.7701	12:47:33.11	-63:38:19.30	12.1	3.94	SOAR	2012B
262	G304.7592-00.6299	13:07:47.42	-63:26:37.00	12.2	3.64	SOAR	2012A
263	G305.4748-00.0961	13:13:45.78	-62:51:27.60	6.1	3.57	SOAR	2012A
264	G305.4840+00.2248	13:13:36.04	-62:32:13.50	4.9	3.89	SOAR	2012A
265	G305.5393+00.3394	13:13:59.56	-62:25:07.60	3.2	3.51	SOAR	2012A
266	G305.5610+00.0124	13:14:26.36	-62:44:30.40	5.9	4.96	SOAR	2012A
267	G306.1160+00.1386	13:19:07.89	-62:33:42.80	2.8	4.39	SOAR	2012B
268	G307.3950-00.5838	13:31:04.05	-63:06:42.40	13.6	4.10	SOAR	2012A
269	G307.6138-00.2559	13:32:31.24	-62:45:17.00	7.4	4.59	SOAR	2012A
270	G307.6213-00.2622	13:32:35.49	-62:45:31.30	7.3	4.76	SOAR	2012A
271	G307.7359-00.5945	13:34:03.39	-63:04:04.60	14.0	4.30	SOAR	2012A
272	G308.0023+02.0190	13:32:42.00	-60:26:45.20	1.7	2.27	SOAR	2012B
273	G308.0049-00.3868	13:36:04.87	-62:49:05.10	7.4	3.96	SOAR	2012A
274	G308.0108+02.0146	13:32:46.46	-60:26:56.00	1.7	4.02	SOAR	2012B
275	G308.6480+00.6469	13:39:55.98	-61:40:58.90	6.1	4.30	SOAR	2012A
276	G308.6876+00.5241	13:40:26.71	-61:47:55.30	6.2	3.74	SOAR	2012A
277	G308.7008+00.5312	13:40:32.64	-61:47:19.90	6.3	3.66	SOAR	2012A
278	G308.9176+00.1231	13:43:01.70	-62:08:51.20	5.3	5.27	SOAR	2012A
279	G309.4230-00.6208	13:48:38.86	-62:46:09.50	3.6	3.51	SOAR	2012A
280	G309.9206+00.4790	13:50:42.33	-61:35:07.80	5.3	5.10	SOAR	2012A
281	G310.0135+00.3892	13:51:37.91	-61:39:07.50	3.3	4.74	SOAR	2012A
282	G311.1359-00.2372	14:02:09.92	-61:58:37.70	14.3	4.09	SOAR	2012A
283	G311.4925+00.4021	14:03:34.80	-61:15:52.10	5.5	3.61	SOAR	2012A
284	G311.4942+00.4163	14:03:33.81	-61:15:02.50	5.6	3.68	SOAR	2012A
285	G311.5131-00.4532	14:05:45.83	-62:04:49.10	7.1	4.13	SOAR	2012A
286	G311.6050-00.6369	14:06:58.14	-62:13:49.20	14.7	4.34	SOAR	2012A
287	G311.9799-00.9527	14:10:51.43	-62:25:16.30	3.1	2.87	SOAR	2012B
288	G313.5769+00.3267	14:20:08.35	-60:41:55.30	8.3	4.67	SOAR	2011A
289	G314.3197+00.1125	14:26:26.28	-60:38:31.50	3.6	4.10	SOAR	2012A
290	G316.1386-00.5009	14:42:01.87	-60:30:09.50	7.6	3.62	SOAR	2012A
291	G316.6412-00.0867	14:44:18.84	-59:55:10.50	11.0	4.92	SOAR	2011A
292	G316.9386-03.8102	15:00:33.59	-63:06:55.80	0.3	2.00	SOAR	2012B
293	G316.9531-03.8130	15:00:41.06	-63:06:39.60	0.3	1.65	SOAR	2012B
294	G317.7477+00.0112	14:51:51.97	-59:21:04.20	14.7	4.24	SOAR	2012A
295	G318.0489+00.0854	14:53:42.33	-59:08:52.30	3.4	3.84	SOAR	2012A
296	G318.9480-00.1969	15:00:55.31	-58:58:52.60	2.4	3.80	SOAR	2012A
297	G319.8366-00.1963	15:06:54.49	-58:32:58.70	0.9	2.35	SOAR	2012B
298	G320.2046+00.8626	15:05:21.83	-57:26:49.20	2.8	3.74	SOAR	2012A
299	G320.2437-00.5619	15:11:01.72	-58:39:38.80	9.5	4.26	SOAR	2012A
300	G320.2878-00.3069	15:10:18.73	-58:25:08.70	8.6	4.21	SOAR	2012A
301	G321.0523-00.5070	15:16:06.11	-58:11:41.70	9.1	4.86	SOAR	2011A
302	G321.3803-00.3016	15:17:23.38	-57:51:02.70	9.4	4.35	SOAR	2012A
303	G321.3824-00.2861	15:17:20.21	-57:50:00.30	9.5	4.39	SOAR	2012A
304	G322.1729+00.6442	15:18:38.13	-56:37:32.50	3.8	4.02	SOAR	2012A
305	G323.7410-00.2552	15:31:43.96	-56:30:26.60	10.4	5.24	SOAR	2011A
306	G324.1594+00.2622	15:32:03.90	-55:50:35.70	8.0	4.25	SOAR	2012A
307	G326.4755+00.6947	15:43:18.94	-54:07:35.40	2.8	3.64	SOAR	2012A
308	G326.5437+00.1684	15:45:53.26	-54:30:01.30	9.5	3.99	SOAR	2012A
309	G326.6618+00.5207	15:45:02.84	-54:09:03.00	11.5	5.78	SOAR	2011A
310	G326.7249+00.6159	15:44:59.42	-54:02:17.40	11.4	5.21	SOAR	2011A
311	G327.1192+00.5103	15:47:32.80	-53:52:39.30	5.3	4.68	SOAR	2011A
312	G327.9455-00.1149	15:54:34.59	-53:50:42.10	11.2	4.55	SOAR	2011A
313	G328.2523-00.5320	15:57:59.82	-53:58:00.40	3.1	4.66	SOAR	2011A
314	G328.3442-00.4629	15:58:09.62	-53:51:18.20	11.5	4.73	SOAR	2011A
315	G328.5487+00.2717	15:56:01.48	-53:09:43.90	3.9	3.32	SOAR	2012B
316	G329.0663-00.3081	16:01:09.93	-53:16:02.30	11.7	4.82	SOAR	2012B
317	G329.6098+00.1139	16:02:03.09	-52:35:33.10	10.6	4.67	SOAR	2011A
318	G331.0890+00.0163	16:09:38.88	-51:40:43.80	5.8	3.56	SOAR	2012A
319	G331.3546+01.0638	16:06:25.78	-50:43:22.20	4.8	4.82	SOAR	2011A
320	G331.5651+00.2883	16:10:42.37	-51:09:19.80	11.2	4.00	SOAR	2012A

Table B1 – *continued* Log of observations.

ID	MSX name	R.A. (J2000)	Decl. (J2000)	d_{kin} (kpc)	$\log(L/L_{\odot})$	Telescope	Semester
321	G331.6191-00.0442	16:12:24.61	-51:21:42.40	10.2	3.98	SOAR	2012A
322	G332.0939-00.4206	16:16:16.46	-51:18:25.20	11.2	5.88	SOAR	2011A
323	G332.4683-00.5228	16:18:26.53	-51:07:12.00	11.5	4.53	SOAR	2011A
324	G332.7013-00.5874	16:19:47.46	-51:00:06.60	11.3	4.63	SOAR	2011A
325	G333.1075-00.5020	16:21:14.22	-50:39:12.60	3.7	3.50	SOAR	2012A
326	G333.3151+00.1053	16:19:29.06	-50:04:40.80	3.3	3.67	SOAR	2012A
327	G333.4747-00.2366	16:21:41.68	-50:12:30.90	11.7	4.52	SOAR	2011A
328	G333.9305-00.1319	16:23:13.88	-49:48:42.80	12.2	4.67	SOAR	2011A
329	G334.8438+00.2095	16:25:40.51	-48:55:16.20	10.4	3.16	SOAR	2012B
330	G336.3684-00.0033	16:32:55.85	-47:57:45.50	7.8	4.21	SOAR	2012A
331	G336.8308-00.3752	16:36:26.16	-47:52:30.90	13.7	4.71	SOAR	2011A
332	G337.0963-00.9291	16:39:57.78	-48:02:48.30	12.4	4.16	SOAR	2012A
333	G337.3071-00.1521	16:37:21.57	-47:22:19.50	4.5	3.47	SOAR	2012A
334	G338.0008-00.1498	16:40:04.02	-46:51:18.10	11.3	4.54	SOAR	2011A
335	G338.1127-00.1905	16:40:40.84	-46:47:54.90	12.1	3.83	SOAR	2012A
336	G338.2801+00.5419	16:38:09.14	-46:11:04.50	11.5	4.26	SOAR	2012A
337	G338.5459+02.1175	16:32:32.18	-44:55:30.00	8.1	0.91	SOAR	2012B
338	G338.9196+00.5495	16:40:34.12	-45:42:08.20	4.4	4.55	SOAR	2011A
339	G338.9237+00.5618	16:40:34.12	-45:42:08.20	4.4	4.55	SOAR	2011A
340	G339.3316+00.0964	16:44:04.39	-45:41:27.10	13.2	4.60	SOAR	2011A
341	G339.6221-00.1209	16:46:05.99	-45:36:43.90	2.9	4.40	SOAR	2011A
342	G339.6816-01.2058	16:51:05.85	-46:15:54.70	13.5	4.67	SOAR	2011A
343	G339.8838-01.2588	16:52:04.66	-46:08:33.60	13.2	6.18	SOAR	2011A
344	G340.1537+00.5116	16:45:20.10	-44:47:49.80	12.0	4.10	SOAR	2012A
345	G340.7455-01.0021	16:54:04.05	-45:18:50.00	13.4	5.05	SOAR	2011A
346	G341.2182-00.2136	16:52:17.93	-44:26:53.00	12.5	4.66	SOAR	2011A
347	G342.7057+00.1260	16:56:02.80	-43:04:51.20	12.6	4.80	SOAR	2011A
348	G343.8354-00.1058	17:00:50.86	-42:20:17.40	2.6	3.03	SOAR	2012B
349	G345.1876+01.0308	17:00:30.76	-40:34:22.40	2.0	3.30	SOAR	2012B
350	G345.6985-00.0894	17:06:50.64	-40:50:59.50	0.8	2.43	SOAR	2012B
351	G347.0775-00.3927	17:12:25.81	-39:55:19.90	14.9	5.21	SOAR	2011A
352	G348.0030+00.0728	17:13:18.24	-38:53:58.50	13.3	4.43	SOAR	2011A
353	G348.5477+00.3721	17:13:41.71	-38:16:57.70	1.4	2.05	SOAR	2012B

Table B2. General classification of the sources.

ID	Ext. Continuum Emission	Stellar Cluster	Primary H ₂ Classification	Secondary H ₂ Classification	Components
001	Y	N	N	-	-
002	N	N	BP2	D	BP2(1a,b), D(2a,b)
003	Y	N	D	-	D(1)
004	N	N	N	-	-
005	N	N	N	-	-
006	Y	N	BP2	K	BP2(1a-f),K(2,3,4)
007	Y	N	K	-	K(1,2)
008	N	N	N	-	-
009	N	N	N	-	-
010	N	N	N	-	-
011	N	N	N	-	-
012	N	N	N	-	-
013	N	N	N	-	-
014	N	N	N	-	-
015	N	N	N	-	-
016	N	N	N	-	-
017	N	N	N	-	-
018	Y	N	K	-	K(1,2)
019	N	N	BP2	-	BP2(1a,b)
020	N	N	N	-	-
021	N	N	N	-	-
022	Y	Y	D	-	D(1)
023	Y	N	N	-	-
024	N	N	N	-	-
025	N	N	N	-	-
026	Y	N	BP2	-	BP2(1a-h)
027	N	N	N	-	-
028	N	N	N	-	-
029	N	N	N	-	-
030	N	N	N	-	-
031	N	N	N	-	-
032	N	N	N	-	-
033	N	N	N	-	-
034	Y	Y	K	-	K(1,2,3,4,5)
035	N	N	N	-	-
036	N	N	N	-	-
037	N	N	N	-	-
038	N	N	N	-	-
039	Y	Y	N	-	-
040	N	N	N	-	-
041	N	N	N	-	-
042	N	N	N	-	-
043	Y	N	N	-	-
044	N	N	N	-	-
045	Y	N	BP2	-	BP2(1a,1b)
046	N	N	N	-	-
047	N	N	N	-	-
048	N	N	N	-	-
049	N	N	N	-	-
050	N	N	N	-	-
051	N	N	N	-	-
052	N	N	N	-	-
053	Y	N	D	-	D(1,2,3)
054	N	N	K	-	K(1,2,3,4)
055	N	N	BP2	-	BP2(1a,b)
056	N	N	N	-	-
057	N	N	N	-	-
058	N	N	N	-	-
059	N	N	N	-	-
060	Y	N	K	-	K(1,2)
061	N	N	N	-	-
062	Y	N	N	-	-
063	N	N	N	-	-

Table B2 – *continued* General classification of the sources.

ID	Ext. Continuum Emission	Stellar Cluster	Primary H ₂ Classification	Secondary H ₂ Classification	Components
064	N	N	N	-	-
065	N	N	N	-	-
066	N	Y	N	-	-
067	N	N	N	-	-
068	N	N	N	-	-
069	N	N	N	-	-
070	Y	N	K	-	K(1)
071	N	N	N	-	-
072	Y	N	N	-	-
073	Y	N	N	-	-
074	N	N	N	-	-
075	N	N	N	-	-
076	N	N	N	-	-
077	Y	N	K	-	K(1,2)
078	Y	N	N	-	-
079	N	N	N	-	-
080	N	N	N	-	-
081	N	Y	N	-	-
082	Y	N	K	-	K(1,2)
083	Y	N	N	-	-
084	Y	N	N	-	-
085	Y	Y	K	-	K(1)
086	Y	N	D	-	D(1,2,3,4),D(067-1,067-2)
087	Y	Y	D	-	D(1,2),D(086-1,086-3,086-4)
088	Y	Y	D	-	D(1,2)
089	Y	N	K	D	K(1),D(2)
090	Y	N	BP2	K	BP2(1a,b,c,d),K(2,3)
091	Y	Y	BP2	-	BP2(1a,b)
092	Y	N	BP2	K	BP2(1),K(2)
093	Y	N	D	-	D(1)
094	Y	N	D	-	D(1)
095	Y	N	D	-	D(1)
096	Y	N	N	BP1,BP2	BP1(097-1a,b,c), BP2(097-2a,b)
097	N	N	BP2	-	BP2(1a,b),BP2(2a,b)
098	N	N	BP2	K	BP2(1a,b),K(2,3,4,5)
099	Y	Y	BP2	D	BP2(1a,b),BP2(2a,b),D(3)
100	N	N	N	-	-
101	Y	N	K	-	K(1,2)
102	Y	N	BP2	-	BP2(1a,b)
103	Y	N	BP2	-	BP2(1a,b)
104	Y	Y	BP2	K	BP2(1a,b),BP2(2a,b),BP2(3),K(4)
105	Y	N	BP1	-	BP1(1)
106	Y	N	K	D	K(1,2,3),D(4,5)
107	Y	Y	D	-	D(1a,b,c),D(2a,b)
108	Y	N	K	D	K(1),D(2,3)
109	Y	N	K	-	K(1)
110	Y	N	K	D	K(1,3),D(2)
111	Y	N	BP2	-	BP2(1a,b)
112	N	Y	BP4	-	BP4(1a,b,c,d)
113	Y	N	BP5	-	BP5(1a,1b,2a,2b,3a)
114	Y	N	N	-	-
115	N	Y	N	-	-
116	Y	N	D	-	D(1a,b),D(2)
117	N	N	N	-	-
118	Y	Y	K	-	K(1,2,3)
119	N	N	BP2	-	BP2(1a,b)
120	N	Y	K	-	K(1,2)
121	Y	Y	K	-	K(1)
122	Y	N	BP2	-	BP2(1a,b)
123	Y	N	K	-	K(1,2,3,4)
124	Y	Y	D	-	D(1,2)
125	Y	N	BP2	-	BP2(1a,b)
126	Y	N	BP1	K,D	BP1(1),K(2,3),BP1(4),D(5a,b,c),D(6)

Table B2 – *continued* General classification of the sources.

ID	Ext. Continuum Emission	Stellar Cluster	Primary H_2 Classification	Secondary H_2 Classification	Components
127	Y	N	BP2	K,D	BP2(1a,b),K(2,3,4),BP2(128-1a,b),D(128-2)
128	Y	Y	BP2	D,K	BP2(1a,b),D(2),K(3)
129	Y	Y	BP2	-	BP2(1a,b)
130	Y	Y	BP2	K	BP2(1a,b), K(2)
131	Y	Y	D	-	D(1a,b,c), D(2a,b,c)
132	Y	N	BP2	-	BP2(1a,b,c)
133	Y	Y	D	K	D(1a,b,c,d),D(2,3),K(106-1,106-2,106-3),K(106-4a,b),D(106-5)
134	N	N	K	D,BP2	K(1a,b,c,d,e),K(2),K(3a,b,c),K(4a,b),D(5),BP2(136-1a,b),BP2(136-2),K(8)
135	Y	Y	D	-	D(1)
136	Y	N	BP4	-	BP4(1a,1b,2a,2b,2c)
137	Y	N	K	D	K(1,2,3),D(4,5,6)
138	Y	Y	K	-	K(1,2)
139	Y	Y	BP2	-	BP2(1a,b)
140	N	Y	BP1	K	BP1(1),K(2),BP1(141-1)
141	Y	Y	BP1	-	BP1(1),BP1(140-1)
142	Y	N	BP2	-	BP2(1a,b)
143	Y	Y	K	-	K(1a,b)
144	N	N	K	-	K(1)
145	Y	N	BP2	K	BP2(1a,b,c), BP2(2a,b), K(3,4,5)
146	Y	N	BP1	D	BP1(1a,b), D(2a,b,c)
147	Y	N	D	K	D(1,2),K(146-1)
148	Y	N	D	-	D(1)
149	Y	Y	BP1	K,D	BP1(1), K(2), D(3a,b,c,d), D(4)
150	Y	Y	BP2	K	BP2(1a,b), K(2)
151	N	N	K	-	K(1,2)
152	N	N	N	-	-
153	Y	Y	BP2	K,BP1	BP2(1a,b), K(2), BP1(3a,b)
154	Y	Y	K	D,BP2	K(1,2,3,5), D(4,7), BP2(6a,b)
155	Y	N	BP4	K	BP4(1a,1b,2a,2b), K(3,4,5)
156	Y	Y	N	-	-
157	N	N	N	-	-
158	N	N	K	-	K(1,2)
159	Y	Y	K	BP2	K(1,3), BP2(2a,b), BP2(4a,b)
160	Y	N	N	-	-
161	N	N	K	-	K(1)
162	Y	Y	BP8	K	BP8(1a,1b,1c,4,6a,6b,7a,7b), K(2,3,5)
163	Y	Y	BP6	K	BP6(2a,2b,5a,5b,7a,7b), K(1,3,4,6), K(9a,b)
164	Y	Y	K	BP2,D	K(1,2,3,4,5,7,10), BP2(6a,b,c), BP2(8a,b), BP2(9a,b), D(11a,b), D(12)
165	Y	N	K	BP2,D	K(1,2,3,4,5),BP2(6,7),D(not labelled)
166	N	N	N	D	D(1)
167	Y	Y	BP4	BP1,BP2	BP4(1a,1b,2a,2b),BP1(3),BP2(4a,b)
168	Y	N	BP2	K	BP2(1a-e),K(2,3)
169	Y	Y	D	-	D(1,2,3)
170	Y	N	K	D	K(1a,1b),D(2),D(171-1)
171	Y	Y	BP2	K,D	BP2(1a,b,c),K(2-12),D(13a,b,c)
172	N	N	N	-	-
173	N	Y	D	-	D(not labelled)
174	Y	Y	D	K	D(1),K(2)
175	Y	Y	K	-	K(1a,b),K(2a,b),K(3,4)
176	Y	Y	BP2	-	BP2(1a,1b,2a,2b)
177	Y	Y	D	-	D(1),D(2a,b)
178	N	Y	K	-	K(1,2)
179	Y	N	BP3	K,D	BP3(1a,1b,2),K(3,4),D(5a,b)
180	Y	Y	K	BP1,BP2	K(1,2,4,5,6,7),BP1(3),BP2(8a,b,c),BP2(9a,b,c),BP2(10a,b)
181	Y	N	BP1	-	BP1(1a,b)
182	Y	N	K	BP2,D	K(1,2,4),BP2(3a,b),D(5,6,7)
183	Y	N	BP4	K	BP2(1a,1b,2a,2b),K(3)
184	N	N	N	-	-
185	Y	N	N	-	-
186	Y	N	N	-	-
187	Y	Y	BP2	-	BP2(1a-e)
188	Y	N	K	-	K(1,2,3)

Table B2 – *continued* General classification of the sources.

ID	Ext. Continuum Emission	Stellar Cluster	Primary H ₂ Classification	Secondary H ₂ Classification	Components
189	N	N	BP2	-	BP2(1a,b)
190	Y	N	K	-	K(1,2,3)
191	N	N	N	-	-
192	Y	N	K	-	K(1,2)
193	Y	N	BP2	K	BP2(1a,b),K(2)
194	N	N	N	-	-
195	Y	N	N	-	-
196	Y	Y	BP1	K	BP1(1),K(2)
197	Y	Y	K	D	K(1),D(2)
198	Y	N	K	-	K(1,2)
199	Y	Y	K	-	K(1)
200	Y	Y	N	-	-
201	N	Y	D	-	D(1)
202	Y	Y	D	-	D(1)
203	Y	N	N	-	-
204	Y	N	BP2	-	BP2(1a,b)
205	N	Y	N	-	-
206	Y	N	BP2	-	BP2(1a,b)
207	Y	N	BP2	K	BP2(1a,b),K(2,3)
208	N	N	N	-	-
209	Y	N	BP4	K	BP2(1a-1g,2a,b,c),K(3,4,5,6,7)
210	N	N	N	-	-
211	Y	Y	K	-	K(1a)
212	Y	N	BP4	BP2,K	BP1(1a,1b,2a,2b),BP2(3a-3f),K(4)
213	Y	N	K	-	K(1,2)
214	Y	N	D	K	D(1a,b),K(1c-f),K(2,3,4)
215	Y	Y	K	D	K(1),D(2a,b)
216	N	N	K	-	K(1,2)
217	Y	Y	D	-	D(1),D(2a,b)
218	Y	N	N	-	-
219	Y	Y	N	-	-
220	Y	N	BP2	K	BP2(1a,b,c,d),K(2)
221	N	N	N	-	-
222	Y	N	D	-	D(1,2,3)
223	N	N	K	-	K(1)
224	N	Y	K	-	K(1,2,3)
225	N	N	N	-	-
226	N	Y	N	-	-
227	N	N	N	-	-
228	Y	N	BP2	K	BP2(1a,b),K(2,3,4)
229	Y	Y	D	-	D(1a,b)
230	N	Y	N	-	-
231	Y	N	BP2	-	BP2(1a,b)
232	N	N	N	-	-
233	Y	N	BP2	K	BP2(1a,b),K(2,3,4)
234	Y	N	BP1	-	BP1(1)
235	N	Y	N	-	-
236	Y	N	D	-	D(1)
237	Y	Y	BP4	K	BP4(1a,1b,1c,2a,2b),K(3,4)
238	Y	N	BP2	-	BP2(1a,1b)
239	N	N	D	-	D(1,2a,2b)
240	N	N	N	-	-
241	Y	N	D	-	D(1)
242	N	N	K	-	K(1)
243	N	N	N	-	-
244	N	N	N	-	-
245	Y	Y	D	-	D(1),D(2a,b)
246	Y	Y	N	-	-
247	N	N	D	-	D(1)
248	N	N	N	-	-
249	Y	N	D	-	D(1)
250	N	Y	D	-	D(1)
251	N	N	K	-	K(1,2)

Table B2 – *continued* General classification of the sources.

ID	Ext. Continuum Emission	Stellar Cluster	Primary H ₂ Classification	Secondary H ₂ Classification	Components
252	Y	Y	N	-	-
253	Y	Y	N	-	-
254	N	Y	N	-	-
255	N	N	BP2	-	BP2(1a,b)
256	Y	N	N	-	-
257	N	Y	N	-	-
258	N	N	N	-	-
259	N	Y	N	-	-
260	Y	N	N	-	-
261	N	N	N	-	-
262	N	N	N	-	-
263	Y	N	N	-	-
264	Y	N	N	-	-
265	N	N	N	-	-
266	Y	Y	N	-	-
267	Y	N	N	-	-
268	N	N	N	-	-
269	Y	N	K	-	K(1)
270	Y	N	D	-	D(1)
271	N	N	N	-	-
272	Y	N	K	-	K(1,2),D(3)
273	N	N	N	-	-
274	Y	Y	BP2	K	BP2(1a,b),K(2,3,4,5,6,7)
275	N	N	N	-	-
276	Y	N	N	-	-
277	N	N	N	-	-
278	N	N	N	-	-
279	N	N	N	-	-
280	Y	N	N	-	-
281	Y	N	N	-	-
282	N	N	N	-	-
283	N	N	N	-	-
284	N	N	N	-	-
285	Y	N	N	-	-
286	N	N	N	-	-
287	Y	N	BP2	-	BP2(1a,b)
288	N	N	K	-	K(1)
289	N	N	N	-	-
290	Y	N	N	-	-
291	N	N	N	-	-
292	Y	N	BP1	-	BP1(1a,b,c,d)
293	N	N	N	BP1	-
294	N	N	N	-	-
295	Y	N	BP4	-	BP4(1a,1b,2,3)
296	Y	N	BP2	-	BP2(1a,b,c)
297	N	N	N	-	-
298	N	N	N	-	-
299	N	N	N	-	-
300	N	N	N	-	-
301	Y	N	D	-	D(1a,b,c,d)
302	N	N	N	-	-
303	N	N	N	-	-
304	Y	N	N	-	-
305	Y	Y	D	K	D(1),K(2a,b,c,d)
306	N	N	N	-	-
307	Y	Y	BP2	-	BP2(1a,b)
308	Y	N	N	-	-
309	Y	N	K	-	K(1)
310	Y	N	D	-	D(1),K(2)
311	Y	N	N	-	-
312	N	N	N	-	-
313	N	N	K	-	K(1,2)
314	N	N	N	-	-

Table B2 – *continued* General classification of the sources.

ID	Ext. Continuum Emission	Stellar Cluster	Primary H ₂ Classification	Secondary H ₂ Classification	Components
315	Y	N	BP2	-	BP2(1a,b)
316	N	N	N	-	-
317	N	N	N	-	-
318	N	N	N	-	-
319	Y	Y	D	-	D(1,2)
320	Y	N	N	-	-
321	N	N	N	-	-
322	Y	N	N	-	-
323	Y	N	D	-	D(1)
324	Y	N	N	-	-
325	Y	N	K	D	K(1),D(2a,b,c,d)
326	Y	N	K	-	K(1,2)
327	N	N	N	-	-
328	N	N	N	-	-
329	N	Y	N	-	-
330	N	N	N	-	-
331	N	N	N	-	-
332	Y	N	N	-	-
333	N	N	N	-	-
334	N	N	N	-	-
335	N	N	N	-	-
336	Y	N	K	-	BP2(1a,b,c),K(2)
337	N	N	BP2	K,D	BP2(1a,b),K(2,3),D(4,5)
338	Y	N	K	-	K(1)
339	Y	N	K	-	K(1,2,3)
340	N	N	N	-	-
341	Y	N	BP2	K	BP2(1a,b,c),K(2)
342	N	N	N	-	-
343	N	N	D	-	D(not labelled)
344	Y	N	N	-	-
345	N	N	K	-	K(1)
346	N	N	N	-	-
347	Y	N	D	K	D(1)
348	Y	N	N	-	-
349	N	N	N	-	-
350	Y	N	N	-	-
351	Y	N	D	-	D(1)
352	N	N	N	-	-
353	N	N	N	-	-

Table B3. Properties of the structures identified on each field.

ID	Structure	ℓ_{proj} (pc)	PA ($^\circ$)	R	ID	Structure	ℓ_{proj} (pc)	PA ($^\circ$)	R
002	BP2(1a,b)	1.26, 0.91	50, 265	11.0, 8.0	108	D(2)	1.87	30-200	-
002	D(2a,b)	3.96	200-320	-	108	D(3)	0.67	300-320	-
003	D(1)	0.51	0-360	-	109	K(1)	0.16	115	-
006	BP2(1a-f)	0.68, 0.74	70, 285	5.5, 5.9	110	K(1)	0.08	135	-
006	K(2)	0.84	50	-	110	D(2)	0.10	45	-
006	K(3)	0.68	290	-	110	K(3)	0.31	90	-
006	K(4)	0.96	330	-	111	BP2(1a,b)	0.45, 0.84	45, 240	3.5, 7.4
019	BP2(1a,b)	0.28, 0.34	315, 135	1.6, 3.1	112	BP4(1a,b,c,d)	0.75, 1.00, 0.58, 0.94	355, 185, 290, 165	16, 15, 6.8, 11
026	BP2(1a-h)	2.27, 2.27	125, 295	3.8, 11.0	113	BP5(1a,b)	2.70, 2.38	355, 180	3.5, 3.3
034	K(1)	0.35	100	-	113	BP5(2a,b)	1.66, 1.24	210, 30	3.2, 3.0
034	K(2)	0.31	0	-	113	BP5(3a)	0.78	300	2.5
034	K(3)	0.72	270	-	116	D(1a,b)	1.17	290-360	-
034	K(4)	0.65	180	-	116	D(2)	0.40	180-210	-
034	K(5)	1.16	345	-	119	BP2(1a,b)	0.12, 0.10	45, 260	3.3, -
053	D(1)	1.27	10-60	-	120	K(1)	0.23	0	-
053	D(2)	0.73	320-335	-	120	K(2)	0.26	270	-
053	D(3)	1.91	225-290	-	121	K(1)	0.44	170	-
054	K(1)	0.15	20	-	122	BP2(1a,b)	0.44, 0.73	135, 315	0.9, 2.0
054	K(2)	0.44	340	-	124	D(1)	0.99	250-360	-
054	K(3)	0.51	270	-	124	D(2)	0.79	210-240	-
054	K(4)	0.99	65	-	125	BP2(1a,b)	0.19, 0.26	20, 195	2.0, 4.5
055	BP2(1a,b)	0.39, 0.29	60, 250	4.5, 5.0	126	BP1(1)	0.32	270	1.1
060	K(1)	0.04	60	-	126	K(2)	0.98	110	-
060	K(2)	0.16	330	-	126	K(3)	1.30	150	-
077	K(1)	0.31	325	-	126	BP1(4)	0.70	255	5.7
077	K(2)	1.30	270	-	126	D(5a,b,c)	4.10	275 < θ < 30	-
082	K(1)	1.05	235	-	126	D(6)	2.40	50, 240	-
082	K(2)	0.66	300	-	127	BP2(1a,b)	0.22, 0.35	60, 230	3.5, 7.0
085	K(1)	0.77	310	-	127	BP2(128-1a,b)	0.13, 0.13	40, 60	5.2, 7.8
086	D(1)	0.62	0-125	-	127	D(128-2)	0.88	50	-
086	D(2)	2.50	235-270	-	127	K(2)	1.80	345	-
086	D(3)	2.02	0-40	-	127	K(3)	2.10	335	-
086	D(4)	1.50	170-185	-	127	K(4)	2.81	320	-
086	D(067-1)	-	115-130	-	128	BP2(1a,b)	0.39, 0.39	150, 320	5.2, 7.8
086	D(067-2)	-	45-110	-	128	D(2)	0.72	55, 235	-
087	D(1)	2.64	110-165	-	128	K(3)	1.28	30	-
087	D(2)	2.64	35-110	-	129	BP2(1a,b)	1.64, 1.61	75, 275	4.8, 5.0
087	D(066-1)	-	275-290	-	130	BP2(1a,b)	0.43, 0.59	125, 275	1.6, 3.6
087	D(066-3)	-	315-10	-	130	K(2)	0.64	195	-
087	D(066-4)	-	200-230	-	131	D(1a,b,c)	1.46	-	-
088	D(1)	0.97	20-110	-	131	D(2a,b,c)	2.92	-	-
088	D(2)	1.99	110-240	-	132	BP2(1a,b,c)	0.20, 0.30	15, 205	3.1, 4.1
089	K(1)	0.18	25	-	133	D(1a,b,c,d)	6.69	-	-
089	D(2)	1.90	0-40	-	133	D(2)	3.30	240-300	-
090	BP2(1a,b,c,d)	0.78	80,35,345,335	7.5	133	D(3)	-	240	-
090	K(2)	0.96	15	-	133	K(106-1)	-	145	-
090	K(3)	1.08	10	-	133	K(106-2,106-3)	-	135	-
091	BP2(1a,b)	1.02, 0.91	100, 250	1.8, 1.4	133	K(106-4a,b)	-	180,170	-
092	K(1)	0.28	60	-	133	D(106-5)	-	105	-
092	BP2(2)	0.28	0, 195	3.4	134	K(1a,b,c,d,e)	-	150,110,80,5,180	-
093	D(1)	6.57	45-110	-	134	K(2)	-	310	-
094	D(1)	5.84	240-320	-	134	K(3a,b,c)	-	20,0,245	-
096	BP2(097-1a,b,c)	1.77	75-145	-	134	K(4a,b)	-	265,245	-
096	BP2(097-2a,b)	0.88	100	-	134	D(5)	-	5	-
097	BP2(1a,b)	0.85, 0.76	200, 15	4.8, 5.2	134	BP2(107-1a,b)	-	95, 55	-
097	BP2(2a,b)	0.88	30-70,335	7.5, 15.0	134	BP2(107-2)	-	75	-
098	BP2(1a,b)	0.11, 0.05	250, 30	2.3, 1.5	134	K(8)	-	240	-
098	K(2)	0.09	215	-	136	BP4(1a,b)	2.06, 2.35	155, 350	7.2, 5.6
098	K(3)	0.14	225	-	136	BP4(2a,b,c)	0.56, 0.56	270, 255, 100	4.8, 6.7
098	K(4)	0.23	225	-	137	K(1)	0.20	0	-
098	K(5)	0.10	115	-	137	K(2)	0.44	75	-
099	BP2(1a,b)	0.90, 0.67	40, 235	11.2, 8.4	137	K(3)	1.96	85	-
099	BP2(2a,b)	0.86, 0.80	50, 310	4.5, 8.3	137	D(4)	-	55	-
099	D(3)	1.12	195	-	137	D(5)	-	340	-
102	BP2(1a,b)	0.77, 0.60	20, 175	1.8, 7.0	137	D(6)	-	130	-
103	BP2(1a,b)	1.31, 1.31	55, 235	4.0, 9.3	138	K(1)	0.85	305	-
104	BP2(1a,b)	1.25, 1.25	60, 250	4.6, 5.7	138	K(2)	0.62	285	-
104	BP2(2a,b)	0.60, 0.62	60, 250	2.2, 2.5	139	BP2(1a,b)	0.33, 0.26	160, 15	4.8, 7.5
104	BP2(3)	0.46	350	5.6	140	BP1(1)	1.40	35	6.5
104	K(4)	[1.14]	340	-	140	K(2)	0.94	270	-
105	BP1(1)	0.09	105	6	140	BP1(141-1)	-	30	4.6
106	K(1)	-	220	-	141	BP1(1)	0.89	65	4.6
106	K(2)	-	220	-	141	BP1(140-1)	-	185	6.5
106	K(3)	-	220	-	142	BP2(1a,b)	0.48, 0.38	10, 200	8.0, 6.3
106	D(4)	0.93	280-320	-	143	K(1a,b)	0.28, 0.21	75,210	-
106	D(5)	1.25	50-75	-	144	K(1)	0.07	330	-
107	D(1a,b,c)	0.98	280-355	-	145	BP2(1a,b,c)	0.70, 0.52, 0.52	350, 160, 185	6.5, 4.9, 5.6
107	D(2a,b)	1.05	335-75	-	145	BP2(2a,b)	0.52, 0.15	245, 230	6.0, -
108	K(1)	0.67	240	-	145	K(3)	0.57	280	-

Table B3 – *continued* Properties of the structures identified on each field.

ID	Structure	ℓ_{proj} (pc)	PA ($^{\circ}$)	R	ID	Structure	ℓ_{proj} (pc)	PA ($^{\circ}$)	R
145	K(4)	1.35	235	-	171	K(2-12)	-	-	-
145	K(5)	1.13	305	-	171	D(13a,b,c)	3.15	-	-
146	BP1(1a,b)	2.51, 2.01	350, 340	6.3, 8.0	175	K(1a)	0.38	280	-
146	D(2a,b,c)	5.24	100-225	-	175	K(1b)	0.13	95	-
149	BP1(1)	0.38	310	2	175	K(2a)	0.38	125	-
149	K(2)	0.92	320	-	175	K(2b)	0.27	260	-
149	D(3a,b,c,d)	4.88	-	-	175	K(3)	0.46	200	-
149	D(4)	1.90	275	-	175	K(4)	0.86	220	-
150	BP2(1a,b)	0.34, 0.20	15, 240	1.7, 1.1	176	BP2(1a,b)	0.24	0	16.6
150	K(2)	0.17	135	-	176	BP2(2a,b)	0.38	90, 270	8
151	K(1)	0.89	285	-	177	D(1)	1.20	125	-
151	K(2)	1.13	110	-	177	D(2a,b)	2.00	245-310	-
153	BP2(1a,b)	0.24, 0.24	270, 90	1.7, 1.3	178	K(1)	0.12	45	-
153	K(2)	0.28	180	-	178	K(2)	0.97	320	-
153	BP1(3a,b)	0.28, 0.28	125, 140	7.0, 7.0	179	BP3(1a,b)	0.24, 0.30	105, 285	5.3, 7.4
154	K(1)	0.55	140	-	179	BP3(2)	0.22	10	6.3
154	K(2)	0.47	310	-	179	K(3)	0.56	50	-
154	K(3)	0.66	220	-	179	K(4)	0.04	185	-
154	D(4)	0.50	220	-	179	D(5a,b)	1.00	100-260	-
154	K(5)	1.22	175	-	180	K(1)	0.24	310	-
154	BP2(6a,b)	0.33	40	-	180	K(2)	0.32	25	-
154	D(7)	1.70	15-75	-	180	BP1(3)	0.12	70	-
155	BP4(1a,b)	0.35, 0.35	230, 30	2.9, 2.8	180	K(4)	0.50	155	-
155	BP4(2a,b)	0.46, 0.43	235, 60	4.0, 6.8	180	K(5)	0.50	125	-
155	K(3)	0.38	300	-	180	K(6)	0.59	75	-
155	K(4)	0.49	15	-	180	K(7)	0.74	125	-
155	K(5)	0.31	155	-	180	BP2(8a,b,c)	0.22, 0.30	110,105,85	7.5, 8.0
158	K(1)	0.35	210	-	180	BP2(9a,b,c)	0.26, 0.31	185-175	9.0, 10.5
158	K(2)	0.88	170	-	180	BP2(10a,b)	0.12	150, 160	-
159	K(1)	0.70	215	-	181	BP1(1a,b)	0.59	305-20	0.8
159	BP2(2a,b)	0.43	160, 175	-	182	K(1)	0.22	260	-
159	K(3)	1.08	190	-	182	K(2)	0.30	320	-
159	BP2(4a,b)	0.27	175	-	182	BP2(3a,b)	0.28	165, 180	-
161	K(1)	6.99	125	6.8	182	K(4)	1.50	65	-
162	BP8(1a,b,c)	5.36, 6.38	330, 150	13.7, 26.0	182	D(5)	0.97	15	-
162	BP8(4)	-	50	-	182	D(6)	1.88	40	-
162	BP8(6a,b)	-	20,130	-	182	D(7)	1.66	325	-
162	BP8(7a,b)	-	60,45	-	183	BP4(1a,b)	0.43, 0.36	60, 240	2.2, 2.2
162	K(2)	5.99	355	-	183	BP4(2a,b)	1.75, 1.52	65, 270	7.6, 7.7
162	K(3)	11.60	355	-	183	K(3)	0.89	15	-
162	K(5)	-	15	-	187	BP2(1a-e)	1.16, 0.98	90, 240	16.7, 14.0
163	K(1)	0.72	180	-	188	K(1)	0.32	150	-
163	BP6(2a,b)	7.16	210, 330	4.8	188	K(2)	0.83	310	-
163	BP6(5a,b)	6.28	0, 265	5	188	K(3)	1.86	50	-
163	BP6(7a,b)	8.16	90, 135	5.41	189	BP2(1a,b)	0.38, 0.18	90, 270	4.0, 2.0
163	K(3)	3.89	285	-	190	K(1)	0.18	320	-
163	K(4)	0.88	345	-	190	K(2)	0.21	30	-
163	K(6)	3.39	30	-	190	K(3)	0.24	45	-
163	K(9a)	7.66	270	-	192	K(1)	0.25	105	-
163	K(9b)	10.17	270	-	192	K(2)	0.20	245	-
164	K(1)	3.30	275	-	193	BP2(1a,b)	0.16, 0.09	230, 50	2.8, 2.5
164	K(2)	7.25	285	-	193	K(2)	0.38	260	-
164	K(3)	11.87	285	-	196	BP1(1)	0.36	85	6
164	K(4)	-	270	-	196	K(2)	0.30	50	-
164	BP2(6a,b,c)	25.00	220, 210, 205	11.4	197	K(1)	0.32	305	-
164	K(7)	-	30	-	197	D(2)	0.46	340-355	-
164	BP2(8a,b)	-	55, 45	-	198	K(1)	0.47	180	-
164	BP2(9a,b)	-	50, 40	-	198	K(2)	0.95	130	-
164	D(11a,b)	36.27	290-315	-	199	K(1)	0.48	110	-
164	D(12)	32.97	30-330	-	201	D(1)	0.10	310	-
165	K(1)	1.98	330	-	202	D(1)	1.50	200	-
165	K(2)	-	240	-	204	BP2(1a,b)	0.6, 0.57	170, 340	15.0, 8.0
165	K(3)	-	265	-	206	BP2(1a,b)	0.64, 0.42	160, 330	3.9, 7.0
165	K(4)	-	265	-	207	BP2(1a,b)	0.16, 0.23	90, 240	3.0, 6.3
165	K(5)	-	255	-	207	K(2)	0.07	200	-
165	BP2(6)	-	240	-	207	K(3)	0.23	245	-
165	BP2(7)	-	225	-	209	BP4(1a-g)	0.50, 0.34	135, 330	15.0, 6.7
165	D(not labelled)	-	-	-	209	BP4(2a,b,c)	0.52, 0.72	75, 255	11.0, 8.0
167	BP4(1a,b)	0.10, 0.10	105, 285	3.0, 4.5	209	K(3)	0.26	90	-
167	BP4(2a,b)	0.12, 0.12	120, 135	3.8, 3.8	209	K(4)	0.56	100	-
167	BP1(3)	0.48	165	8.2	209	K(5)	0.30	320	-
167	BP2(4a,b)	0.13, 0.13	85	12.5, 12.5	209	K(6)	0.43	255	-
168	BP2(1a-e)	0.18, 0.11	320, 140	9.0, 5.0	209	K(7)	0.52	240	-
168	K(2)	0.08	300	-	211	BP1(1a)	0.11	150	1.2
168	K(3)	0.07	65	-	212	BP4(1a,1b)	0.04, 0.05	65, 245	-
169	D(1)	0.37	270	-	212	BP4(2a,b)	0.30	315, 130	-
169	D(2)	1.31	10-95	-	212	BP2(3a-f)	0.38, 0.58	170, 230, 260, 265, 320, 330	7.5, 11.8
169	D(3)	1.30	155	-	213	K(1,2)	0.16	340, 320	-
171	BP2(1a,b,c)	0.49, 0.23	245,70	11.3, 8.0	214	D(1a,b)	0.96	-	-

Table B3 – *continued* Properties of the structures identified on each field.

ID	Structure	ℓ_{proj} (pc)	PA ($^\circ$)	R	ID	Structure	ℓ_{proj} (pc)	PA ($^\circ$)	R
214	K(1c-f)	0.53	90	-	269	K(1)	0.51	155	-
214	K(2)	0.48	70	-	274	BP2(1a,b)	0.20, 0.03	150, 330	4.0, 7.5
214	K(3)	0.18	10	-	274	K(2)	0.08	205	-
214	K(4)	0.30	315	-	274	K(3)	0.18	175	-
215	K(1)	0.20	80	-	274	K(4)	0.18	205	-
215	D(2a,b)	0.68	260, 290	-	274	K(5)	0.21	235	-
216	K(1)	0.14	90	-	274	K(6)	0.14	265	-
216	K(2)	0.18	270	-	274	K(7)	0.12	280	-
217	D(1)	0.18	130	-	287	BP2(1a,b)	0.26, 0.06	305, 125	5.7, 2.0
217	D(2a,b)	1.09	220-30	-	288	BP1(1)	0.46	115	4
220	BP2(1a,b,c,d)	0.18, 0.18	90, 80, 270, 260	-	292	BP1(1a,b,c,d)	0.10	115	15
220	K(2)	0.12	25	-	295	BP4(1a,1b,2,3)	0.23, 0.31	90, 270, 290, 245	7.3, 7.5
223	K(1)	0.21	170	-	296	BP2(1a,b,c)	0.20, 0.18	125, 300	12.7, 4.4
224	K(1)	-	120	-	301	D(1a,b,c,d)	2.74	-	-
224	K(2)	0.31	145	-	305	D(1)	2.10	-	-
224	K(3)	0.35	340	-	305	K(2a,b,c,d)	2.50	135, 160, 185, 235	-
228	BP2(1a,b)	0.2, 0.43	0, 180	1.0, 3.0	307	BP2(1a,b)	0.09, 0.14	35, 215	3.0, 4.8
228	K(2)	0.74	85	-	309	K(1)	0.26	270	-
228	K(3)	1.09	85	-	310	D(1)	2.77	300-70	-
228	K(4)	0.71	250	-	310	K(2)	0.45	185	-
229	D(1a,b)	0.52	15-140	-	313	K(1)	0.09	190	-
231	BP2(1a,b)	0.43, 0.32	50, 230	5.7, 6.0	313	K(2)	0.25	190	-
233	BP2(1a,b)	0.22, 0.13	20, 200	7.0, 5.3	315	BP2(1a,b)	0.35, 0.26	10, 185	4.2, -
233	K(2)	0.42	5	-	319	D(1)	0.31	130	-
233	K(3)	0.63	75	-	319	D(2)	0.25	260	-
233	K(4)	0.69	110	-	323	D(1)	0.86	125	-
234	BP1(1)	0.08	350	5.5	325	K(1)	0.15	5	-
236	D(1)	0.60	265-350	-	325	D(2a,b,c,d)	0.28	-	-
237	BP4(1a,b,c)	0.21, 0.21	115, 295	6.3, 6.3	326	K(1)	0.04	330	-
237	BP4(2a,b)	0.13, 0.13	85, 265	3.8, 3.8	326	K(2)	0.10	350	-
237	K(3)	0.23	295	-	336	BP2(1a,b,c)	0.56, 0.49	345, 270, 150	6.0, 5.8
237	K(4)	0.29	200	-	336	K(2)	0.32	60	-
238	BP2(1a,1b)	0.47, 0.59	65, 245	5.3, 10.0	337	BP2(1a,b)	0.49, 0.61	45, 225	5.3, 6.7
239	D(1,2a,2b)	1.07	-	-	337	K(2)	0.34	205	-
242	K(1)	0.45	200	-	337	K(3)	0.62	345	-
245	D(1)	0.26	140	-	337	D(4)	1.83	315	-
245	D(2a,b)	0.70	180, 290	-	337	D(5)	2.14	255	-
247	D(1)	0.87	120	-	338	K(1)	0.21	150	-
249	D(1)	0.72	235-330	-	341	BP2(1a,b,c)	0.30, 0.28	90, 75, 275	7.8, 9.3
250	D(1)	0.50	-	-	341	K(2)	0.19	135	-
251	K(1)	0.45	175	-	345	K(1)	1.43	290	-
251	K(2)	0.82	175	-	347	D(1)	1.22	350	-
255	BP2(1a,b)	0.11, 0.67	80, 260	1.0, 4.8	352	D(1)	0.67	70	-

Table B4. Properties of the stellar clusters identified on each field.

ID	RA (J2000)	Dec (J2000)	d (kpc)	ℓ_{proj} (pc)	$\Delta\theta$ (")
22	18 36 47	-07 35 39	9.6	0.85	20
34	18 43 46	-03 35 29	8.7	1.35	45
39	18 47 36	-02 01 50	9.1	0.95	25
66	19 07 01	08 18 44	11.2	0.47	20
81	19 44 24	25 48 43	15.9	0.96	15
85	20 21 55	39 59 45	4.5	0.70	35
87	20 29 37	39 01 15	4.5	0.95	40
88	20 19 40	40 56 33	3.8	1.08	60
91	20 29 25	40 11 19	4.7	0.6	30
99	20 38 56	42 22 41	3.7	0.62	40
104	20 38 37	42 37 20	1.2	0.58	100
107	20 42 34	42 56 51	1.0	0.26	55
112	21 31 45	51 15 35	5.6	1.25	45
115	21 15 55	54 43 30	10.7	0.73	20
118	21 43 02	54 56 20	7.9	1.25	30
120	21 52 57	56 39 54	7.4	0.52	15
121	22 16 10	52 21 34	4.8	0.58	25
124	22 55 29	57 09 24	6.1	0.8	30
126	22 58 45	58 47 00	5.5	2.40	60
127	22 59 03	59 28 25	5.3	0.88	55
128	22 59 06	59 28 23	5.1	1.05	45
129	22 56 19	62 01 56	1.5	0.4	60
130	23 05 25	60 08 15	5.7	0.92	35
131	23 05 10	60 14 42	5.6	1.46	70
133	23 13 33	61 29 06	6.2	2.57	85
135	23 13 45	61 28 23	6.1	1.4	50
138	23 15 31	61 07 09	6.0	1.16	45
139	23 28 28	64 17 37	5.5	0.88	35
140	00 23 57	66 05 51	7.3	1.25	35
141	00 24 01	66 06 45	7.3	0.79	25
143	01 16 37	64 50 43	5.5	0.49	20
149	02 29 02	61 33 31	5.6	0.9	35
150	02 43 28	62 57 10	9.3	1.45	35
153	03 01 32	60 29 12	4.0	2.69	140
154	03 07 24	58 30 43	4.3	1.11	55
156	03 27 31	58 19 21	5.7	0.73	25
159	03 56 15	53 52 13	4.3	0.86	45
162	05 39 10	35 45 17	22.3	4.09	35
163	05 39 28	35 40 43	20.9	4.03	40
164	05 41 07	35 49 35	34.0	6.25	35
167	06 08 53	21 38 28	1.0	0.44	95
169	06 09 21	20 39 15	2.7	1.86	145
171	06 12 54	17 59 22	1.8	0.61	70
173	06 11 22	17 26 33	8.0	1.21	30
174	06 13 21	15 23 48	3.9	0.95	50
175	06 13 16	15 22 25	3.7	0.95	50
176	06 15 35	14 17 05	2.1	0.3	30
177	06 14 37	13 49 36	3.9	2.32	120
178	06 21 47	10 39 21	7.9	1.63	40
180	06 41 10	09 29 33	1.0	1.78	370
187	06 47 50	-02 12 54	3.0	1.46	100
196	07 19 00	-18 02 41.5	4.1	0.57	30
197	07 32 10	-16 58 13	1.6	0.92	240

Table B4 – continued Properties of the stellar clusters identified on each field.

ID	RA (J2000)	Dec (J2000)	d (kpc)	ℓ_{proj} (pc)	$\Delta\theta$ (")
199	07 48 43	-26 39 31	6.7	1.42	45
200	08 02 43	-34 31 49	5.9	0.95	35
201	08 15 57	-36 08 08	4.1	0.65	35
202	08 26 17	-40 48 40	7.0	1.17	35
205	08 29 14	-41 10 48	7.0	0.85	25
211	08 48 49	-43 32 29	2.6	1.10	90
215	08 59 28	-43 45 18	2.0	1.38	150
217	08 58 04	-47 23 10	2.1	1.1	115
219	09 00 41	-47 26 02	2.1	0.74	75
224	09 04 29	-48 49 25	2.3	0.3	30
226	09 11 08	-48 15 56	10.2	0.97	20
229	09 59 16	-56 54 45	1.6	0.48	60
230	10 01 34	-56 47 18	0.2	0.03	25
235	10 26 36	-58 00 30	6.2	0.41	15
237	10 42 49	-59 25 29	2.5	0.82	70
245	11 30 07	-62 03 13	3.3	0.47	50
246	11 34 33	-63 58 03	0.8	0.17	45
250	11 53 08	-63 08 56	10.4	0.4	10
252	11 56 50	-63 32 05	9.9	1.50	25
253	12 15 25	-63 01 17	11.1	1.68	30
254	12 28 36	-62 58 33	4.2	0.84	40
257	12 41 54	-62 04 15	4.4	0.63	30
259	12 47 09	-63 36 29	12.6	0.92	15
266	13 14 26	-62 44 30	5.9	0.50	20
274	13 32 47	-60 26 56	1.7	0.73	90
305	15 31 44	-56 30 27	10.4	3.45	65
307	15 43 19	-54 07 35	2.8	0.42	30
319	16 06 26	-50 43 22	4.8	0.93	40
329	16 25 40	-48 55 16	10.4	0.45	10

This paper has been typeset from a \TeX / \LaTeX file prepared by the author.